HELLENIC REPUBLIC
National and Kapodistrian University of Athens
EST. 1837

SCHOOL OF SCIENCE
DEPARTMENT OF PHYSICS
SECTION OF ASTROPHYSICS, ASTRONOMY AND MECHANICS

Master Thesis

Multiwavelength study of QPOs in Active Galactic Nuclei

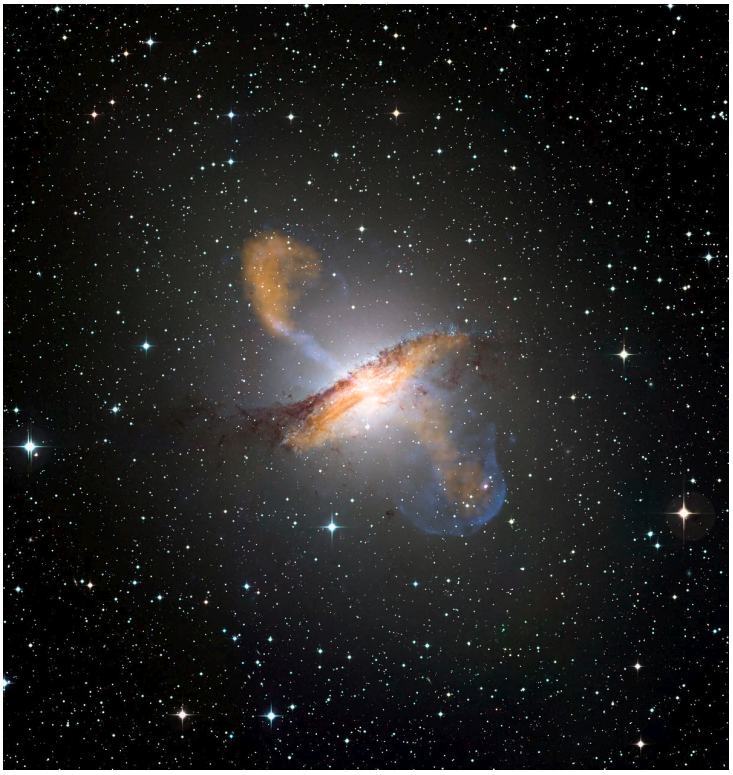

Konstantina Vrontaki
AM 2020306

Supervisor:

Dr. Kosmas Gazeas
Lecturer of Observational Astrophysics

Athens 2022

HELLENIC REPUBLIC
National and Kapodistrian University of Athens
EST. 1837

SCHOOL OF SCIENCE
DEPARTMENT OF PHYSICS
SECTION OF ASTROPHYSICS, ASTRONOMY AND MECHANICS

Master Thesis Report

Multiwavelength study of QPOs in Active Galactic Nuclei

Konstantina Vrontaki
AM 2020306

Supervising committee:

Kosmas Gazeas, Lecturer, NKUA
Maria Petropoulou, Assistant Professor, NKUA
Stanislaw Zola, Professor, Jagiellonian University

Athens 2022

Abstract

Active galaxies have greater luminosity than anticipated based on their stellar population. Their luminosity is due to non-thermal phenomena that occur in a compact region in the center of the galaxy, known as *Active Galactic Nucleus* (AGN). A supermassive black hole (SMBH) exists in the center of the AGN, surrounded by hot magnetized plasma that creates an accretion disk. AGNs are classified in different subclasses based on their characteristics. The most energetic subclass of AGNs is *blazars*. Their jets are aligned with the line of sight and they display variability of different timescales across the electromagnetic spectrum. Although their signal seems non-periodic, quasi-periodic oscillations have been reported in the recent years.

In this study, that was carried out in the frame of *BOSS Project*, Quasi-Periodic Oscillations (QPO) of intra-day (IDV), short-term (STV) and long-term (LTV) timescales were sought in the light curves of blazars. Time-domain analysis of multi-wavelength light curves of AGNs was conducted by combining radio and optical wavelengths, and X-rays, in order to compare the results and find the correlation between the different wavelengths. A total of 21 targets were studied in 5 energy bands between 2013 and 2021. The data in optical wavelengths are from the University of Athens Observatory (UOAO), with observations conducted in the frame of *BOSS Project*. In radio wavelengths data were provided by Metsähovi Radio Observatory (37 GHz), Owens Valley Radio Observatory (OVRO) (15 GHz), and Xinjiang Astronomical Observatory by the Nanshan Radio Telescope (NSRT) (4.8 GHz). Data in X-rays were obtained from the Swift Space Telescope (Swift-XRT). The data were analyzed using the Discrete Fourier Transform (DFT) and the Lomb-Scargle Periodogram (LSP) in order to find the timescales of QPOs.

The detected timescales of QPOs can provide information about the inner regions of the AGN, which are difficult to observe directly with our current instruments. For example, the mass of the SMBH of AGNs is usually calculated using spectroscopic methods, but due to the featureless continuum of blazars, such methods have several constraints. On the other hand, the detected QPOs are an important tool in the estimation of the mass of the SMBH of blazars and AGNs in general, setting a limit to the value. The detected timescales also place constraints on other parameters of AGNs such as the Eddington luminosity and the accretion rate.

The comparison of the detected timescales of QPOs in different wavelengths provides insights about the region of origin of the quasi-periodic signals of the AGNs, giving information on whether the signals originate from the same region or not. This study indicates that the QPOs arise from the same region regardless the energy band that were detected. This confirms the model that suggests that quasi-periodic signals arise from instabilities in the inner region of the AGN that propagate along the jet.

Multi-wavelength time series analysis and the detection of QPOs can shed light in the mysterious nature of AGNs, the processes that occur in their inner region, where direct observations are difficult to be made, and the mechanisms that lead to quasi-periodic signals.

Keywords: BOSS Project, Active Galactic Nuclei, Blazars, Quasi-periodic Oscillations, photometry, time-series analysis, Discrete Fourier Transform, Lomb-Scargle Periodogram, Multi-wavelength Astronomy

Περίληψη

Οι Ενεργοί Γαλαξίες έχουν μεγαλύτερη φωτεινότητα από αυτή που αναμένεται με βάση τον αστρικό τους πληθυσμό. Η φωτεινότητα αυτή προέρχεται από μη θερμικά φαινόμενα που συμβαίνουν σε μία συμπαγή περιοχή στο κέντρο του γαλαξία, γνωστή ως *Ενεργός Γαλαξιακός Πυρήνας* (ΕΓΠ). Στο κέντρο ενός ΕΓΠ υπάρχει μία υπερμεγέθης μελανή οπή, γύρω από την οποία υπάρχει θερμό μαγνητισμένο πλάσμα που δημιουργεί έναν δίσκο προσαύξησης. Οι ΕΓΠ ταξινομούνται σε υποκατηγορίες με βάση τα χαρακτηριστικά τους. Η πιο ενεργητική κατηγορία των ΕΓΠ είναι οι blazars. Οι πίδακες των blazars βρίσκονται στην ίδια κατεύθυνση με την ευθεία παρατήρησης, ενώ οι blazars εμφανίζουν έντονη μεταβλητότητα στην φωτεινότητα διαφόρων χρονικών κλιμάκων σε όλο το ηλεκτρομαγνητικό φάσμα. Αν και το σήμα τους φαίνεται μη περιοδικό, ημι-περιοδικές ταλαντώσεις (QPOs) έχουν βρεθεί τα τελευταία χρόνια.

Σε αυτή την μελέτη, η οποία πραγματοποιήθηκε στα πλαίσια του *BOSS Project*, ημι-περιοδικές μεταβολές ημερήσιας (IDV), βραχείας (STV) και μακράς (LTV) κλίμακας αναζητήθηκαν στις καμπύλες των blazars. Χρονική ανάλυση των πολυκυματικών καμπύλων των AGNs πραγματοποιήθηκε συνδυάζοντας παρατηρήσεις από ραδιοφωνικά και οπτικά μήκη κύματος, και ακτίνες Χ, με στόχο την σύγκριση των αποτελεσμάτων και την εύρεση συσχέτισης μεταξύ των διαφορετικών μηκών κύματος. Συνολικά 21 στόχοι μελετήθηκαν σε 5 ενεργειακές μπάντες μεταξύ 2013 και 2021. Τα δεδομένα στα οπτικά μήκη κύματος είναι από το Γεροσταθοπούλειο Πανεπιστημιακό Αστεροσκοπείο Αθηνών (UOAO), από παρατηρήσεις που πραγματοποιήθηκαν στα πλαίσια του *BOSS Project*. Στα ραδιοφωνικά μήκη κύματος, δεδομένα παρασχέθηκαν από το Metsähovi Radio Observatory (37 GHz), το Owens Valley Radio Observatory (OVRO) (15 GHz), και το Xinjiang Astronomical Observatory από το Nanshan Radio Telescope (NSRT) (4.8 GHz). Τα δεδομένα στις ακτίνες Χ είναι από το διαστημικό τηλεσκόπιο Swift (Swift-XRT). Η ανάλυση των δεδομένων πραγματοποιήθηκε με την χρήση της Discrete Fourier Transform (DFT) και του περιοδογράμματος Lomb-Scargle (LSP), ώστε να βρεθούν οι χρονικές κλίμακες των QPOs.

Οι χρονικές κλίμακες που βρέθηκαν μπορούν να μας δώσουν πληροφορίες για τις εσωτερικές περιοχές των ΕΓΠ, που είναι δύσκολο να παρατηρηθούν άμεσα με τα όργανα που έχουμε. Για παράδειγμα, η μάζα της υπερμεγέθους μελανής οπής των ΕΓΠ συνήθως υπολογίζεται με την χρήση φασματοσκοπικών μεθόδων, αλλά λόγω του φάσματος των blazar που δεν εμφανίζει έντονα χαρακτηριστικά, οι μέθοδοι αυτοί εμφανίζουν δυσκολίες. Αντίθετα, τα QPOs αποτελούν ένα χρήσιμο εργαλείο στον υπολογισμό της μάζας της υπερμεγέθους μελανής οπής των blazars και γενικότερα των ΕΓΠ, καθώς θέτουν ένα όριο στην τιμή της. Επιπλέον οι χρονικές κλίμακες που έχουν εντοπιστεί θέτουν περιορισμούς σε άλλες παραμέτρους των ΕΓΠ, όπως η φωτεινότητα Eddington και ο ρυθμός προσαύξησης.

Η σύγκριση μεταξύ των περιόδων που έχουν εντοπιστεί για διαφορετικά μήκη κύματος μπορούν να παρέχουν πληροφορίες για την προέλευση των ημι-περιοδικών σημάτων στους ΕΓΠ, όπως το αν προέρχονται από την ίδια περιοχή ή όχι. Η παρούσα μελέτη υποδεικνύει πως τα QPOs προέρχονται από την ίδια περιοχή ανεξαρτήτως από το μήκος κύματος στο οποίο εντοπίσθηκαν. Αυτό επιβεβαιώνει το μοντέλο που προτείνει πως τα ημι-περιοδικά σήματα προέρχονται από διαταραχές που συμβαίνουν στην εσωτερική περιοχή των ΕΓΠ και διαδίδονται στον πίδακα.

Η πολυκυματική ανάλυση χρονοσειρών και ο εντοπισμός των QPOs μπορούν να παρέχουν πληροφορίες για την μυστηριώδη φύση των ΕΓΠ, για τις διαδικασίες που συμβαίνουν στο εσωτερικό τους, όπου οι απευθείας παρατηρήσεις είναι δύσκολες, και τους μηχανισμούς που οδηγούν σε ημι-περιοδικά σήματα.

Λέξεις κλειδιά: BOSS Project, Ενεργοί Γαλαξιακοί Πυρήνες, Blazars, Ημι-περιοδικές μεταβολές, φωτομετρία, ανάλυση χρονοσειρών, Discrete Fourier Transform, περιοδόγραμμα Lomb-Scargle, Πολυκυματική Αστρονομία

Acknowledgements

Somewhere, something incredible is waiting to be known
-Carl Sagan

This study would not be possible if not for the help and the support of several people. First of all, I would like to thank my supervisor, Dr. Kosmas Gazeas, for inspiring my interest in Observational Astrophysics and for his guidance and support in every step of this thesis and my academic career. His passion in Astrophysical research and teaching was inspiring and provided great motive for continuous improvement. I would also like to thank my co-supervisors, Dr. Staszek Zola, for providing data and for his helpful comments about the time-series analysis for the detection of QPOs, and Dr. Maria Petropoulou, for her helpful comments about the interpretation of the results.

A huge thanks should also go to my parents, Sophia and Giorgos, for their unconditional daily tangible and emotional support, and for always believing in me. Lastly, I would like to thank my friends for their understanding and for always being there when I needed them.

This work is dedicated to all the people that believe in me and support me in every possible way.

List of abbreviations

AD	Accretion Disk
AGN	Active Galactic Nucleus
BL Lacs	BL Lac Objects
BLR	Broad Line Region
BOSS	Blazar Optical Sky Survey
CCD	Charged-Coupled Device
CGRaBS	Candidate Gamma-Ray Blazar Sample
cpd	cycles per day
DFT	Discrete Fourier Transform
FFT	Fast Fourier Transform
FR	Fanaroff-Riley type galaxies
FSRQ	Flat Spectrum Radio Quasars
HBL	High-frequency BL Lac objects
HMXB	High Mass X-ray Binary
IC	Inverse Compton
IDV	Intra-day variability
IGM	Intergalactic medium
LAC	LAT AGN Catalog
LBL	Low-frequency BL Lac objects
LSP	Lomb-Scargle Periodogram
LTV	Long-term variability
MRO	Metsähovi Radio Observatory
NLR	Narrow Line Region
NLRQ	Narrow Line Radio Galaxies
NSRT	Nanshan Radio Telescope
OVRO	Owens Valley Radio Observatory
OVV	Optically Violently Variable
QPO	Quasi-Periodic Oscillation
QSR	Quasi-Stellar Radio Sources or Quasars
QSO	Quasi-Stellar Objects
RBL	Radio-selected BL Lac Objects
SED	Spectral Energy Distribution
SMBH	Supermassive Black Hole
SSRQ	Steep Spectrum Radio Quasars
STV	Short-term variability
Sy	Seyfert type galaxies
UOAO	University of Athens Observatory
UV	Ultraviolet
VLBI	Very Long Baseline Interferometry
WEBT	Whole Earth Blazar Telescope
XAO	Xinjiang Astronomical Observatory
XBL	X-ray-selected BL Lac
XRT	X-Ray Telescope

Contents

1 Active Galactic Nuclei **1**

1.1 Morphology of AGNs 1

1.2 Unified model of AGNs 2

1.2.1 Seyfert galaxies 4

1.2.2 Narrow Line Radio Galaxies 5

1.2.3 Quasars 5

1.2.4 Blazars 6

1.3 Variability of AGNs 7

1.4 Quasi-periodic oscillations models 8

1.5 Correlation of flux variations from different wavelengths 9

2 Blazar Optical Sky Survey - BOSS Project **11**

2.1 *BOSS Project* targets 12

3 Data analysis **17**

3.1 Fourier Analysis 17

3.2 Lomb-Scargle Periodogram 18

4 Search for QPOs in optical wavelengths **21**

4.1 Observations and data reduction 21

4.1.1 University of Athens Observatory (UOAO) 21

4.1.2 Data reduction 22

4.2 Search for QPOs of intra-day timescales . . . 27
4.3 Search for QPOs of short-term timescales . . . 36
4.4 Search for Long-Term Variability (LTV) . . . 40

5 Search for QPOs in radio wavelengths 41

5.1 Metsähovi Radio Observatory . . . 41
5.2 Owens Valley Radio Observatory . . . 42
5.3 Xinjiang Astronomical Observatory . . . 42
5.4 Data acquisition . . . 43
5.4.1 Observations at 37 GHz . . . 43
5.4.2 Observations at 15 GHz . . . 44
5.4.3 Observations at 4.8 GHz . . . 45
5.5 Data Analysis . . . 45
5.6 Search QPOs of short-term timescales . . . 46
5.6.1 Short-term QPOs at 37 GHz . . . 46
5.6.2 Short-term QPOs at 15 GHz . . . 48
5.6.3 Short-term QPOs at 4.8 GHz . . . 50
5.7 Search for Long-Term Variability (LTV) . . . 51
5.7.1 Long-term variability at 37 GHz . . . 51
5.7.2 Long-term variability at 15 GHz . . . 52
5.7.3 Long-term variability at 4.8 GHz . . . 52

6 Search for QPOs in X-rays 55

6.1 Neil Gehrels Swift Observatory . . . 55
6.2 Data acquisition . . . 56
6.3 Data analysis . . . 59
6.4 Search for QPOs of intra-day timescales . . . 59
6.5 Search for QPOs of short-term timescales . . . 74

6.6 Search for Long-Term Variability (LTV) 78

7 Discussion and Conclusions **81**

7.1 Study of the optical emitting region 81

7.2 Comparative study of the detected QPOs for different optical activity states 82

7.3 Comparative study of the detected timescales of QPOs in different wavelengths 88

7.4 Conclusions 91

A Radiation mechanisms **103**

A.1 Synchrotron radiation 103

A.2 Inverse Compton process 104

B Optical light curves of targets with little data **105**

C Data binning algorithm (One-day binning) **109**

D Discrete Fourier Transform and Lomb-Scargle Periodogram algorithm **111**

D.1 Uploading the data 111

D.2 Discrete Fourier Transform 112

D.3 Lomb-Scargle Periodogram 113

E Discrete Fourier Transform and Lomb-Scargle Periodogram testing algorithm **115**

E.1 First test of DFT and LSP methods – Intermittent synthetic signal with known periods . . 115

E.2 Second test of significance of DFT and LSP – Added noise to original data 123

E.3 Third test of significance of DFT and LSP – Added a periodicity in the original data . . . 124

F Tables of detected timescales of QPOs in optical wavelengths **125**

F.1 Tables of intra-day timescales of QPOs in optical wavelengths 125

F.2 Tables of short-term timescales of QPOs in optical wavelengths 132

G Tables of detected timescales of QPOs in radio wavelengths **135**

G.1 Tables of short-term timescales of QPOs at 37 GHz 135

G.2 Tables of short-term timescales of QPOs at 15 GHz 136

G.3 Tables of short-term timescales of QPOs at 4.8 GHz 138

H Tables of detected timescales of QPOs in X-rays **139**

H.1 Tables of intra-day timescales of QPOs in X-rays 139

H.2 Tables of short-term timescales of QPOs in X-rays 144

Chapter 1

Active Galactic Nuclei

The term *Active Galactic Nucleus* (AGN) refers to a compact region in the center of a galaxy where the luminosity is greater than anticipated based on the stellar population of the host galaxy. This is due to non-thermal energetic phenomena in the nucleus of the galaxy, which cannot be attributed to the physical processes that occur in the stars of the host galaxy (Peterson, 1997; Hayashida, 2008).

In general, there is an upper limit to the luminosity, which is known as *Eddington luminosity*. Eddington luminosity is the maximum luminosity beyond which the radiation pressure will be greater than gravity. It can be calculated by balancing the inward force of gravity against the outward pressure of radiation, assuming spherical accretion. The equation for Eddington luminosity is:

$$L_E = \frac{4\pi G M m_p c}{\sigma_T} \tag{1.1}$$

where G is the gravitational constant, m_p is the mass of a proton, c is the speed of light in vacuum, and σ_T is Thomson cross-section (Longair, 2011).

1.1 Morphology of AGNs

It is widely accepted that *supermassive black holes* (SMBHs), with masses in the range of $10^6 - 10^9 M_\odot$, exist at the center of AGNs (Lynden-Bell, 1969; Gupta, 2014). This theory is based on the Doppler effect, because the motion of the stars near the nuclei of such galaxies indicates that they revolve around great masses and very steep gravity gradients, which suggests the existence of SMBHs. The area surrounding the Schwarzchild radius consists of hot magnetized plasma that is accelerated by the gravitational force of the SMBH, creating a disk, which is known as *accretion disk* (AD) (Syunyaev & Shakura, 1977). The energy source of AGNs is the accretion of gas onto the SMBHs. The radiation is generated outside the *Schwarzchild radius* R_S, due to the friction created by the accreting gas. The Schwarzschild radius and the gravitational radius R_G are given by the equations 1.2:

$$R_S = \frac{2GM}{c^2} \quad , \quad R_G = \frac{GM}{c^2} \tag{1.2}$$

where G is the gravitational constant, M is the mass of the black hole, and c is the speed of light in vacuum. The accretion rate that is needed in order to power an AGN, if the accretion rate is greater than 0.01 of the Eddington accretion rate, is given by:

$$\dot{M} = \frac{L}{\eta c^2} \tag{1.3}$$

where L is the luminosity of the AGN and η is the efficiency factor, which for AGNs is of the order of $\eta \approx 0.1$. The upper limit of the accretion rate, considering a spherical accretion model, can be calculated by using the Eddington luminosity, and thus is given by:

$$\dot{M}_E = \frac{L_E}{\eta c^2} \Rightarrow \dot{M}_E = 2.2 \left(\frac{M}{M_\odot 10^8} \right) M_\odot \, yr^{-1} \tag{1.4}$$

where $M\odot$ is the mass of the Sun (Peterson, 1997).

The magnetic flux is frozen into the accreting material and the field near the horizon can become quite large. Due to the rotation of the AD, the magnetic field lines are twisted, giving rise to an aligned magnetic field, known as *jet* (Blandford & Znajek, 1977; Hayashida, 2008). The direction of the jet depends on the angular velocity of the axis of rotation of its source. The jet consists of plasma that moves with bulk velocities approaching the speed of light. The relativistic jets can be extended up to several tens of megaparsecs from the central black hole. Inside the jet, high energy particles and photons interact with one another and with the magnetic field (Begelman et al., 1984).

The accretion disk ionizes gas clouds that orbit the SMBH at a distance of about 100 light days, which is known as *Broad Line Region* (BLR) (Kaspi et al., 2005; Hayashida, 2008). BLR is a region of rapid gas clouds, with velocities that range from 10^3 to 10^4 Km/s, that produce the broad lines in the spectrum of AGNs, due to Doppler effect. The BLR clouds are optically thick to the ionizing continuum. The variability of the ionizing continuum that drives the emission lines is highly coupled with the variability of the observable continuum (Peterson, 1993). The BLR radius can be calculated, using the Eddington ratio $\lambda = L/L_E$, with the equation (Shen & Loeb, 2010):

$$R_{BLR} \approx 2.2 \cdot 10^{-2} \left(\frac{\lambda_E}{0.1} \right)^{\frac{1}{2}} \left(\frac{M}{10^8 M_\odot} \right)^{\frac{1}{2}} pc \tag{1.5}$$

The BLR is surrounded by a toroidal molecular cloud at a radius of 100 light years, which is known as *Obscuring torus*. The torus is a region of colder gas, that is optically thick, thus shielding the central region of AGN when viewed from the equatorial plane (Hayashida, 2008). Over a 1000 light years radius, there is an extended region, known as *Narrow Line Region* (NLR), where the narrow lines in the spectrum of AGNs are produced. The NLR consists of small cold gas clouds,that have lower density than the clouds of the BLR (Osterbrock & Mathews, 1986; Filippenko, 1986).

A schematic drawing of the structure of an AGN as described above can be seen in Fig. 1.1.

1.2 Unified model of AGNs

Active Galactic Nuclei are classified in two main categories based on the ratio of radio to optical flux, R, known as *radio-loudness*. They are classified as *Radio-Loud AGNs*, if $R > 10$, and as *Radio-Quiet AGNs*, if $R < 10$ (Kellermann et al., 1989). Another classification is based on the morphology of the host galaxy and emission characteristics. The subcategories of AGNs, based on this classification can be seen in Fig. 1.2.

AGNs that are classified as Radio-Loud are *Radio Galaxies*, *Fanaroff-Riley Galaxies*, *Radio-Loud Quasars* and *Blazars*, and as Radio-Quiet are *Radio-Quiet Quasars* and *Seyfert Galaxies* (Antonucci, 1993; Urry & Padovani, 1995).

A unified scheme proposed that the different characteristics of each subclass of AGNs is due to the orientation of the source relative to the line of sight (Urry & Padovani, 1995). Based on this model, AGNs

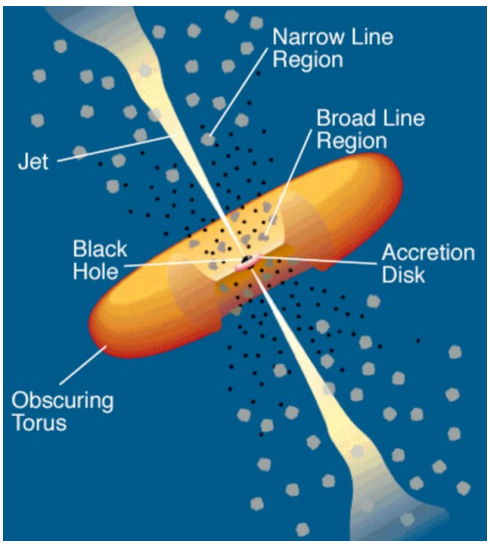

Figure 1.1: A schematic drawing of the structure of an AGN.
Credits: C.M. Urry P. Padovani

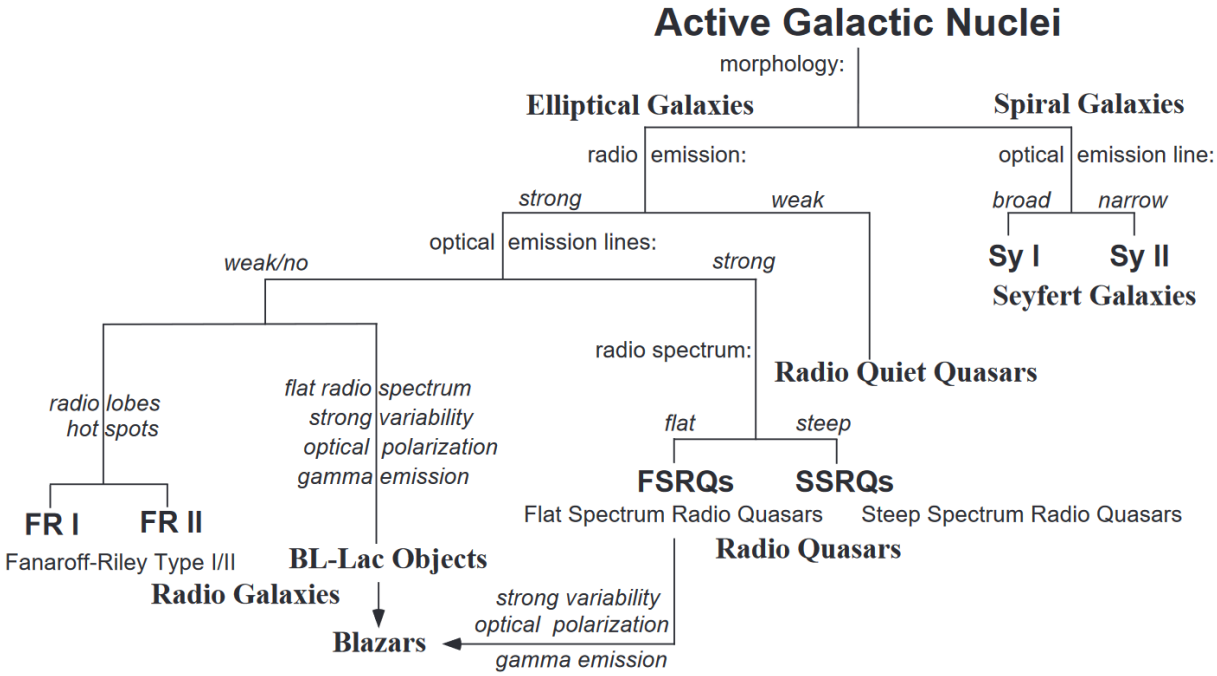

Figure 1.2: Classification of Active Galactic Nuclei (Böttcher, 1997)

with narrow lines on their spectrum are observed from an equatorial view. In this category belong the Fanaroff-Riley galaxies, which are also known as Narrow Line Radio Galaxies (NLRG), and the Seyfert type II galaxies. AGNs with broad lines on their spectrum, such as Seyfert Type I galaxies and Steep Spectrum Radio Quasars (SSRQ), are observed from an intermediate view. Lastly, blazars, which are BL Lac objects or Flat Spectrum Radio Quasars (FSRQ), are AGNs that are observed from a polar view, thus their jets are aligned with our line of sight. A schematic representation of the structure of an AGN and the subclasses based on the line of sight of the observer can be seen in Fig. 1.3

The characteristics of each subclass are briefly described next.

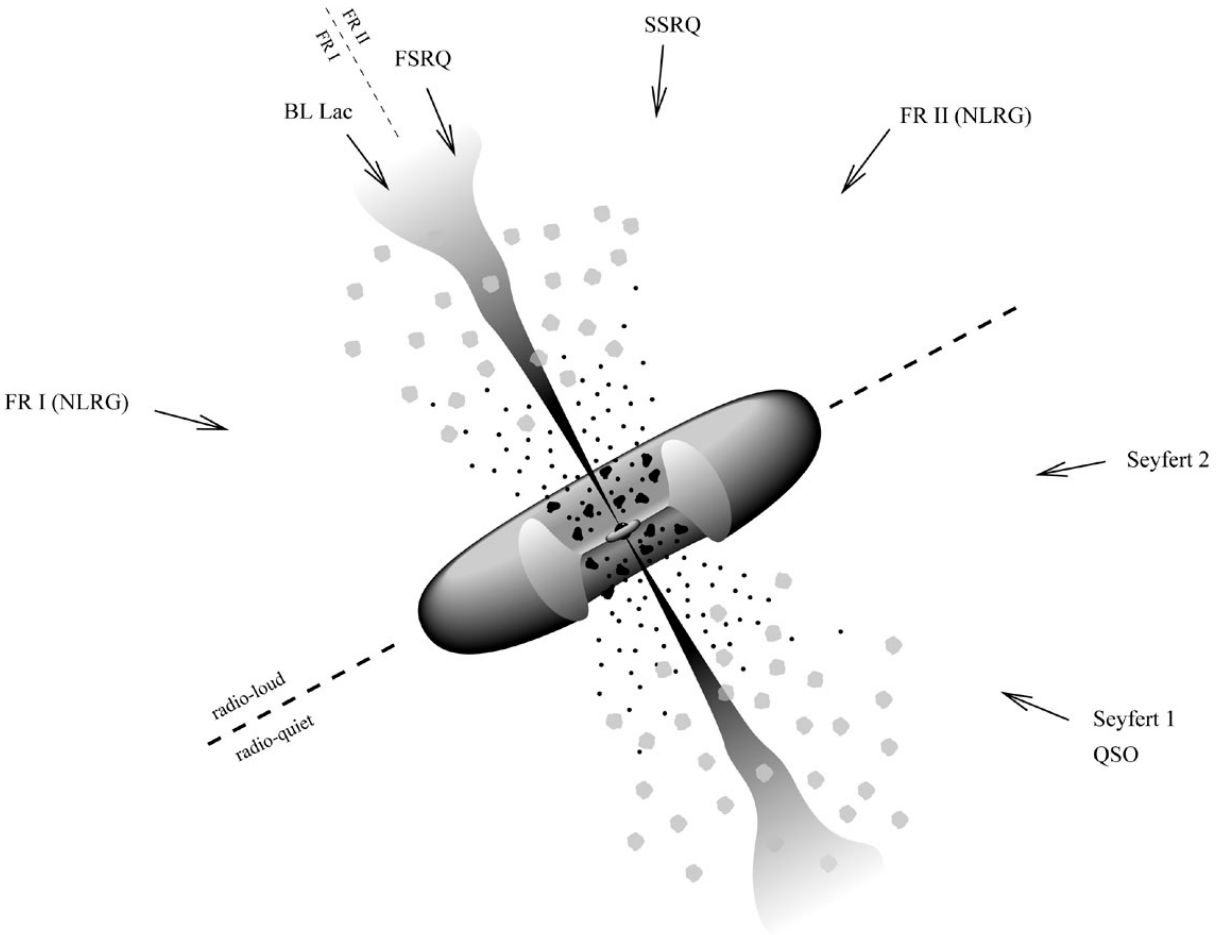

Figure 1.3: Schematic representation of the structure of an AGN and the subclasses based on the line of sight of the observer.

1.2.1 Seyfert galaxies

Seyfert galaxies are lower-luminosity AGNs, that have a very bright nucleus, but the host galaxy can still be observed (Maiolino & Rieke, 1995; Shu, 1982). Morphological studies suggest that their host galaxies are mostly spiral galaxies (Peterson, 1997). Also, unlike typical galaxies that have a thermal continuum with absorption lines, Seyfert galaxies consists of strong emission lines and a non-thermal continuum (Shu, 1982).

The first definition of this subclass was based on morphological characteristics of the galaxy, i.e. galaxies with high surface brightness nuclei (Seyfert, 1943). The identification of Seyfert galaxies now uses not only the morphological characteristic, but also spectroscopic characteristics. Thus as Seyfert galaxy is identified a galaxy that has high surface brightness nucleus and strong, high-ionized emission lines (Peterson, 1997).

There are two distinct subclasses of Seyfert galaxies based on the relative width of the permitted and the forbidden emission lines. *Type I Seyfert galaxies* have Balmer lines broader than the forbidden lines and *Type II Seyfert galaxies* have Balmer lines and forbidden lines of the same width (Khachikian & Weedman, 1974). Type I Seyfert galaxies have two set of emission lines, one set of narrow lines, both in the permitted and forbidden lines, that correspond to low-density ionized gas with velocities of several hundreds kilometers per second, and a set of broad lines, only in the permitted lines, that correspond to high-density gas. On the other hand, type II Seyfert galaxies have only narrow lines in their spectra (Peterson, 1997). This means that type II Seyfert galaxies have lower density emission regions and the emitting gas has greater velocity than type I Seyfert galaxies (Weedman, 1972).

1.2.2 Narrow Line Radio Galaxies

Narrow line radio galaxies are the radio-loud analog of type II Seyfert galaxies, in terms of phenomenology. One of their main difference from Seyfert galaxies is that the host galaxy is elliptical and not spiral (Peterson, 1997). Their main difference is that, as radio-loud galaxies, they have an extended radio structure, which consists of two radio lobes. The radio lobes lie symmetrically to the nucleus and extend for million of light years (Shu, 1982). A radio galaxy can be seen in Fig. 1.4.

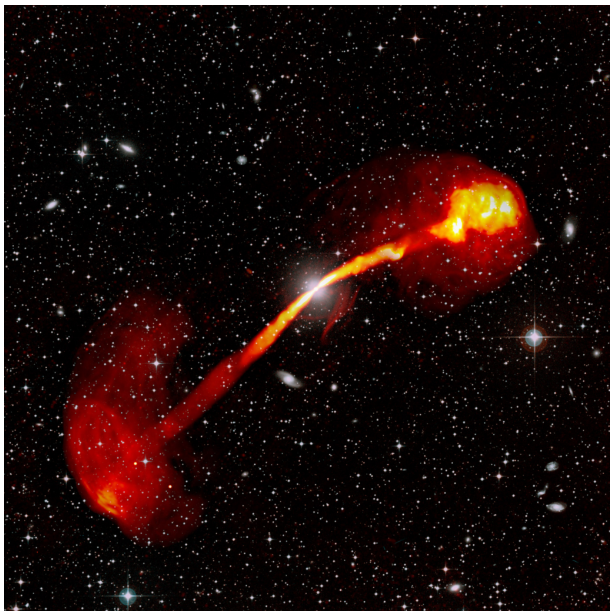

Figure 1.4: The Fanaroff-Riley Type I radio galaxy IC 4296.
Credits: ARAO, SSS, S. Dagnello and W. Cotton (NRAO/AUI/NSF)

NLRGs can be divided in two subcategories, the *Fanaroff-Riley type I (FN I) and type II (FN II) galaxies*. This classification is based on the ratio of the distance between the regions of highest brightness on opposite sides of the nucleus, to the total extend of the source. The sources that have a ratio less than 0.5 are classified as type I, and those with ratio greater than 0.5 as type II (Fanaroff & Riley, 1974). FN I galaxies are weaker radio sources that their brightest regions are near the nucleus, whereas FN II galaxies have high brightness at the edge of the radio structure (Peterson, 1997).

Based on this way of classification, a new way of distinction was proposed based on the Mach number of the sources jet. The FR type I galaxies have jets with low Mach number, thus the turbulence leads to anomalously high surface brightness. The FR type II galaxies, have jets with high Mach number, which means that the jets are supersonic, less turbulent, and terminate with a shock against the intergalactic matter (IGM) (Bicknell, 1985).

1.2.3 Quasars

Quasars were detected as spatially unresolved radio sources, which means that they have angular sizes smaller than $\sim$ 7" (Shu, 1982; Peterson, 1997). Due to their starlike appearance in optical images, they were named Quasi-Stellar Radio Sources or Quasars (QSR) (Chiu, 1964). QSRs are 10% of quasars and are radio-loud AGNs. The 90% of quasars is radio-quiet and are named *Quasi-Stellar Objects (QSO)* (Shu, 1982). A useful criterion to classify a quasar as radio-loud or radio-quiet is the radio to optical ratio R of specific fluxes, in mJy, at 5GHz and 4400Å. Radio-loud sources have a ratio in the range 10-1000, whereas radio-quiet sources have a ratio in the range 0.1-1 (Kellermann et al., 1989).

Quasars have typical luminosities of 10^{47} erg/sec, or about $10^{13} L_{\odot}$ (Perkins, 2009). Those luminosities vary with time, on timescales of some days to several years (Peterson, 1997). The variability of quasars was one of the first properties that was studied in detail, revealing, for the first time, variability on timescales of several years (Smith & Hoffleit, 1963).

Quasars can be found in redshifts from z=0.026 to z=7.527 (Bañados et al., 2018). The majority of quasars have redshift greater than 1, which means that they can be found at great distances, at an early stage of the universe and the evolution of galaxies (Perkins, 2009).

The spectra of quasars have strong, broad emission lines. The strongest observed lines are the hydrogen lines (Balmer-series and Lyman alpha) and the lines of ions in abundance, such as magnesium (Mg_{II}) and carbon (C_{III}, C_{IV}). Due to their redshift, those lines cannot always be observed, because they fall outside of the spectral window of the detector (Peterson, 1997).

1.2.4 Blazars

Blazars are the most active subclass of AGNs. Their jets are aligned with the line of sight, and they are characterized by rapid variability, high and variable polarization, and superluminal velocities (Urry & Padovani, 1995). Those AGNs are named Optically Violently Variables (OVV) Quasars (Peterson, 1997). The term "blazar" is a contraction of BL Lacartae Objects and OVV quasars, and it was proposed by Edward Spiegel in 1978 (Angel & Stockman, 1980).

Blazars are divided in two subcategories, *BL Lacartae Objects (BL Lacs)* and Flat-spectrum radio Quasars (FSRQs), based on their emission lines (Urry & Padovani, 1995). BL Lacs have weak or no emission or absorption lines in their spectra, whereas FSRQs have strong optical emission lines (Peterson, 1997).

BL Lacs are named after the prototype of the class, BL Lacartae (BL Lac), which was originally identified as an irregular variable star. BL Lac was later identified as a radio source, with high variability, radio polarization and unusual microwave spectrum. Also optical images show marginal nebulosity about the source (Schmitt, 1968). FSRQs are highly variable, show high polarization and have radio structures that are dominated by compact radio cores (Fugmann, 1989; Impey et al., 1991; Valtaoja et al., 1992; Wills et al., 1992).

Blazars have emission across the electromagnetic spectrum, from radio to γ-rays. Their spectral energy distributions (SEDs) has a two-bump structure, with one peak at the sub-millimeter to optical wavelengths and one at UV to X-ray energies (Padovani & Giommi, 1995). The SED of a Blazar can be seen in Fig. 1.5.

BL Lacs were mostly diskovered in radio and X-ray energies and thus were divided in two subcategories, *Radio-selected BL Lacs (RBLs)* and *X-ray-selected BL Lacs (XBLs)* (Giommi & Padovani, 1994). The spectra of RBLs shows a smooth rise from radio to optical wavelengths, followed by a sharp cutoff, whereas XBLs are characterised by a smooth rise from radio to X-rays (Giommi et al., 1995). This categorization is based on the selection band and not on an intrinsic physical characteristic of the source and it is not very reliable (Giommi & Padovani, 1994). A new division was proposed based on the shape of the SED. BL Lacs are divided into *Low-frequency peaked BL Lacs (LBLs)* and *High-frequency peaked BL Lacs (HBLs)*. BL Lacs are classified as LBLs if the lower peak of their SED is located at low frequencies (infrared-optical wavelengths), and as HBLs if the lower peak is located at high frequencies (UV, X-rays) (Padovani & Giommi, 1995). The peak frequency is anticorrelated to the X-ray to radio flux ratio (Mao et al., 2005).

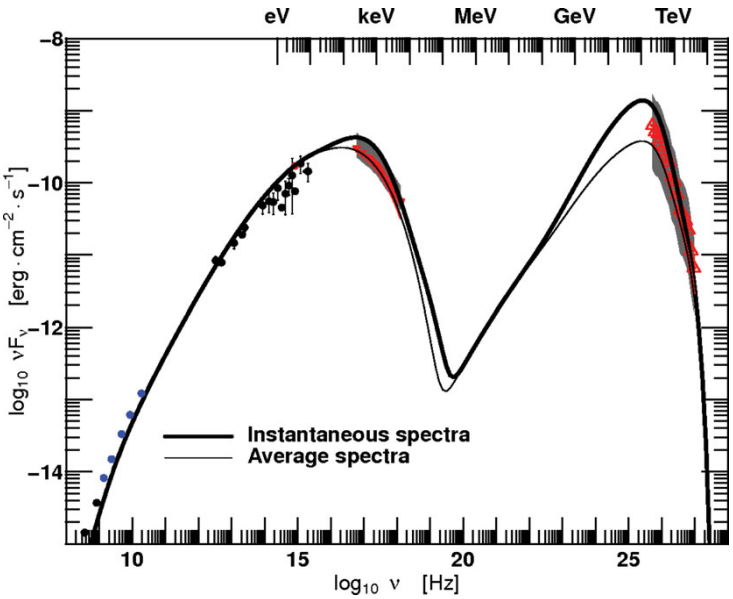

Figure 1.5: Spectral energy distributions (SED) of the blazar PKS 2155-304 during its 2006 highly active state. Red points show nightly average spectra from Chandra and H.E.S.S. data, while the grey band indicates the varying Chandra and H.E.S.S. spectra. Thin and thick solid lines present time dependent synchrotron-self-Compton models able to reproduce the SED (H. E. S. S. Collaboration et al., 2012).

It has been proposed that the blazar subclasses are linked through an evolutionary scenario. This scenario proposes that, due to the gradual depletion of the gas and dust around the SMBH, the accretion power and the accretion-disk radiation declines. The optical emission lines are due to the accretion-disk radiation, thus the declining radiation leads to weaker emission lines. The evolutionary sequence of blazars is: $FSRQs \rightarrow LBLs \rightarrow HBLs$ (Böttcher & Dermer, 2002).

1.3 Variability of AGNs

The variability of AGNs is important in understanding their morphology and the processes that occur in them. The variability of blazars can be divided in three classes:

- Intra-day variability (IDV), with timescales that range from a few minutes to several hours (Wagner & Witzel, 1995).
- Short-term variability (STV), with timescales that range from several days to a few weeks.
- Long-term variability (LTV), with timescales that range from several months up to years (Gupta et al., 2004).

The fluctuations of AGNs luminosity seems non-period, but quasi-periodic oscillations (QPOs), in multiple frequencies, have been observed in the light curves of AGNs (Bhatta, 2017). QPOs have been detected in multiple wavelengths, on different timescales. Some of the timescales of QPOs that have been detected in different wavelengths are listed bellow.

- In radio wavelengths, QPOs with timescales of a few years have been detected (Raiteri et al., 2001; Hovatta et al., 2008; Wang et al., 2014). Also QPOs with periods of several days (Li et al., 2021) and periods of few hours have been observed (Sandrinelli et al., 2016; Liu et al., 2021)

- In optical wavelengths, QPOs have been detected with timescales of few years (Bhatta et al., 2016; Sandrinelli et al., 2016; Zhang et al., 2021), and of a few hours (Gupta et al., 2009).
- In X-rays, QPOs with periods of few seconds to several minutes (Espaillat et al., 2008a; Gierliński et al., 2008).
- In γ-rays, QPOs with periods of few years have been detected (Ackermann et al., 2015; Ait Benkhali et al., 2020).

It is easily seen that QPOs can be detected in every possible class of variability (IDV, STV and LTV). In this thesis, we aim to detect QPOs in different wavelengths, in intra-day and short-term timescales.

1.4 Quasi-periodic oscillations models

Many models have been proposed in order to explain the variability of blazars on different timescales. The models can be divided in two categories, the AD models, that suggest that the fluctuations arise from the AD, and the jet models that suggest that the fluctuations arise from the jet of the AGN.

For blazars, models for IDV involve fluctuations at their jets due to shocks (Wagner & Witzel, 1995) or the helical motion of relativistic blobs (Camenzind & Krockenberger, 1992). Another, more likely model suggests that QPOs detected from the emission of the jet arise from quasi-periodic injection of plasma into the jet from oscillations in the inner region of AD (Mangalam & Wiita, 1993a; Liu et al., 2006; Bhatta, 2019).

In non-blazar AGNs, fluctuations with periods less than a week or IDV may arise from the AD of the AGN (Mangalam & Wiita, 1993b). In optical and UV wavelengths, variability could be a product of processes that take place inside the AD. In X-rays, variability could be connected with the rotation of the AD or other internal processes of the AD. Such fluctuation could happen due to hot-spots or spiral shocks at the AD (Mangalam & Wiita, 1993b; Fukumura & Kazanas, 2008).

In timescales of years, the variability may arise from a binary black hole system. Such periodicities could emanate from radiation that arises in two bubbles of matter that is torn from the AD, when the BH passed through it (Lehto & Valtonen, 1996).

Assuming that the model that suggests that QPOs originate from the accretion disk near the SMBH, the maximum radius of the emitting region can be calculated using the equation:

$$R \leq \frac{c\Delta t_{obs}}{1+z} \tag{1.9}$$

where Δt_{obs} is the timescale of the observed fluctuation, and z is the redshift of the source (Gupta et al., 2012). If the emission comes from the jet of the blazar, it will be Doppler boosted, thus an additional Doppler factor, δ, should be considered in the calculation and equation 1.9 becomes:

$$R \leq \delta\frac{c\Delta t_{obs}}{1+z} \tag{1.10}$$

In case of a non-rotating BH, the emission originates outside the Schwarzchild radius, thus the radius of the emitting region must be greater than the Schwarzchild radius. By comparing equation 1.2 and equation 1.9, we can extract the limit for the mass of the SMBH (non-rotating) is given by the equation:

$$M_{BH} \leq \frac{c^3\Delta t_{obs}}{2G(1+z)} \tag{1.11}$$

If the fluctuation arise from the AD and then propagates along the jet, the emission is Doppler boosted and the Doppler factor should be added in the calculations and the mass of the SMBH is given by (Dai et al., 2007):

$$M_{BH}(\delta) \leq \delta \frac{c^3 \Delta t_{obs}}{2G(1+z)} \tag{1.12}$$

For a maximally spinning SMBH, equations 1.11 and 1.12 change accordingly based on the gravitational radius.

A better estimation of the mass of the SMBH can be calculated in the case of dominant QPOs. Due to the periodicity of the fluctuations, the period is assumed to be related to the orbital timescale of a hot-spot or a shock in the AD (Mangalam & Wiita, 1993a). The minimum timescale of QPO likely corresponds to the marginally stable orbit, R_{ms}, but fluctuations can occur from regions closer to the SMBH (Abramowicz & Nobili, 1982). The radii of the marginally stable orbit, for a non-rotating (left) and a maximally spinning (right) black holes, are (Espaillat et al., 2008b):

$$R_{ms} = \frac{6GM}{c^2} = 6R_G \quad , \quad R_{ms} \simeq 1.2R_G \tag{1.13}$$

The mass of the SMBH can be calculated using the equation:

$$\frac{M}{M_\odot} = \frac{3.23 \times 10^4 P}{(r^{3/2} + \alpha)(1+z)} \tag{1.14}$$

where, $r = R/R_K$, P is the observed period in seconds, α is the angular momentum parameter and z is the redshift. For a non-rotating black hole the angular momentum parameter is $\alpha = 0$ and r=6, and for a maximally rotating black hole the angular momentum parameter is $\alpha = 0.9982$ and r=1.2 (Gupta et al., 2009). In case that the QPOs that arise in the AD propagate along the relativistic jet, the emission is Doppler boosted, thus the Doppler factor, δ, should be added in the calculations and the mass of the SMBH is given by:

$$\frac{M}{M_\odot} = \delta \frac{3.23 \times 10^4 P}{(r^{3/2} + \alpha)(1+z)} \tag{1.15}$$

Equations 1.14 and 1.15 estimate a lower limit for the mass of the SMBH.

1.5 Correlation of flux variations from different wavelengths

The cross-correlation at the light curves of different wavelengths places some additional constrains to the emission models. The flux variations of blazars shows strong correlation (Guise et al., 2022). Many studies have shown correlation between different wavelengths, from microwaves to γ-rays, with lags shorter than a day or with no significant lag (D'Ammando et al., 2013; Zhang et al., 2013). This implies that the sources of the emission of different wavelengths are located at the same region, or at small distances (Guise et al., 2022).

More recent studies show correlation with lags with timescales from 10 to 100 days (Li et al., 2018; Safna et al., 2020). These timescales could imply that there is a distance between the sources of emission from different wavelengths (Guise et al., 2022). Another scenario suggests that if the emission is produced from shocks in the jet of a blazar, the high energy component comes from a region near the shock front, while the lower energy component comes from a further region, thus the delay in the emission (Li et al., 2018).

Chapter 2

Blazar Optical Sky Survey - BOSS Project

Blazar Optical Sky Survey (BOSS) Project is an international observing program, initiated in 2013 at the *Department of Physics*, *University of Athens*. The purpose of the project is the monitoring of blazars, in parallel with observations in different wavelengths from ground-based and space observatories, in order to search for quasi-periodic oscillations in the light curves of AGNs.

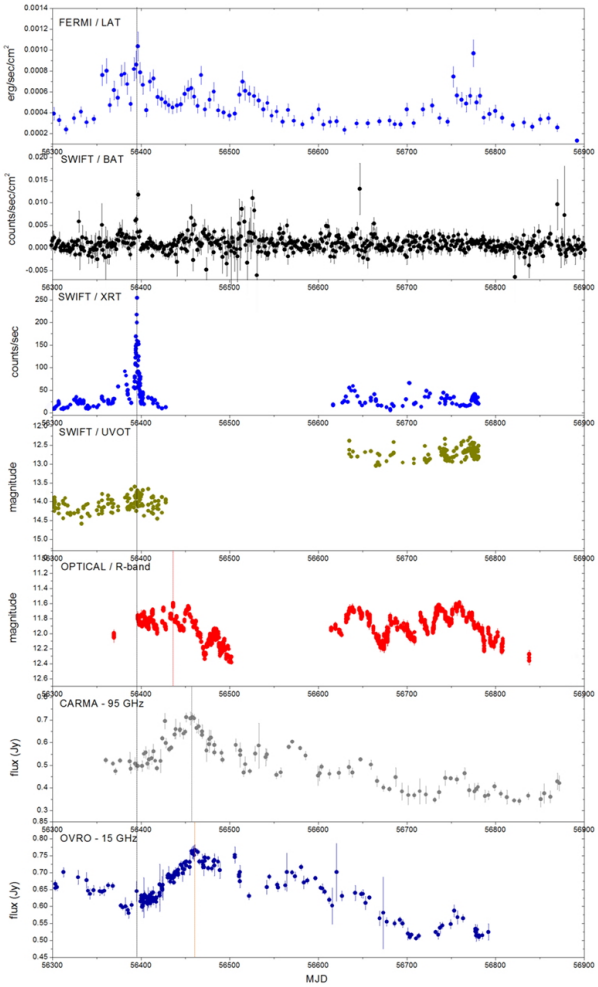

Figure 2.1: Multiwavelength light curves from high to very low energies of Mrk 421 (Gazeas et al., 2015)

This project aims to fill the gap in observations of AGNs in optical wavelengths. The combination of parallel observations from across the electromagnetic spectrum can provide valuable information about the structure and the processes carried out in an AGN. By comparing signals from different wavelengths, we can find the time lag between them and study the mechanisms that cause them. Such a multi-wavelength study was done, in the frame of BOSS Project, for Mrk 421, as shown in Fig. 2.1.

The project involves colleagues from institutes all over the world, such as the Jagiellonian University in Poland, the Owens Valley Radio Observatory (OVRO) in USA, the Xinjiang Astronomical Observatory (XAO) in China, the Aalto University in Finland and the Universität Würzburg in Germany.

2.1 *BOSS Project* targets

The targets that are being observed in the frame of *BOSS Project* are shown in Table 2.1.

Table 2.1: *BOSS Project* target list

Target	**Other Name**	**RA (J2000)**	**DEC (J2000)**	**Mag.**	**Comments**
Mrk1018	PGC 8029	02:06:16	-00:17:29	10.3 mag	Seyfert 1 Galaxy
1ES 0236+61	LS I +61 303	02:40:32	+61:13:42	10.2 mag	HMXB (V615 Cas)
1H 0323+342	PGC 2045127	03:24:41	+34:10:46	13.1 mag	Seyfert 1 Galaxy
PKS 0420-014	QSO B0420-0127	04:23:16	-01:20:33	17.0 mag	Quasar (FSRQ)
PKS 0716+714	GSC 4368:0899	07:21:54	+71:19:21	14.3 mag	Blazar (BL Lac Object)
1ES 0836+71	QSO B0836+71	08:41:24	+70:53:42	16.8 mag	Quasar
OJ 287	GSC 1400:0230	08:54:49	+20:06:30	14.1 mag	Blazar (BL Lac Object)
Mrk110	PGC 26709	09:25:13	+52:17:11	15.2 mag	Seyfert 1 Galaxy
PKS 0925+504	QSO J0929+5013	09:29:15	+50:13:36	15.9 mag	Blazar (BL Lac Object)
PKS 0954+658	S4 0954+658	09:58:47	+65:33:55	15.8 mag	Blazar (BL Lac Object)
Mrk421	PGC 33452	11:04:27	+38:12:31	8.3 mag	Blazar (BL Lac Object)
Mrk180	PGC 35899	11:36:26	+70:09:28	14.5 mag	Blazar (BL Lac Object)
3C 273	PGC 41121	12:29:07	+02:03:09	14.1 mag	Blazar (BL Lac Object)
3C 279	PGC 2817645	12:56:11	-05:47:22	15.9mag	Quasar (FSRQ)
PKS 1510-089	PGC 2828331	15:12:51	-09:06:00	16.5 mag	Quasar (FSRQ)
PKS 1553+113	GSC 0947:1098	15:55:43	+11:11:24	14.6 mag	Blazar (BL Lac Object)
Mrk501	PGC 59214	16:53:52	+39:45:36	13.3 mag	Blazar (BL Lac Object)
1ES 1959+650	PGC 2674942	20:00:00	+65:08:55	11.2 mag	Blazar (BL Lac Object)
BL Lac	1ES 2200+42.0	22:02:43	+42:16:40	14.7 mag	Blazar (prototype)
CTA102 (4C 11.69)	PGC 2819036	22:32:36	+11:43:51	16.7 mag	Quasar (FSRQ)
3C 454.3	PGC 2819327	22:53:58	+16:08:54	15.2 mag	Quasar (FSRQ)
1ES 2344+514	QSO B2344+514	23:47:05	+51:42:18	15.5 mag	Blazar (BL Lac Object)

Most of the *BOSS Project* targets are blazars, but targets from other subclasses of AGNs have been observed due to their powerful emission in optical wavelengths. Some of the characteristics of each of the targets are listed below.

Mrk 1018

Mrk 1018 is a Seyfert Galaxy (Keel, 1980) at z=0.043(McElroy et al., 2016). It is a changing-look AGN, because its high-amplitude continuum fluctuation is associated with the presence of the optical broad emission lines (Miniutti et al., 2019). Around 1980 and in a course of less than 5 years, observations show that Mrk 1018 brightened and displayed strong broad emission lines, changing from Seyfert type 1.9 to Seyfert type 1 (Cohen et al., 1986). In 2010, the broad emission lines almost disappeared and Mrk 1018 returned to its previous classification as a Seyfert Type 1.9 Galaxy (McElroy et al., 2016).

1ES 0236+61

1ES 0236+61 is a High Mass X-ray Binary (HMXB) at a redshift of z=0.00014 (Taylor et al., 1992). It was first detected as a gamma-ray source in 1977 (Hermsen et al., 1977), but later a periodic signal of 26.52 days was detected in radio (Taylor & Gregory, 1982). Based on the luminosity, the spectral slope and the detection of QPOs in X-rays and radio, it is believed that 1ES 0236+61 is a microquasar (Chernyakova et al., 2019). Multiwavelength observation in TeV energies, from MAGIC and VERITAS, and in X-rays, from XMM-Newton and Swift/XRT, show a correlation between the data, but there is no correlation between emissions in TeV and GeV energies (Anderhub et al., 2009; Aliu et al., 2013).

1H 0323+342

1H 0323+342 is a Seyfert Type I galaxy with narrow emission lines at a redshift of z=0.063 (Berton et al., 2019) with a mass of the order of $10^7 M_\odot$ (Zhou et al., 2007). Images from the VLBI, at 15GHz, has shown a strong radio core at the end of a one-sided jet (Lister & Homan, 2005). Observations in optical wavelengths have lead to the detection of intra-day variability of the order of 30 minutes (Paliya et al., 2014).

PKS 0420-014

PKS 0420-014 is a flat spectrum radio quasar (Healey et al., 2008) at redshift of z=0.916 (Jones et al., 2009), with a SMBH of $7.9 \times 10^8 M_\odot$ (Liang & Liu, 2003). In optical wavelengths a two mode variability has been revealed, with a variability of 13 months with a flare lasting one month, superimposed with a variability of shorter timescales from 1 to 10 days, also an IDV of 3 hours has been detected (Wagner et al., 1995). In radio wavenlengths, a similar variability of 13 months has been suggested using observations from VLBI (Britzen et al., 2000).

PKS 0716+714

PKS 0716+714 is a BL Lac object (Kühr et al., 1981) at redshift of $z = 0.31 \pm 0.08$ (Nilsson et al., 2008). Until 2009, five flares had been detected in optical wavelengths at the beginning of 1995, the end of 1997, the autumn of 2001, on March 2004 and the beginning of 2007 (Raiteri et al., 2003; Foschini et al., 2006; Gupta et al., 2008). These flares show that a long-term variability (LTV) of 3 ± 0.3 years exists in optical wavelengths. A short-term variability of 7 days, and an intra-day variability of 25-73 minutes have also been detected (Gupta et al., 2009). In radio wavelengths, a periodicity of 5.5-6 years has been found (Villata et al., 2008).

1ES 0836+71

1ES 0836+71 is a quasar (Kühr et al., 1981) at a redshift of z=2.21, with a mass of $(2.0 \pm 0.7) \times 10^9 M_\odot$ (Raiteri et al., 2020). Until 2015, two flares had been observed in gamma rays, the first one on April 2011, when the flux was 25 times greater than the mean flux (Ciprini & Dutka, 2011), and on March 2015, when the flux was 65 times greater than the mean flux (Ciprini & Fermi Large Area Telescope Collaboration, 2015). Also a fast gamma ray flux rising time of ~ 3 hours has been detected (Paliya & Vaidehi, 2015).

OJ287

OJ287 is a BL Lac object at a redshift z=0.306 (Sitko & Junkkarinen, 1985). In optical wavelenghts, double flares have been observed, that have a periodicity of about 12 years (Sillanpää et al., 1988). Periodicities of 40-50 days have been observed in optical and radio wavelengths (Pihajoki et al., 2013; Wu et al., 2006). A long-term variability of 435 days has been detected in the optical–near-infrared bands, and of 410 days in gamma rays (Sandrinelli et al., 2016).

Mrk 110

Mrk 110 is a Seyfert Type I galaxy (Adams & Weedman, 1975) at a redshift of z=0.035 (Boller et al., 2007), with a mass of $(1.4 \pm 0.3) \times 10^8 M_\odot$ (Kollatschny, 2003). One day observations in 1996 detected an 0.07 mag rise in the lightcurve of Mrk 110 in 1.5 hours and then a decline and rise of 0.05 mag in 1.7 hours (Jang & Miller, 1997). Fluctuations have also been observed in the line profile of Mrk 110. The He II $\lambda 4686$ line follows the continuum variations with a lag of 5 days, and the Balmer lines with a delay of 23 days (Kollatschny & Welsh, 2001).

PKS 0925+504

PKS 0925+504 is a BL Lac object (Nass et al., 1996) at a redshift of z=0.370 (Abazajian et al., 2009).A rapid intra-day variability has been detected on 4.9 GHz, from VLA observation in 2002-2003 (Lovell et al., 2008). In radio wavelengths, IDVs with a timescale of 0.5 ± 0.1 days have also been detected, and short term variability of 250-300 days (Liu & Liu, 2015). In optical wavelengths, fluctuations with a period of 0.3 ± 0.1 days have been detected (Liu et al., 2017).

PKS 0954+658

PKS 0954+658 is a BL Lac objects at a redshift of z=0.367 (Stickel et al., 1993). A correlation between the light curves of radio and optical wavelengths has been detected (Wagner et al., 1993). In 2015, the magnitude of R-band rose from ~16-17 mag to ~13 mag (Spiridonova et al., 2015). Also, in optical wavelengths, rapid fluctuations of 0.1 mag have been detected with a period of the order of 10 minutes (Gaur et al., 2019).

Mrk 421

Mrk 421 is a BL Lac object (Ulrich, 1978) at a redshift of z=0.031 (Mao, 2011). The light curves of radio and optical wavelengths are strongly correlated (Lindfors et al., 2016), also a significant correlation has been detected between gamma rays and radio wavelengths, during a flare in 2012 (Hovatta et al., 2015). Short term variability has been detected in different energy bands. In gamma rays a period of 280 days has been detected (Bhatta & Dhital, 2020), in radio wavelengths (15 GHz) a periodicity of 287.6 ± 4.4 days has been found, and in X-rays an STV of 309.5 ± 5.8 days has been detected (Li et al., 2016). In energies from 3 to 79 keV (X-rays), intra-day variability with period of 14.01 ± 5.03 minutes has been found (Paliya & Vaidehi, 2015).

Mrk 180

Mrk 180 is a BL Lac object at a redshift of z=0.046 (Ulrich, 1978). Between 2008 and 2009 it was on a high-flux state, with its peak luminosity changing between $10^{43.5}$ to $10^{44.5}$ $erg\ s^{-1}$ (Wang et al., 2019). The light curves of optical and radio wavelengths show increasing trends for several years. The flares observed in optical wavelengths can be detected in radio light curves. This means that a correlation exists between the two energy bands and also that the fluctuations originate from the same region (Lindfors et al., 2016).

3C 273

3C 273 is a BL Lac object at a redshift of z=0.158 (Strauss et al., 1992). It has been observed across the spectrum, from radio to gamma rays, and it has shown variability in different timescales. In optical wavelengths an intra-day variability of 13-245 minutes has been detected (Fan et al., 2009). Also variabilities of 23.9 to 744 days have been found (Dai et al., 2009; Fan

et al., 2014). In X-rays, an IDV of ~3300 seconds has been detected (Espaillat et al., 2008b).

3C 279

3C 279 is a flat spectrum radio quasar at a redshift of z=0.536 (Beckmann et al., 2006). It shows fluctuations across the spectrum from radio wavelengths to gamma rays (Burbidge & Rosenberg, 1965). In optical wavelengths, IDV with timescales from 23 to 115 minutes have been detected (Agarwal et al., 2019). In near-infrared–optical bands and in gamma rays, STV of 24 days has been found (Sandrinelli et al., 2016). Correlation between different energy bands has been detected. Between the radio and optical light curves a lag of 12.8 days has been found (Böttcher et al., 2007), between optical wavelengths and gamma rays a lag of 1.06 ± 0.47 days, and between the light curves of X-rays and gamma rays a lag of 0.24 ± 0.42 days (Larionov et al., 2020).

PKS 1510-089

PKS 1510-089 is a flat spectrum radio quasar at a redshift of z=0.361 (Hawkins, 1978). In the begging of 2009, flares in gamma rays, X-rays, radio and optical wavelengths were observed (Marscher et al., 2010; Abdo et al., 2010; D'Ammando et al., 2011). In 2011, a flare in radio wavelengths was observed, that was correlated with the high activity state in gamma rays (Aleksić et al., 2014). During the flare, the fluctuations in gamma rays showed a periodicity of the order of 20 minutes (Foschini et al., 2013).

PKS 1553+113

PKS 1553+113 is a BL Lac object at a redshift of z=0.36 (Miller & Green, 1983). The optical light curves show many flares (Lindfors et al., 2016), and a STV of 754 ± 20 days has been observed. In gamma rays, a variability of 2.18 ± 0.08 years has been detected (Ackermann et al., 2015). Additionally, a correlation between radio and gamma ray lightcurves has been found, with a time lag of 50 ± 20 days (Ackermann et al., 2015).

Mrk 501

Mrk 501 is a BL Lac object at a redshift of z=0.034 (Ulrich, 1978). During a flare in gamma rays in 1997, observations showed a variability of 23 days (Rieger & Mannheim, 2000). Other researches have found periodicities of 72 days (Rödig et al., 2009) and 330 days in gamma rays (Bhatta, 2019).

1ES 1959+650

1ES 1959+650 is a BL Lac object at a redshift of z=0.048 (Perlman et al., 1996). Its radio and optical light curves show similar flaring behavior, but there is not a significant correlation between the two wavelengths (Lindfors et al., 2016). In radio wavelengths a variability of 370 days was found, but with low significance (Li et al., 2017). In R-band (optical), a STV with a period of 266.2 ± 7.3 days has been detected (Li et al., 2022).

BL Lac

BL Lac is the prototype of the subclass of blazars. It is at a redshift of z=0.069 (Mao, 2011). It has been observed that it has a variability with period of 270, 520 and 750 days in gamma rays (Bhatta & Dhital, 2020). Also in optical wavelengths there is a variability of 670 ± 40 days (Sandrinelli et al., 2017). In radio wavelengths LTV with a period of 8 years has been detected. Also a correlation between the radio and optical light curves has been found, with a time lag of 540 days (Villata et al., 2004).

CTA 102

CTA 102 is a flat spectrum radio quasar at a redshoft of z=1.032 (Schmidt, 1965). Until 2017 two flaring events had been observed, in 2012, when the magnitude rose from 17-18 mag to 13 mag was observed (Larionov et al., 2016), and in 2016 when it rose up to 11 mag (Calcidese et al., 2016). During these two events, IDV that reached 0.2 mag were detected in timescales of the order of 30 minutes (Bachev et al., 2017).

3C 454.3

3C 454.3 is a flat spectrum radio quasar at a redshift of z=0.859 (Penston & Cannon, 1969). In V-band (optical), fluctuations of 0.06 mag has been detected with a period of 1.7 hours (Raiteri et al., 1998), and in R-band (optical) a variation of 0.27 mag in 2.6 hours has been found (Villata et al., 1997). In B-band, observations have shown STV of 0.83, 2.97 and 6.39 years (Webb et al., 1988). Recent studies have found a QPO of 47 days in gamma rays and in optical wavelengths (Sarkar et al., 2021). Also a correlation between X-rays and ultraviolet (UV) has been detected, with the X-ray variations preceding the UV by 98 days (Zhou et al., 2021).

1ES 2344+514

1ES 2344+514 is a BL Lac object at a redshift of z=0.044 (Perlman et al., 1996). Observations have shown a variability of 5000 seconds in X-rays (Giommi et al., 2000). Fluctuations of similar timescales have been detected in the R-band (optical), with a period of 4738 seconds, thus a correlation between the two wavelengths must exist (Ma et al., 2010). Also a correlation of radio and optical wavelengths has been detected, with optical leading radio by 70 days (Lindfors et al., 2016).

A multi-wavelength Astronomy approach was used to study these target, with the exception of PKS 0420-014, in order to compare the results and find correlations between the different wavelengths. The targets were studied in 5 energy bands from 2013 to 2021.

Chapter 3

Data analysis

In order to search for quasi-periodic oscillations from timescales of few minutes to several months the Discrete Fourier Transform (DFT) and the Lomb-Scargle Periodogram (LSP) were implemented, these methods are briefly discussed next.

3.1 Fourier Analysis

Fourier analysis is the method of representing or approximating general functions using a sum of periodic trigonometric functions. Fourier transform is a mathematical transform that decomposes a signal, which is a time dependent function, into functions of temporal frequency, thus allowing the calculation of the period of the QPOs. The Fourier decomposition of function f(t) is:

$$f(t) = \frac{\alpha_o}{2} + \sum_{n=1}^{\infty}(\alpha_n \cdot cos(n\omega t) + b_n \cdot sin(n\omega t)) \tag{3.1}$$

where α_n and b_n are complex values that represent the signal.

In the frame of this thesis, the program *Period04* (P04) was used, that performs Discrete Fourier Transform (Lenz & Breger, 2005). In this program, we import the data and set the limit of frequency that it will search for oscillations. Also Discrete Fourier Transform was applied using an algorithm of Fast Fourier Transform (FFT) developed in *Python* environment, the algorithm can be found in the Appendix D.

Fourier transform is one of the most used methods implemented in order to search for periodic signals in astronomical observations. It can represent non periodic signals with high accuracy when the data are evenly spaced, but can give results even in cases when the data are not evenly spaced, but with lower accuracy. The data used for the search of QPOs of intra-day timescales are evenly spaced and therefore DFT can provide reliable results. In the case of short-term timescales the data series include several time-gaps and the results should be used with caution. However, the results extracted with DFT can be compared with other methods (see below) in order to cross-check the validity of the method.

3.2 Lomb-Scargle Periodogram

The Lomb-Scargle Periodogram (Lomb, 1976; Scargle, 1982) is an algorithm that can detect periodicity in unevenly spaced data. The function modelling the signal based on the periodogram is:

$$d(t_i) = Acos(2\pi f t_i - \theta) + Bsin(2\pi f t_i - \theta) + n \tag{3.2}$$

where d is the data in time t_i, A and B are the amplitudes of the trigonometric functions that describe the signal, f is the frequency, n is the noise, and θ is a phase that is used to orthogonize the trigonometric expression in case of uneven data (Lomb, 1976). The phase θ is given by equation 3.3.

$$\theta = \frac{1}{2} arctan\left(\sum_{i=1}^{N} sin(4\pi f t_i), \sum_{i=1}^{N} cos(4\pi f t_i)\right) \tag{3.3}$$

The power spectral density of the periodogram is given by:

$$P(\omega) = \frac{1}{2\sigma^2}\left(\frac{R(\omega)^2}{C(\omega)} + \frac{I(\omega)^2}{S(\omega)}\right) \tag{3.4}$$

where:

$$R(\omega) = \sum_{i=1}^{N} d(t_i) cos(2\pi t_i - \theta) \tag{3.5}$$

$$I(\omega) = \sum_{i=1}^{N} d(t_i) sin(2\pi t_i - \theta) \tag{3.6}$$

$$C(\omega) = \sum_{i=1}^{N} cos^2(2\pi t_i - \theta) \tag{3.7}$$

$$S(\omega) = \sum_{i=1}^{N} sin^2(2\pi t_i - \theta) \tag{3.8}$$

and σ^2 is the variance of the data (Hocke & Kämpfer, 2009).

The Lomb-Scargle Periodogram algorithm that was used in the frame of the analysis can be found in the Appendix D.

A confidence threshold of 99% in QPO detection was set, in order to ensure the significance of the detected signal. In order to calculate the confidence level, we used a method based on gamma distribution for the DFT method and a method based on normal distribution for the LSP method. Moreover, signals that have been detected with at least two methods are considered significant. Signals which are detected within a range of 5 minutes (for IDV) and 5 days (for STV) were considered to represent the same QPO, based on the data cadence and the observation method.

An example of the implementation of the above methodology is given below, where we search for QPOs of intra-day timescales in the light curve of BL Lac on JD 2457999. The total duration of the observations is 8.4 hours (502.8 minutes).

The light curve that was analysed can be seen in Fig. 3.1.

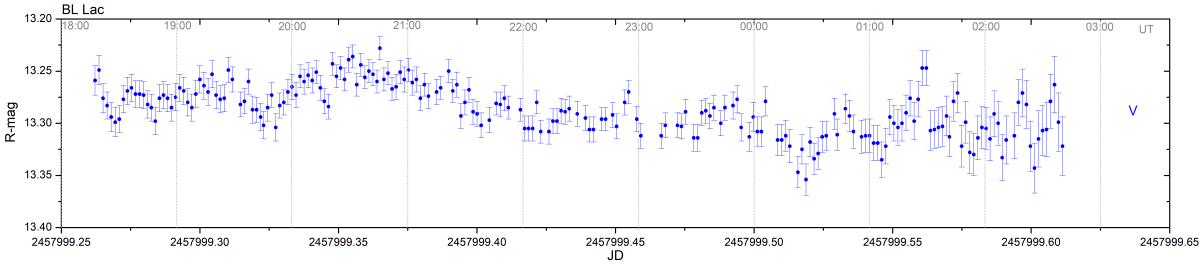

Figure 3.1: Photometric optical light curves of BL Lac on JD 2457999.

The frequency limits for the search of IDV are set based on the observations (i.e. cadence and duration). Due to the fact that most observations have an exposure time of 180 sec, the upper limit of frequency is 200 cycles per day (cpd), which corresponds to a period of 7.2 minutes, because we need at least 2 points in order to fit a function to our data. The lower limit is set as 1/t (cpd), where t is the total duration of the observations (in days). The range of reliability of the detected frequencies is set from 2/t cpd, in order to detect at least two oscillations during the observations, to 100 cpd, which corresponds to 15 minutes, because we need at least 5 to 6 points to fit the trigonometric functions. In this case we are searching for periods from 15 minutes to 4 hours.

The discrete Fourier power spectrum extracted from the implementation of DFT using the Period04 software can be seen in Fig. 3.2.

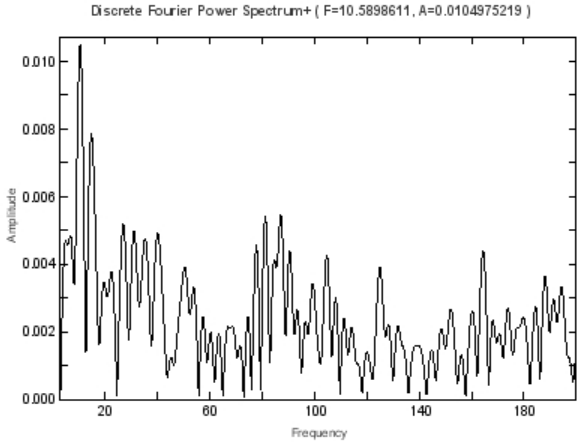

Figure 3.2: Discrete Fourier power spectrum for JD 2457999.

The Discrete Fourier power spectrum of the DFT implemented using *Python* environment, and the Lomb-Scargle periodogram can be found in Fig. 3.3.

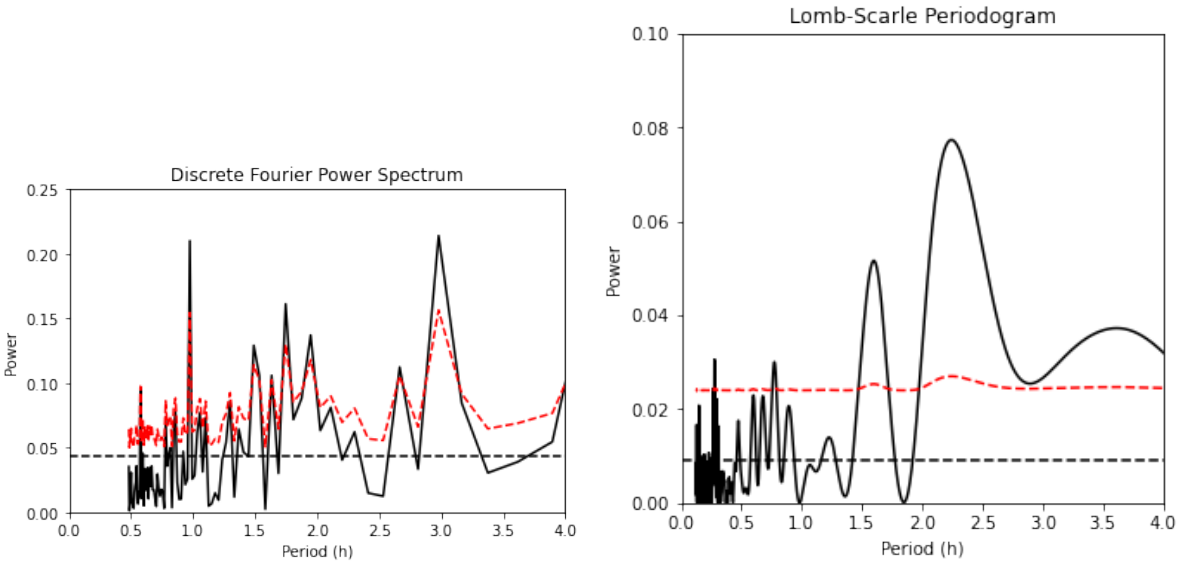

Figure 3.3: Discrete Fourier power spectrum (left) and Lomb-Scargle Periodogram (right) exported from *Python* algorithm for JD 2457999. With black dashed line we see the level of noise of the detected periods, which was estimated through the power spectral density over the range of frequencies. With red dashed lines is the 99% confidence level computed using the gamma and normal distribution accordingly and with black dashed line is the level of noise of the detected frequencies.

Although many periods have been detected, only few are above the threshold of 99% confidence.

The detected timescales of QPOs in the light curve of BL Lac of JD 2457999, with at least 99% confidence in detection, can be found in table 3.1.

Table 3.1: Period of the detected IDVs in the optical light curve of BL Lac on JD 2457999.

JD	Duration (min)	Discrete Fourier Transform (P04)			Fast Fourier Transform (Python)			Lomb-Scargle Periodogram		
		Period (min)	Amplitude	S/N	Period (min)	Amplitude	S/N	Period (min)	Amplitude	S/N
2457999	502.78	135.98±3.77	0.011±0.002	13.3	98.01	0.006	2.4	134.59	0.28	8.5
		17.74±0.15	0.005±0.002	3.0				95.89	0.23	5.6
		15.91±0.10	0.006±0.002	3.1				16.53	0.17	3.3
								15.88	0.16	2.7

The signal to noise ratio (S/N) was calculated by dividing the amplitude of the detected period with the value of the noise of the power spectrum.

The above analysis was implemented throughout the current study, in order to search for QPOs of different timescales in different wavelengths.

Chapter 4

Search for QPOs in optical wavelengths

4.1 Observations and data reduction

4.1.1 University of Athens Observatory (UOAO)

In the frame of *BOSS Project* and the present thesis, observations in optical wavelengths have been conducted by the *University of Athens Observatory* (*UOAO*). The *UOAO* hosts a 0.4 m *Cassegrain* telescope with a secondary mirror of 0.15 m. The focal ratio of the primary mirror is f/3, and the effective focal ratio is f/8 for the telescope, thus its focal length is 3.2 m. It is the first robotic and fully remote controlled telescope operating in a Greek educational institute (Gazeas, 2016).

Figure 4.1: The University of Athens Observatory and the 0.4 m Cassegrain telescope.

The telescope is equipped with an imaging CCD camera ST-10XME (SBIG) and a set of Bessell filters (UBVRI). CCD image sensors are used in digital imaging because they have a high quantum efficiency, great resolution, high photometric accuracy, and low electromagnetic noise.

The *UOAO* is used both for research and educational purposes. The observatory collaborates with institutes from all around the world in the frame of international campaigns, such as the *Whole Earth Blazar Telescope* (*WEBT*) network. This is an international monitoring campaign for AGNs in multiple wavelengths (optical, near-infrared, and radio). The *University of Athens Observatory* has provided data in optical wavelengths to the *WEBT campaign* in the frame of *BOSS Project*, which was discussed in the previous chapter.

For the current thesis, data in optical wavelength from 2013 to 2021 were provided by the *University of Athens Observatory*. The targets were observed in R-filter (Bessell prescription, (Bessell, 1990)). The number of nights, the total number of images and the exposure time for each target can be found in table 4.1.

Table 4.1: Observing information of the *BOSS Project* targets.

Target	Number of nights	Number of observations	Exposure time (sec)
Mrk1018	6	27	180
1ES 0236+61	17	925	40, 60
1H 0323+342	13	78	180
PKS 0716+714	21	757	120, 180
1ES 0836+71	8	233	180, 240
OJ 287	1478	35333	180
Mrk110	43	253	180
PKS 0925+504	9	83	180
PKS 0954+658	12	241	180
Mrk421	700	16097	120, 180
Mrk180	277	1232	180
3C 273	15	63	120, 180
3C 279	17	167	120, 180
PKS 1510-089	9	231	120,180
PKS 1553+113	2	11	180
Mrk501	176	1011	120, 180, 240
1ES 1959+650	11	139	120, 180
BL Lac	569	9957	120, 180
CTA102	13	101	60, 180
3C 454.3	12	77	180
1ES 2344+514	14	47	180

4.1.2 Data reduction

The acquired raw images were calibrated using *bias*, *dark*, and *flat* correction frames. Bias frames are images that are obtained with zero exposure time and dark background, they contain the noise from the electronics of the CCD sensor. Dark frames are images that are obtained with a dark background and the exposure time and temperature of the sensor are the same as the ones of the raw image that needs calibration. They are used to subtract the noise produced by the sensor due to dark current and the fixed-pattern noise. Flat-field frames are images that are acquired in a uniformly illuminated background with short exposure time. They are used to correct the raw image from effects due to distortions in the optical path (i.e. dust grains) and from vignetting in the perimeter of the image. The standard method for the correction of the raw images follows equation 3.1.

$$Calibrated = \frac{raw \ - \ dark}{flat \ field} \tag{3.1}$$

Differential photometry was conducted utilizing differential (aperture) photometry techniques (C-MUNIPACK software [1]) (Hroch, 1998). The method of differential photometry uses comparison stars (comparison and check star) of known magnitude that are in the same field as the

[1] http://c-munipack.sourceforge.net/

target in order to export the magnitude of the target. The main advantage of this method is that results can be extracted even if the observing conditions are not ideal.

The observed targets and their comparison stars can be found in table 4.2. Photometric data for OJ 287 were provided by Dr. Zola.

Table 4.2: The observed AGNs and the comparison stars used for differential photometry.

Target	**Comparison star**	**R-mag**	**Check star**	**R-mag**
Mrk1018	GSC 4689:0752	15.28	GSC 4689:1217	14.26
1H 0323+342	GSC 2349:1649	12.42	GSC 2349:1333	13.40
PKS 0716+714	GSC 4368:0930	12.06	GSC 4368:1196	13.26
1ES 0836+71	GSC 4378:1285	13.73	GSC 4378:0595	13.99
Mrk110	GSC 3431:1243	13.17	GSC 3431:1266	13.52
PKS 0925+504	GSC 3431:0005	14.16	GSC 3431:0006	13.89
PKS 0954+658	GSC 4143:0922	12.55	GSC 4143:0852	12.74
Mrk421	GSC 3010:0688	12.21	GSC 3010:0762	12.76
Mrk180	GSC 4395:1040	13.44	GSC 4395:1328	13.51
3C 273	GSC 0282:0283	12.87	GSC 0282:0423	12.20
3C 279	GSC 4956:1119	12.25	GSC 4956:1057	14.05
PKS 1510-089	GSC 5581:0002	11.55	GSC 5581:0061	13.01
PKS 1553+113	GSC 0947:1188	11.90	GSC 0947:1248	13.00
Mrk501	GSC 3075:1227	13.12	GSC 3075:1005	12.79
1ES 1959+650	GSC 4240:0849	12.90	GSC 4239:0597	12.70
BL Lac	GSC 3206:1597	12.43	GSC 3206:1087	12.10
CTA102	GSC 1154:0763	13.57	GSC 1154:0252	12.41
3C 454.3	GSC 1698:0572	13.67	GSC 1698:1358	13.23
1ES 2344+514	GSC 3650:1106	12.25	2MASS 23472385+5143494	14.20

The light curves of the observed Active Galactic Nuclei between 2013 and 2021 are plotted below. In order to plot the light curves the data are grouped in one-day bins. In Appendix B, the zoomed in light curves of the target with few points can be found.

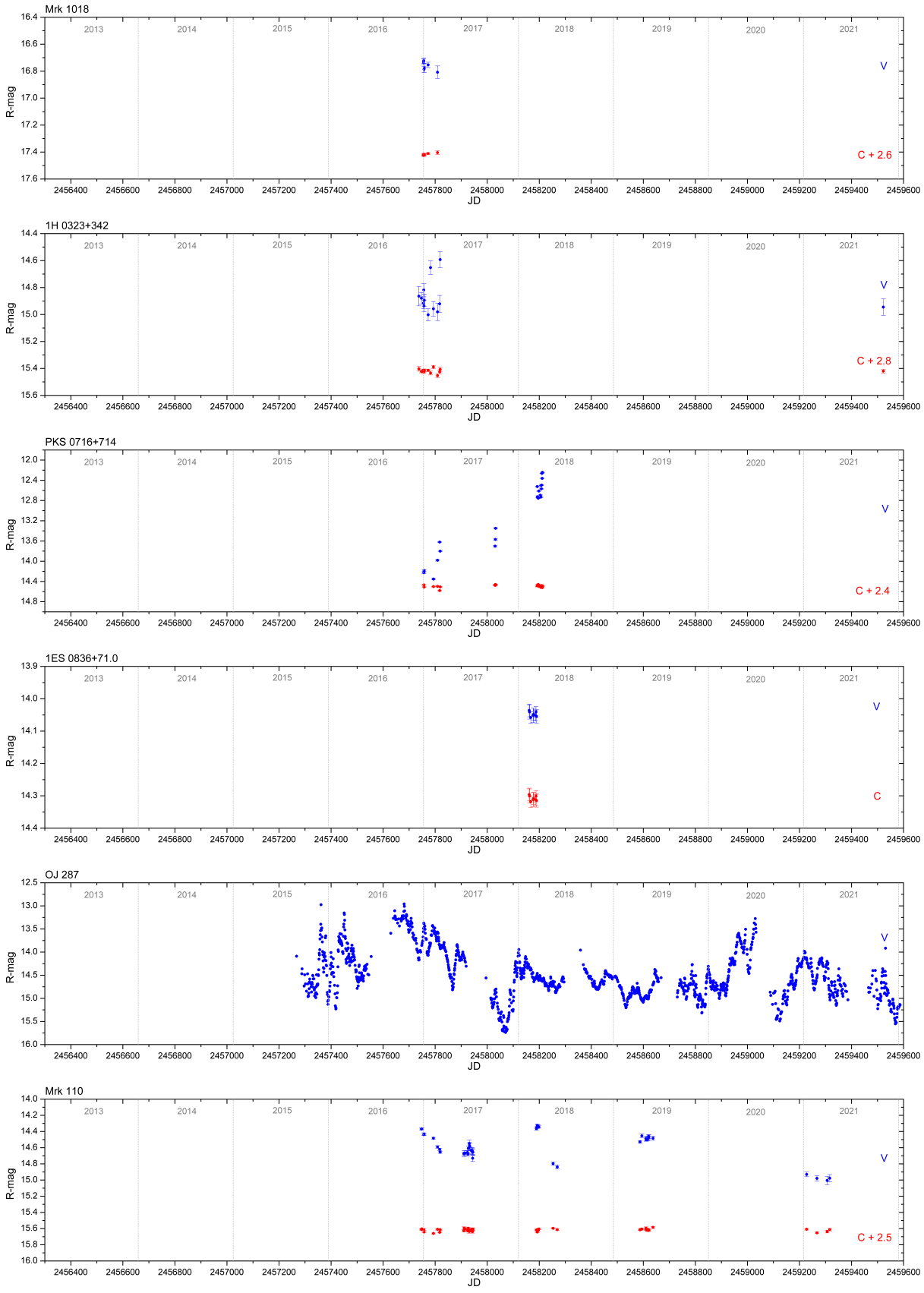

Figure 4.2: Photometric optical light curves of the first 6 targets of table 4.2 between 2013 and 2021.

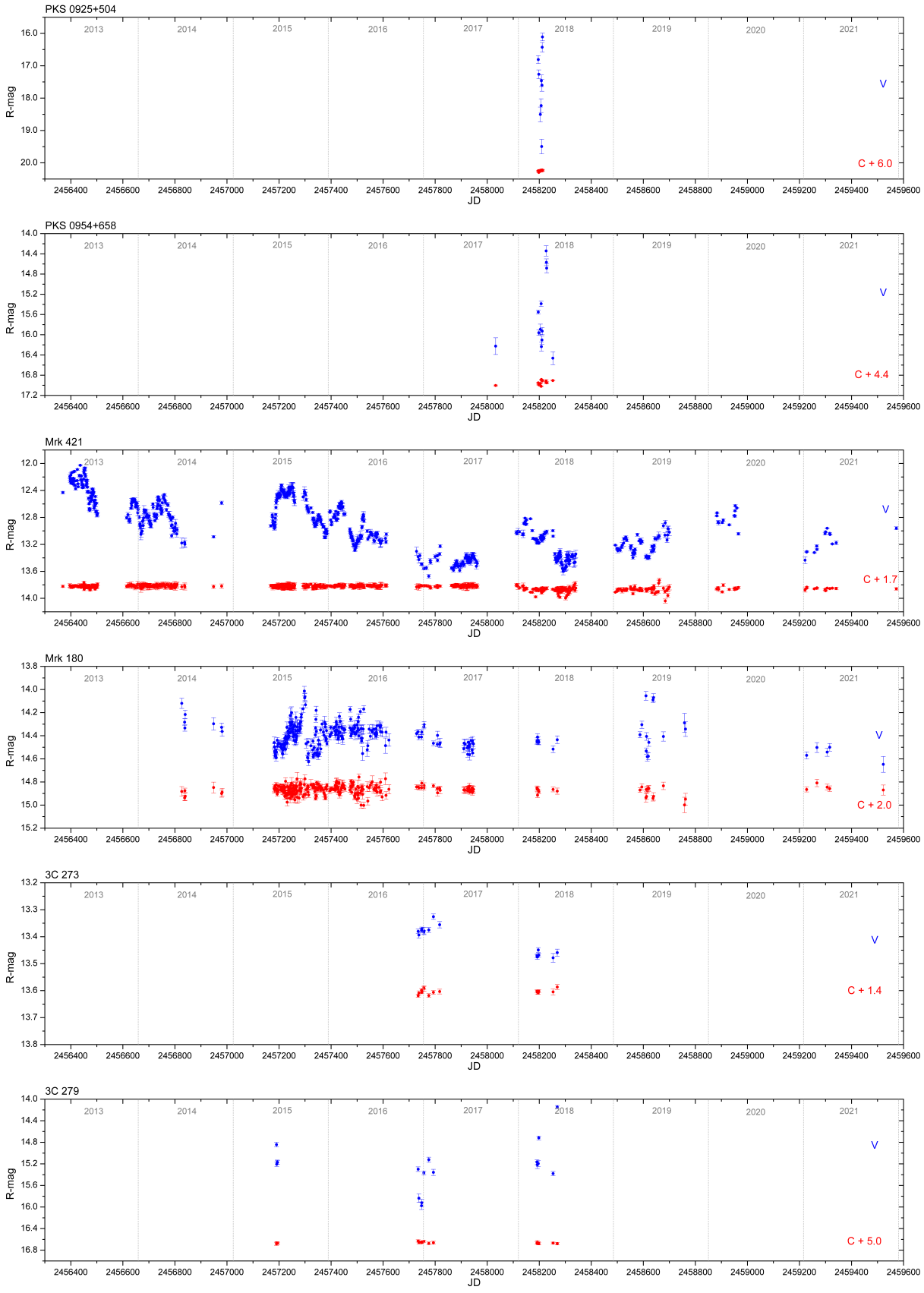

Figure 4.3: Photometric optical light curves of the next 6 targets of table 4.2 between 2013 and 2021.

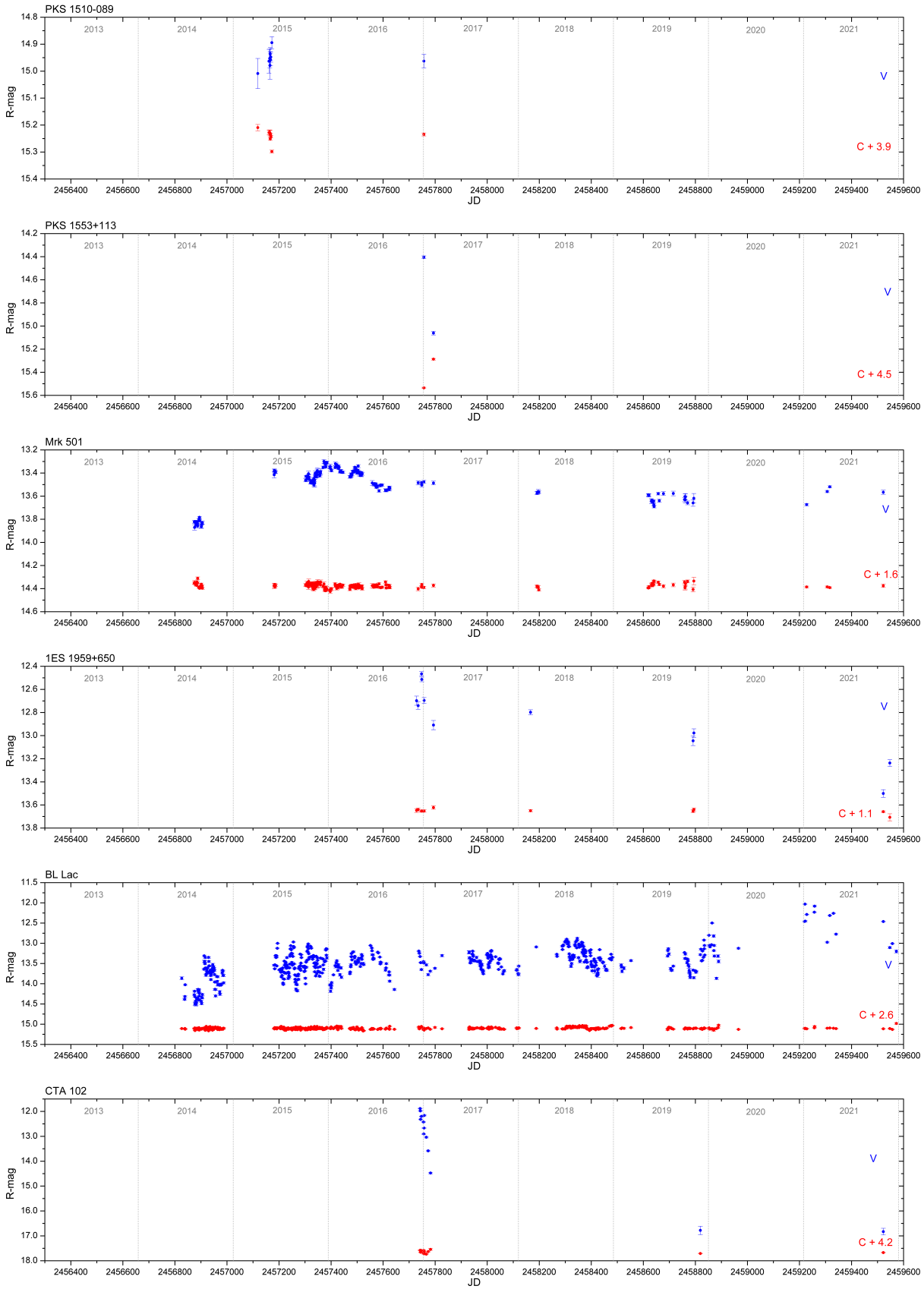

Figure 4.4: Photometric optical light curves of the next 6 targets of table 4.2 between 2013 and 2021.

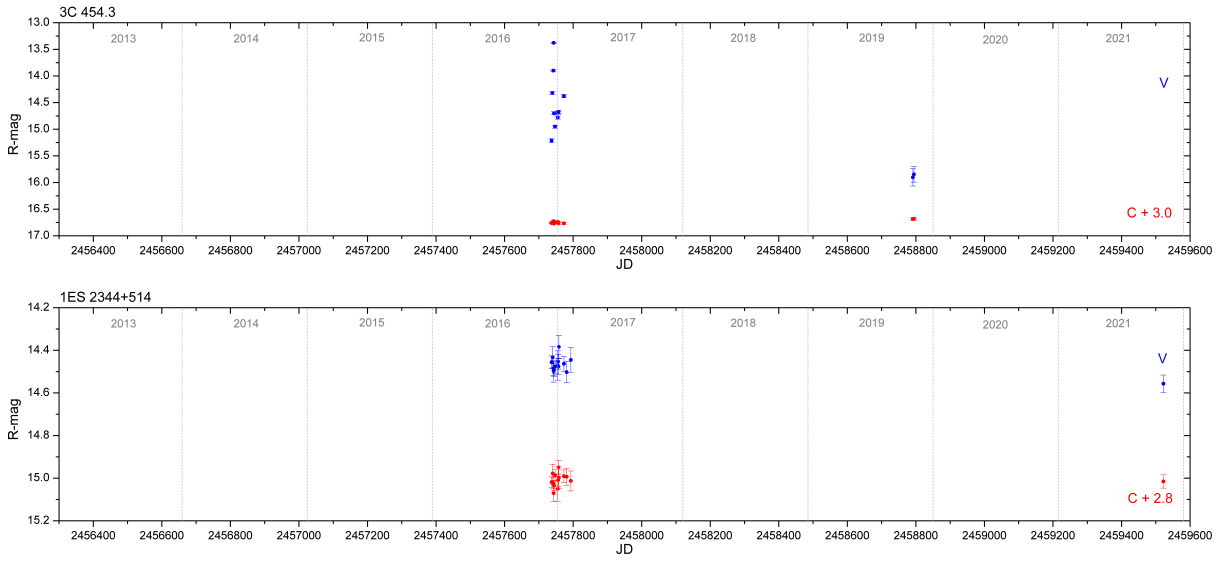

Figure 4.5: Photometric optical light curves of the last 2 targets of table 4.2 between 2013 and 2021.

The daily observation of each target is not always possible. The amount of data and the total duration of the observations differ for each target, as shown in table 4.1. Short-term variability and long-term variability can be seen in the light curves of many of the above AGNs. The variability in different timescales is going to be studied in the next sections.

4.2 Search for QPOs of intra-day timescales

In order to search for Quasi-Periodic oscillations with timescales of less than a day, high-cadence intra-day light curves are required. Thus IDVs were searched whenever it was possible.

The frequency limits for the search of periodic IDV are set based on the observations. Due to the fact that most observations have an exposure time of 180 sec, the upper limit of frequency is 200 cycles per day (cpd), which corresponds to a period of 7.2 minutes. The lower limit is set as 1/t (cpd), where t is the total duration of the observations (in days). The range of reliability of the detected frequencies is set from 2/t cpd, in order to detect at least two oscillations during the observations, to 100 cpd, which corresponds to 15 minutes, because we need at least 5 to 6 points to fit the trigonometric functions. A threshold in order to have at least 99% confidence in the detection of the QPOs was set, using a method based on gamma distribution and normal distribution. Also only the periods detected with at least two methods are considered significant.

The methods used in the search of QPOs are the ones discussed in paragraphs 3.1 and 3.2. The results from the search of QPOs of intra-day timescales can be found below. The tables with the intra-day QPOs of each target can be found in Appendix F.1.

We assume that QPOs of intra-day timescales originate from instabilities that occur in the inner region of the AD and the quasi-periodic signal is either observed directly from the AD or it propagates along the jet of the source. A scale factor for the radius of the region that the instabilities arise, hence referred as ***region of origin***, and for the parameters of the SMBH, such as the mass of the BH, the Eddington luminosity and the upper accretion rate can be calculated. The parameters are calculated for a non-rotating and maximally rotating BH, and for emission that either comes from the AD or from the jet, thus the Doppler factor is considered in the

calculations. The Doppler factor cannot be extracted directly from observations, but it has been estimated with different methods, thus many values for the Doppler factor have been proposed. Throughout this thesis the value of Doppler factor that was used is 6.87, which is based on a model suggested by Pei et al. (2022). Since we assumed that the periods detected with different methods are the same within a limit of 3-5 minutes, we use the mean value of these periods in order to calculate the parameters of the inner region of the AGN. The error in the calculation of the parameters is estimated based on the uncertainty of the detected timescales.

PKS 0716+714

In order to search for QPOs of intra-day timescales in PKS 0716+714, a total of 3 high-cadence light curves were studied. The detected timescales can be found in table 4.3.

Table 4.3: Period of detected IDVs in the optical light curves of PKS 0716+714.

JD	Duration (min)	Discrete Fourier Transform (P04)			Fast Fourier Transform (Python)			Lomb-Scargle Periodogram		
		Period (min)	Amplitude	S/N	Period (min)	Amplitude	S/N	Period (min)	Amplitude	S/N
2458030	359.61	52.13 ± 1.43	0.010 ± 0.001	9.2				52.30	0.3	3.3
2458031	471.34	231.96 ± 6.58	0.017 ± 0.002	4.8	227.31	0.011	7.8	227.41	0.4983	77.6
		66.56 ± 1.54	0.006 ± 0.002	5.9	138.37	0.006	2.3	138.45	0.1919	11.5
		50.51 ± 0.81	0.007 ± 0.002	5.0	63.65	0.008	4.4	64.43	0.1697	9.0
		32.55 ± 0.28	0.008 ± 0.002	2.5				50.86	0.1814	10.3
								32.53	0.2197	15.1
2458032	238.85	48.79 ± 5.96	0.007 ± 0.001	2.9	49.95	0.009	1.8			

The shortest detected IDV is 32 minutes. Timescales of 48-52 minutes were found in all the light curves, thus we assume that they relate to QPOs.

Assuming that the QPO originate from the inner region of the AD and that the timescale of 48-52 minutes, that was detected in all the light curves, relates to fluctuations that originate in the marginally stable orbit, we can calculate the lower bound of the mass of the BH using equations 1.14 and 1.15. The calculated masses can be seen in table 4.4.

Table 4.4: The calculated mass of the SMBH of PKS 0716+714.

$\mathbf{M_{BH}(10^7 M_\odot)}$	Non-rotating BH	Rotating BH
M_{stable}	0.51 ± 0.02	3.21 ± 0.10
$M_{stable}(\delta)$	3.47 ± 0.10	22.00 ± 0.66

Using direct measurements of stellar velocity dispersion, Woo & Urry (2002) calculated the mass of the SMBH of PKS 0716+714 to be $M = 2.80 \times 10^8 M_\odot$. This value is in line with the lower limit set by the detected timescales of QPOs.

From the mass of the BH we can calculate the minimum radius of the stable orbit (R_{ms}), using equations 1.13. The radii of the region of origin, in case of a non-rotating and a maximally rotating BH, can be seen in table 4.5.

Table 4.5: Radii of region of origin of IDV of PKS 0716+714.

$\mathbf{R(10^{10} m)}$	Non-rotating BH	Rotating BH
R_{stable}	4.47 ± 0.13	5.68 ± 0.17
$R_{stable}(\delta)$	30.70 ± 0.92	39.00 ± 1.17

From the mass of the SMBH we can also calculate the lower limit of Eddington luminosity using equation 1.1. The calculated luminosities can be seen in table 4.6.

Table 4.6: The calculated Eddington luminosity of PKS 0716+714.

$\mathbf{L_{Edd}(10^{12}L_{\odot})}$	**Non-rotating BH**	**Rotating BH**
$L_{Edd_{stable}}$	0.16 ± 0.01	1.03 ± 0.03
$L_{Edd_{stable}}(\delta)$	1.11 ± 0.03	7.05 ± 0.21

From Eddington luminosity we can calculate the Eddington accretion rate of the black hole, using equation 1.4. The calculated accretion rate can be found in table 4.7.

Table 4.7: The upper limit of accretion rate of PKS 0716+714.

$\mathbf{\dot{M}_{BH}(M_{\odot}/yr)}$	**Non-rotating BH**	**Rotating BH**
$\dot{M}_{stable}$	0.111 ± 0.003	0.706 ± 0.021
$\dot{M}_{stable}(\delta)$	0.763 ± 0.023	4.849 ± 0.145

OJ 287

A total of 19 high-cadence intra-day light curves of OJ287 were studied in order to detected QPOs. The timescales that were detected with at least 99% confidence can be found in table F.3 in Appendix F.1.

The shortest detected QPO is 19 minutes. The frequency that each timescale was detected can be seen in the frequency histogram of Fig. 4.6, which shows the detected QPOs grouped in 4-minute bins.

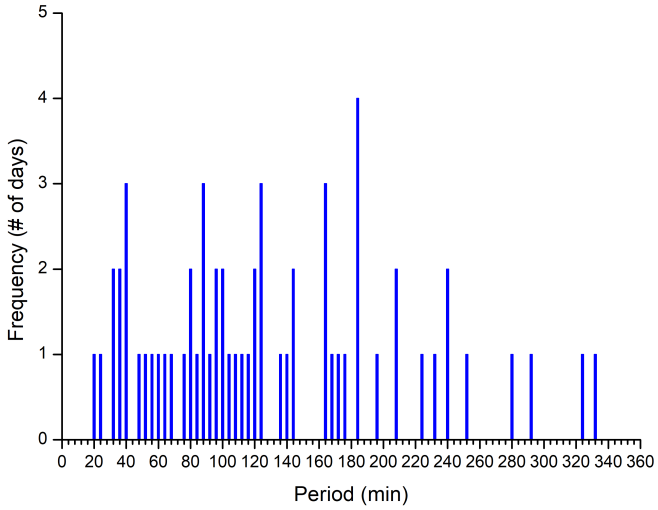

Figure 4.6: Frequency histogram of the detected period of IDVs of OJ287, in 4-minute bins. The data used to create this histogram can be found in table F.3 in Appendix F.1.

The timescales of the detected IDVs range between 19 and 330 minutes. The most frequently QPO with a timescale of 180-184 minutes was detected in 4 out of 19 intra-night light curves. In 3 out of 19 light curves, IDVs of 36-40, 84-88 and 120-124 minutes have been detected.

Assuming that the QPO originate from the inner region of the AD and that the timescale of 180-184 minutes, that was detected in most light-curves, relates to fluctuations that originate in the marginally stable orbit, we can calculate the lower bound of the mass of the BH using equations 1.14 and 1.15. The calculated masses can be seen in table 4.8.

Table 4.8: The calculated mass of the SMBH of OJ 287.

$\mathbf{M_{BH}(10^7 M_\odot)}$	**Non-rotating BH**	**Rotating BH**
M_{stable}	1.25 ± 0.02	7.93 ± 0.10
$M_{stable}(\delta)$	8.57 ± 0.10	54.50 ± 0.66

OJ 287 host a BH binary system. In order to accurately predict the timing of 10 flares in a period of about 80 years based on the binary black hole model, the mass of the central SMBH is predicted to be $M_{BH} = 18.35 \times 10^9 M_\odot$ (Laine et al., 2020). This value is in agreement with the calculated lower bound of mass based on the detected timescales of QPOs.

From the calculated mass, we can calculate the minimum radius of the stable orbit using equations 1.13. The radii of the region of origin, in case of a non-rotating and a maximally

rotating BH, can be seen in table 4.9.

Table 4.9: Radii of region of origin of IDV of OJ 287.

$\mathbf{R(10^{11}m)}$	**Non-rotating BH**	**Rotating BH**
R_{stable}	1.10 ± 0.01	1.40 ± 0.02
$R_{stable}(\delta)$	7.59 ± 0.09	9.65 ± 0.12

The lower limit of Eddington luminosity can be calculated from equation 1.1 using the calculated mass. The calculated luminosities can be seen in table 4.10.

Table 4.10: The calculated Eddington luminosity of OJ 287.

$\mathbf{L_{Edd}(10^{12}L_\odot)}$	**Non-rotating BH**	**Rotating BH**
$L_{Edd_{stable}}$	0.40 ± 0.01	2.54 ± 0.03
$L_{Edd_{stable}}(\delta)$	2.74 ± 0.03	17.40 ± 0.21

From Eddington luminosity we can calculate the upper accretion rate of the BH from equation 1.4. The calculated accretion rate can be found in table 4.11.

Table 4.11: The upper limit of accretion rate of OJ 287.

$\mathbf{\dot{M}_{BH}(M_\odot/yr)}$	**Non-rotating BH**	**Rotating BH**
$\dot{M}_{stable}$	0.275 ± 0.003	1.745 ± 0.021
$\dot{M}_{stable}(\delta)$	1.886 ± 0.023	11.988 ± 0.145

Mrk 421

A total of 16 high-cadence light curves were studied in order to find QPOs in Mrk 421. The intra-day timescales of the QPOs that were detected with at least 99% confidence in the optical light curves of Mrk 421 can be found in table F.4 in Appendix F.1.

The shortest detected IDV is 16 minutes. The frequency that each timescale was detected can be seen in the frequency histogram of Fig. 4.7, that shows the detected QPOs grouped in 4-minute bins.

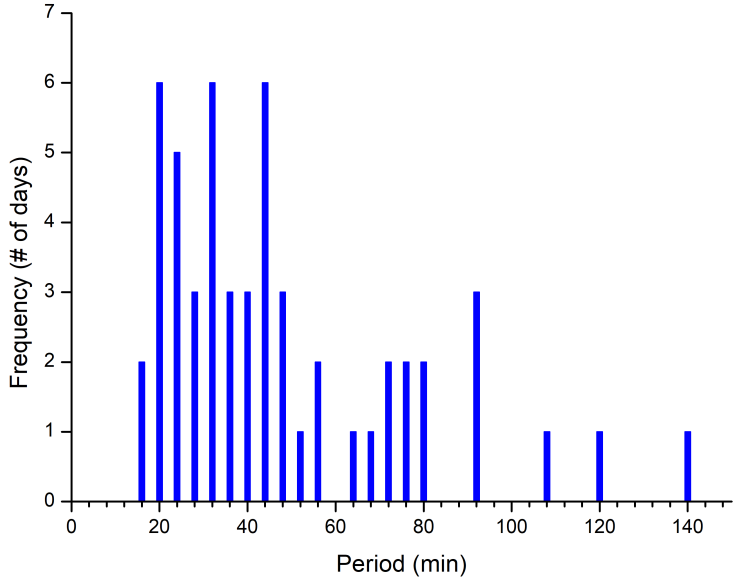

Figure 4.7: Frequency histogram of the detected period of IDVs of Mrk 421, in 4-minute bins. The data used to create this histogram can be found in table F.4 in Appendix F.1.

QPOs with timescales of 16-20, 28-32 and 40-44 minutes were detected in 6 out of 16 light curves. Also IDVs of 20-24 minutes have been detected in 5 out of the 16 light curves. Although the timescales of the detected QPOs range from 16 to 143 minutes, most of the IDVs are in the range of 16 to 48 minutes.

Assuming that the QPO originate from the inner region of the AD and that the timescale of 16-20 minutes, that is the shortest and most frequently detected timescales, relates to fluctuations that originate in the marginally stable orbit, we can calculate the lower bound of the mass of the BH using equations 1.14 and 1.15. The calculated masses can be seen in table 4.8.

Table 4.12: The calculated mass of the SMBH of Mrk 421.

$\mathbf{M_{BH}(10^7 M_\odot)}$	**Non-rotating BH**	**Rotating BH**
M_{stable}	0.23 ± 0.02	1.46 ± 0.12
$M_{stable}(\delta)$	1.58 ± 0.13	10.10 ± 0.84

Using direct measurements of stellar velocity dispersion, Woo & Urry (2002) calculated the mass of the SMBH of Mrk 421 to be $M = 1.95 \times 10^8 M_\odot$, which is in accordance with the limit set by the detected QPOs.

From the calculated mass, we can calculate the minimum radius of the stable orbit using

equations 1.13. The radii of the region of origin, in case of a non-rotating and a maximally rotating BH, can be seen in table 4.13.

Table 4.13: Radii of region of origin of IDV of Mrk 421.

$\mathbf{R(10^{10}m)}$	**Non-rotating BH**	**Rotating BH**
R_{stable}	2.04 ± 0.17	2.59 ± 0.22
$R_{stable}(\delta)$	14.00 ± 1.17	17.80 ± 1.48

The lower limit of Eddington luminosity can be calculated from equation 1.1 using the calculated mass. The calculated luminosities can be seen in table 4.14.

Table 4.14: The calculated Eddington luminosity of Mrk 421.

$\mathbf{L_{Edd}(10^{12}L_\odot)}$	**Non-rotating BH**	**Rotating BH**
$L_{Edd_{stable}}$	0.074 ± 0.006	0.47 ± 0.04
$L_{Edd_{stable}}(\delta)$	0.506 ± 0.004	3.22 ± 0.27

From Eddington luminosity we can calculate the upper accretion rate of the BH from equation 1.4. The calculated accretion rate can be found in table 4.15.

Table 4.15: The upper limit of accretion rate of Mrk 421.

$\mathbf{\dot{M}_{BH}(M_\odot/yr)}$	**Non-rotating BH**	**Rotating BH**
$\dot{M}_{stable}$	0.051 ± 0.004	0.322 ± 0.027
$\dot{M}_{stable}(\delta)$	0.348 ± 0.029	2.211 ± 0.184

BL Lac

In order to search for QPOs in BL Lac, a total of 27 intra-day high-cadence light curves were studied. The timescales of the QPOs detected with at least 99% confidence can be found in table F.5 in Appendix F.1. In some light curves, no QPOs with confidence greater than 99% were detected.

The timescale of the shortest detected IDV is 15 minutes. The frequency that each period was detected can be seen in the frequency histogram of Fig. 4.8, that shows the detected QPOs grouped in 4-minute bins.

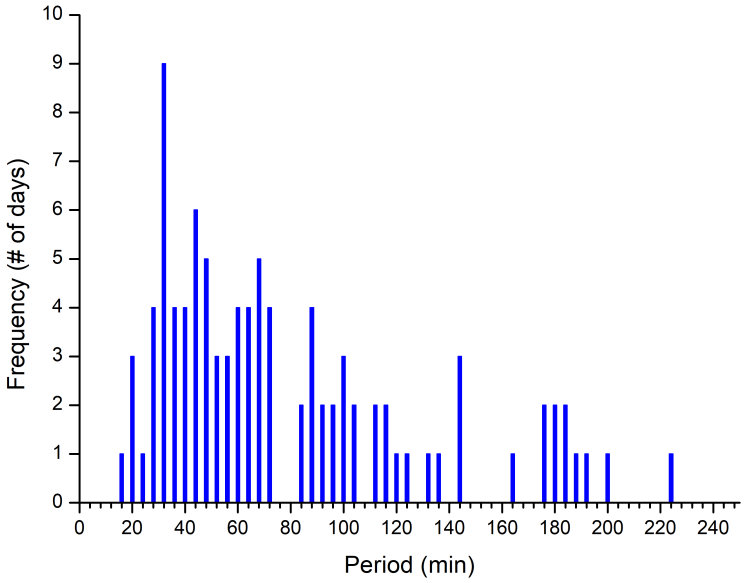

Figure 4.8: Frequency histogram of the detected period of IDVs of BL Lac, in 4-minute bins. The data used to create this histogram can be found in table F.5 in Appendix F.1.

IDVs of 28-32 minutes were detected in 9 out of 27 intra-night light curves. Also QPOs of 40-44 minutes have been detected in 6 out of the 27 light curves. The detected IDVs range from 16 to 236 minutes, but most of the timescales of the detected QPOs are between 24 and 72 minutes.

Assuming that the QPO originate from the inner region of the AD and that the timescale of 28-32 minutes, that was detected in most light-curves, relates to fluctuations that originate in the marginally stable orbit, we can calculate the lower bound of the mass of the BH using equations 1.14 and 1.15. The calculated masses can be seen in table 4.16.

Table 4.16: The calculated mass of the SMBH of BL Lac.

$\mathbf{M_{BH}(10^7 M_\odot)}$	**Non-rotating BH**	**Rotating BH**
M_{stable}	0.37 ± 0.02	2.35 ± 0.12
$M_{stable}(\delta)$	2.54 ± 0.13	16.20 ± 0.81

Titarchuk & Seifina (2017) estimated that the mass of the SMBH of BL Lac is $M = 3 \times 10^7 M_\odot$ based on the correlation of the photon index and the mass accretion rate. Another method that used direct measurements of stellar velocity dispersion, estimated that the mass of the BH is $M = 1.70 \times 10^8 M_\odot$ (Woo & Urry, 2002). The calculated values of the mass of the SMBH

are in accordance with the ones in the existing literature.

From the calculated mass, we can calculate the minimum radius of the stable orbit using equations 1.13. The radii of the region of origin, in case of a non-rotating and a maximally rotating BH, can be seen in table 4.17.

Table 4.17: Radii of region of origin of IDV of BL Lac.

$\mathbf{R(10^{10}m)}$	**Non-rotating BH**	**Rotating BH**
R_{stable}	3.28 ± 0.16	4.16 ± 0.21
$R_{stable}(\delta)$	22.50 ± 0.11	28.60 ± 1.43

The lower limit of Eddington luminosity can be calculated from equation 1.1 using the calculated mass. The calculated luminosities can be seen in table 4.18.

Table 4.18: The calculated Eddington luminosity of BL Lac.

$\mathbf{L_{Edd}(10^{12}L_{\odot})}$	**Non-rotating BH**	**Rotating BH**
$L_{Edd_{stable}}$	0.118 ± 0.006	0.75 ± 0.04
$L_{Edd_{stable}}(\delta)$	0.81 ± 0.04	5.17 ± 0.26

From Eddington luminosity we can calculate the upper accretion rate of the black hole, using equation 1.4. The calculated accretion rate can be found in table 4.19.

Table 4.19: The upper limit of accretion rate of BL Lac.

$\mathbf{\dot{M}_{BH}(M_{\odot}/yr)}$	**Non-rotating BH**	**Rotating BH**
$\dot{M}_{stable}$	0.081 ± 0.004	0.517 ± 0.026
$\dot{M}_{stable}(\delta)$	0.599 ± 0.028	3.554 ± 0.178

The timescales of the detected QPOs in the optical light curves of all the targets can be seen in the frequency histogram in Fig. 4.9, that shows the QPOs grouped in 3-minute bins.

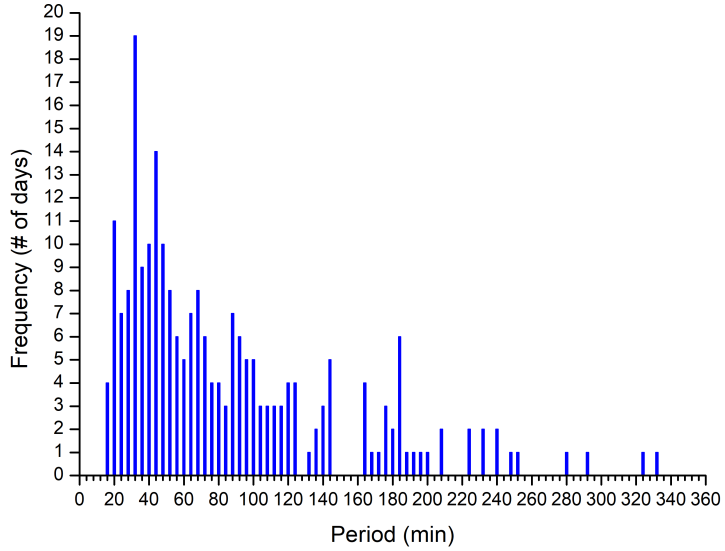

Figure 4.9: Frequency histogram of the detected period of IDVs of all the targets, in 3-minute bins.

The timescales of the detected IDVs range from 15 to 330 minutes, but most of the detected IDVs have periods in the range of 15 to 72 minutes. This shows very fast rotation of matter in the AD. QPOs of greater timescales have been detected in lesser days, but that is due to the duration of the observations and the reliability limit we set in the search of the periods.

4.3 Search for QPOs of short-term timescales

To search for QPOs with timescales of some days to several months, a large amount of data for several, preferably continuous, nights must be acquired. The data used for the search of STVs were grouped in 1-day bins using an algorithm developed in *Python* environment, the algorithm can be found in Appendix C.

The frequency limits for the search of the period of STVs are set based on the observations. The upper limit of frequency is 0.3 cycles per day (cpd), which corresponds to a period of 3 days. The lower limit is set as 1/t (cpd), where t is the total duration of the observations (in days). The range of reliability of the detected frequencies is set from 2/t cpd, in order to detect at least two oscillations during the observations, to 0.15 cpd, which corresponds to 6 days, because we need at least 5 to 6 points to fit the trigonometric functions. To ensure that the detected timescales are significant, a threshold of 99% confidence was set. Also only the periods detected with at least two methods are considered significant. We set a limit of 3-5 days that we assume the detected periods are the same.

Since our data include several time-gaps, the reliability of the DFT method is limited with respect to the LSP method, even though periods were detected with 99% confidence. The timescales of QPOs that were detected with all methods are presented below. The LSP method is considered more reliable. The tables with the short-term QPOs of each target can also be found in Appendix F.2. The same applies for all wavelengths under study.

OJ 287

In order to search for short-term QPO in OJ 287, we studied a total of 7 short-term light curves. The short-term timescales of QPOs in OJ 287 can be found in table F.6 in Appendix F.2.

The shortest STV detected has a period of 21 days. The frequency that each period was detected can be seen in the frequency histogram of Fig. 4.10, that shows the detected QPOs grouped in 3-day bins.

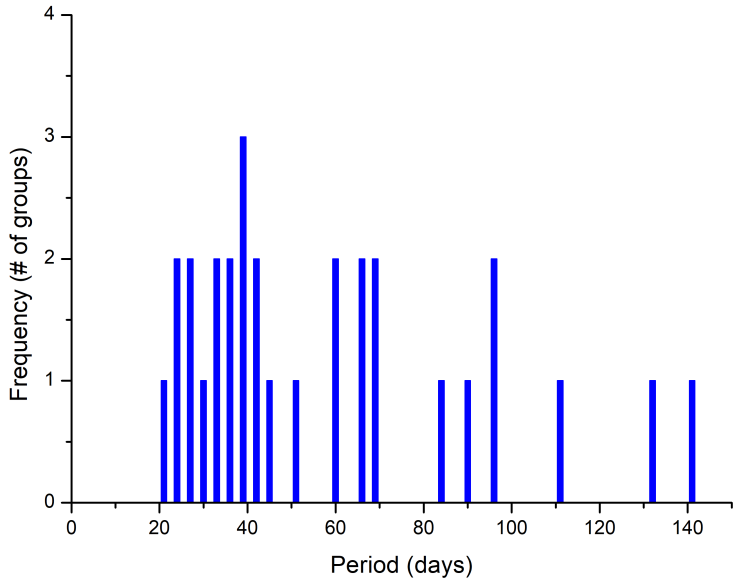

Figure 4.10: Frequency histogram of the detected period of STVs of OJ 287, in 3-day bins. The data used to create this histogram can be found in table F.6 in Appendix F.2.

QPOs with timescales in the range of 36-39 days were detected in 3 out of 7 light curves. The detected STVs range from 21 to 143 days, but most of the QPOs have timescales in the range of 21 to 69 days.

Mrk 421

A total of 5 light curves were studied in order to search for short-term quasi-periodic signals in Mrk 421 in optical wavelengths. The detected timescales of QPOs can be found in table 4.20.

Table 4.20: Period of the detected STVs in the optical light curves of Mrk 421.

JD	Duration	Discrete Fourier Transform (P04)			Fast Fourier Transform (Python)			Lomb-Scargle Periodogram		
	(days)	Period (days)	Amplitude	S/N	Period (days)	Amplitude	S/N	Period (days)	Amplitude	S/N
2456369-2456502	133	60.04 ± 2.75	0.12 ± 0.02	5.405	15.88	0.063	3.4	63.27	0.44	3.9
		28.20 ± 0.82	0.09 ± 0.02	4.010				26.41	0.44	3.8
		14.00 ± 0.23	0.08 ± 0.02	3.487						
2456614-2456838	224	42.25 ± 0.77	0.10 ± 0.02	4.810	45.86	0.107	11.7	42.91	0.44	4.0
		26.03 ± 0.41	0.07 ± 0.02	3.415	26.75	0.058	3.4			
2457168-2457612	444	109.94 ± 1.00	0.21 ± 0.01	13.506	70.50	0.072	25.4	106.87	0.56	6.2
		73.52 ± 0.86	0.11 ± 0.01	7.043	50.36	0.064	20.0			
		53.56 ± 0.35	0.14 ± 0.01	9.203						
2457728-2457962	234	112.09 ± 1.93	0.09 ± 0.01	12.32	32.57	0.075	12.0	110.50	0.74	10.9
		31.01 ± 0.44	0.03 ± 0.01	4.188				30.74	0.33	2.1
2458112-2458340	228	76.92 ± 9.84	0.04 ± 0.03	1.322	78.00	0.162	55.2	34.97	0.41	3.4
		22.87 ± 0.43	0.08 ± 0.03	2.675	34.67	0.060	7.7	22.32	0.30	1.8
					22.29	0.050	5.2			

The shortest detected STV has a period of 14 days. In 2 out of 5 light curves, a QPO of 24-27 days was detected.

Mrk 180

One light curve of Mrk 180 was studied in order to search for QPOs of short-term timescales. The detected timescales can be found in table 4.21.

Table 4.21: Period of the detected STVs in the optical light curves of Mrk 180.

JD	Duration	Discrete Fourier Transform (P04)			Fast Fourier Transform (Python)			Lomb-Scargle Periodogram		
	(days)	Period (days)	Amplitude	S/N	Period (days)	Amplitude	S/N	Period (days)	Amplitude	S/N
2457181-2457643	462	117.74 ± 2.11	0.10 ± 0.01	6.4	147.00	0.034	4.9	147.16	0.45	15.0
		62.23 ± 0.40	0.15 ± 0.01	9.3	61.25	0.033	4.8	120.80	0.43	13.4
		44.32 ± 0.30	0.10 ± 0.01	6.3	45.94	0.044	8.5			
		33.06 ± 0.10	0.17 ± 0.01	10.1	33.41	0.029	3.7			
		27.38 ± 0.15	0.08 ± 0.01	4.8	27.22	0.032	4.4			
		17.00 ± 0.06	0.08 ± 0.01	4.8	17.93	0.026	3.0			

The shortest STV has a period of 17 days. A QPO with timescale of 33 days was also detected, which can possibly be a harmonic of the period of 17 days. The detected STVs range from 17 to 147 days.

Mrk 501

In order to search for short-term QPOs in Mrk 501, one light curves was studied. The detected timescales can be found in table 4.22.

Table 4.22: Period of the detected STVs in the optical light curves of Mrk 501.

JD	Duration	Discrete Fourier Transform (P04)			Fast Fourier Transform (Python)			Lomb-Scargle Periodogram		
	(days)	Period (days)	Amplitude	S/N	Period (days)	Amplitude	S/N	Period (days)	Amplitude	S/N
2457302-2457625	323	142.36 ± 3.45	0.062 ± 0.01	8.85				137.79	0.63	8.1
		36.42 ± 0.70	0.02 ± 0.01	2.859				36.03	0.27	1.5

The shortest STV is 36 days, while the longest is 137-142 days.

BL Lac

A total of 5 light curves of BL Lac were studied in order to search for QPOs of hort-term timescales. The detected timescales can be found in table F.10 in Appendix F.2.

The shortest detected STV is 11 days. The frequency that each period was detected can be seen in the histogram of Fig. 4.11, which shows the detected QPOs grouped in 3-day bins.

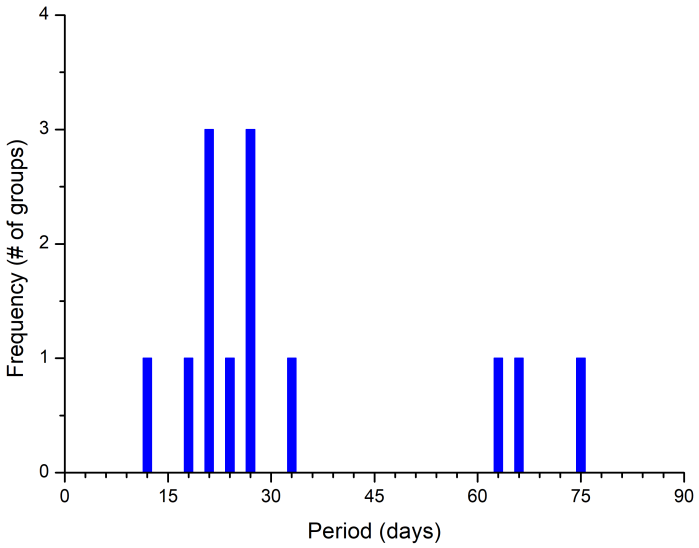

Figure 4.11: Frequency histogram of the detected period of STVs of BL Lac, in 3-day bins.

In 3 out of 5 light curves, QPOs with timescales of 18-21 and 24-28 days were detected. The STVs have periods between 11 and 74 days, but most of the QPOs are in the range of 18 to 28 days.

The short-term timescales of QPOs that were detected in the light curves of all the targets can be seen in the frequency histogram in Fig. 4.12.

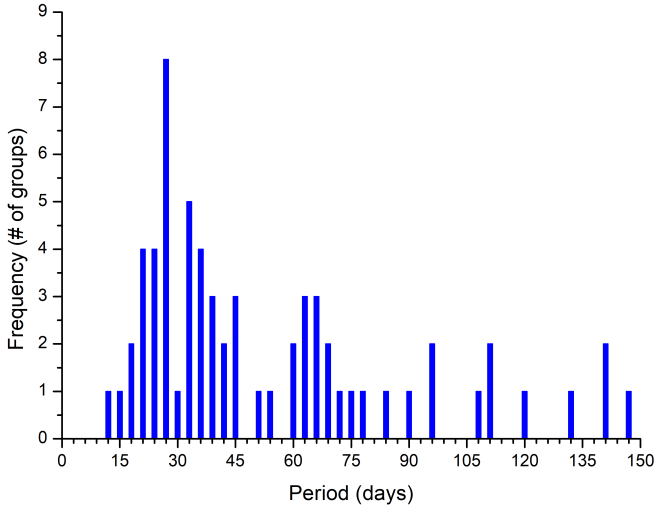

Figure 4.12: Frequency histogram of the detected period of STVs of all the targets, in 3-day bins.

The detected QPOs have timescales between 12 and 147 days, but most of the detected

STVs are in the range of 18 to 45 minutes. QPOs of greater timescales have been detected in less light curves, but that is due to the duration of the observations and the reliability limit we set in the search of the QPOs.

4.4 Search for Long-Term Variability (LTV)

In order to search for Long-Term Variability non of the methods mentioned in paragraphs 3.1 and 3.2 were impemented. We searched for fluctuations and trends in the light curves of the targets (Fig. 4.2, 4.3, 4.4, and 4.5). Not all targets have enough data to search for LTV, thus only some targets were studied.

OJ 287

The light curve of OJ 287 shows great variability from mid-2015 to 2021, when it was observed. The target was in a high-state from late 2015 to early 2017 and had a flare event in mid 2020. Many fluctuations of smaller magnitude change can be seen throughout the duration of the observations.

Mrk 421

Mrk 421 is highly variable from 2013 to 2021. In 2013, the target was is high-state, with a downward trend from mid 2013 to mid 2014, when it reached a medium state. In 2015, Mrk 421 was also in a high state with a downward trend from mid-2015 to mid-2017. An upward trend can be seen in the light curve from mid-2018 to mid-2020. Multiple flare events were observed throughout the duration of the observations.

Mrk 180

The light curve of Mrk 180 shows no trend in the period that it was observed. A flare event can be seen starting in mid-2015, reaching its peak in October 2015 and then the target returns to its mean magnitude by the end of 2015.

BL Lac

BL Lac shows high variability from 2014 to early 2021. From 2014 to 2020, the light curve of BL Lac is shows a small upward trend. In 2021, the target was in a high state and the brightness was increased up to 1 mag from its mean value.

Chapter 5

Search for QPOs in radio wavelengths

The radio radio curves that were studied in the frame of this thesis were obtained from Metsähovi Radio Observatory (MRO) (37 GHz), from Owens Valley Radio Observatory (OVRO) (15 GHz) and from Xinjiang Astronomical Observatory by the Nanshan Radio Telescope (NSRT) (4.8 GHz).

5.1 Metsähovi Radio Observatory

Metsähovi Radio Observatory (MRO) is a radio observatory in Finland associated with the Aalto University. It hosts a Cassegrain-type antenna with a diameter of 14 m, which is protected from the weather and the Sun's heat radiation by a radome. The receiver is a Dicke type radiometer and a Peltier element is used to stabilize the temperature of the receiver (Kallunki et al., 2012).

Figure 5.1: Metsähovi Radio Observatory and the 14 m radio telescope.

Radio observations are done daily at millimeter waves and microwaves from 2 to 150 GHz and are used for international very long baseline interferometry (VLBI) campaigns and in the study of active galaxies, the Sun, and the rotation of the Earth.

One of the main research activities is the observation of active galaxies in 22 and 37 GHz, in order to study the long-term variability of the sources, and the high-frequency radio behaviour of various source populations.

5.2 Owens Valley Radio Observatory

Owens Valley Radio Observatory (OVRO) is owned and operated by the California Institute of Technology (Caltech). It hosts a 40 m f/0.4 parabolic reflector on an altitude-azimuth mount. It uses off-axis Dicke-switched dual-beam optics to achieve high efficiency. The telescope and the receiver produce a pair of Gaussian beams separated in azimuth by 12.95′ (Richards et al., 2011).

Figure 5.2: Owens Valley Radio Observatory's 40 m radio telescope.

Since 2008, regular observations of blazars have been carried out as a part of blazars monitoring program. The targets of the program include all of the "Candidate Gamma-Ray Blazar Sample" (CGRaBS) north of declination -20 degrees and all of the sources from the first and second *Fermi* detected AGN (1LAC and 2LAC).

5.3 Xinjiang Astronomical Observatory

Xinjiang Astronomical Observatory (XAO) of the Chinese Academy of Sciences (CAS) was founded in 1957. Its current research covers areas such as star formation and evolution, galaxies and cosmology, pulsars, high-energy astrophysics, and so on. The Nanshan Radio Telescope (NSRT) is a 25 m radio telescope, with a sub-reflector made of carbon fiber materials. Also the telescope is equipped with four cryogenic receivers.

Figure 5.3: Nanshan Radio Telescope.

It is the second radio telescope that was used for VLBI observations. Other areas of research are pulsars, star formation and evolution, and active galactic nuclei. NSRT has also an important role in China's Lunar Exploration Program.

5.4 Data acquisition

5.4.1 Observations at 37 GHz

In the frame of this thesis, data from Metsähovi Radio Observatory at 37 GHz were acquired for 4 targets of BOSS Project. The targets are: ***OJ 287, Mrk 421, Mrk 501*** and ***BL Lac***. The radio curves at 37 GHz are plotted below, in Fig. 5.4.

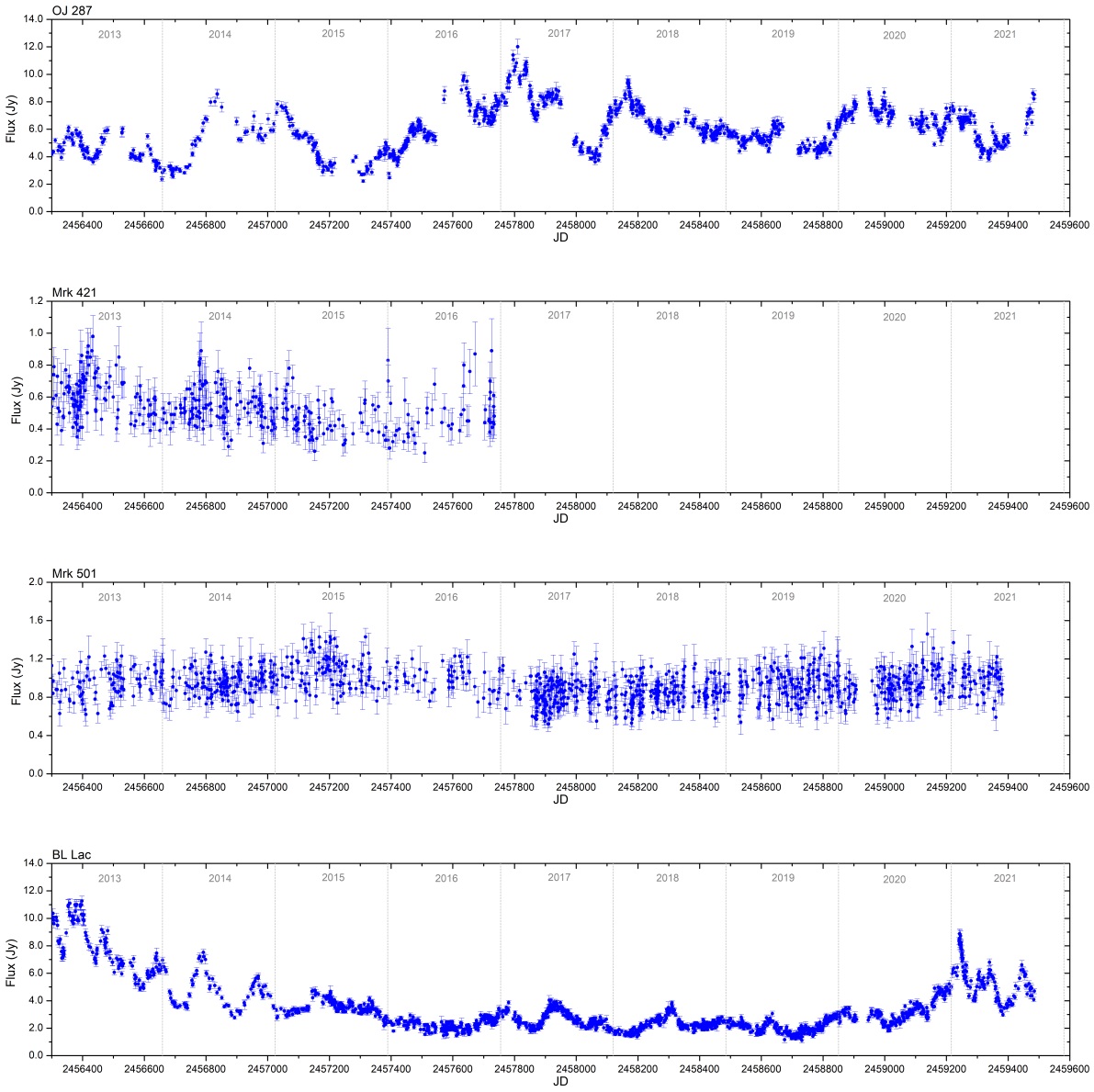

Figure 5.4: The radio curves of the AGNs at 37 GHz.

5.4.2 Observations at 15 GHz

Data from Owens Valley Radio Observatory at 15 GHz were acquired for 5 targets of BOSS Project. The targets are: ***OJ 287, Mrk 421, Mrk180, Mrk 501*** and ***BL Lac***. The radio curves at 15 GHz are plotted below, in Fig. 5.5.

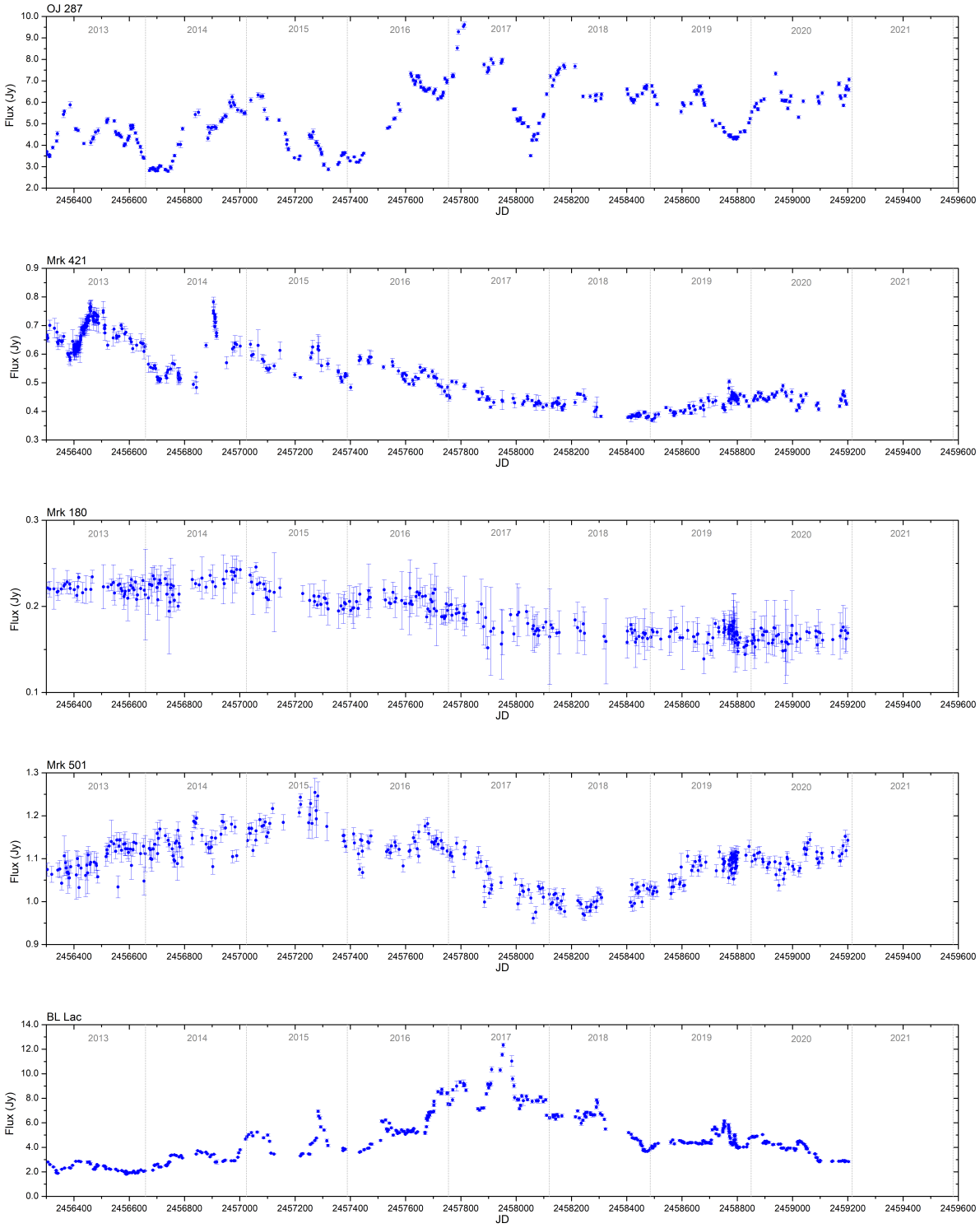

Figure 5.5: The radio curves of the AGNs at 15 GHz.

5.4.3 Observations at 4.8 GHz

Data from Nanshan Radio Telescope at 4.8 GHz were acquired for 4 targets of BOSS Project. The targets are: ***OJ 287, Mrk 421, Mrk 501*** and ***BL Lac***. The radio curves at 4.8 GHz are plotted below, in Fig. 5.6.

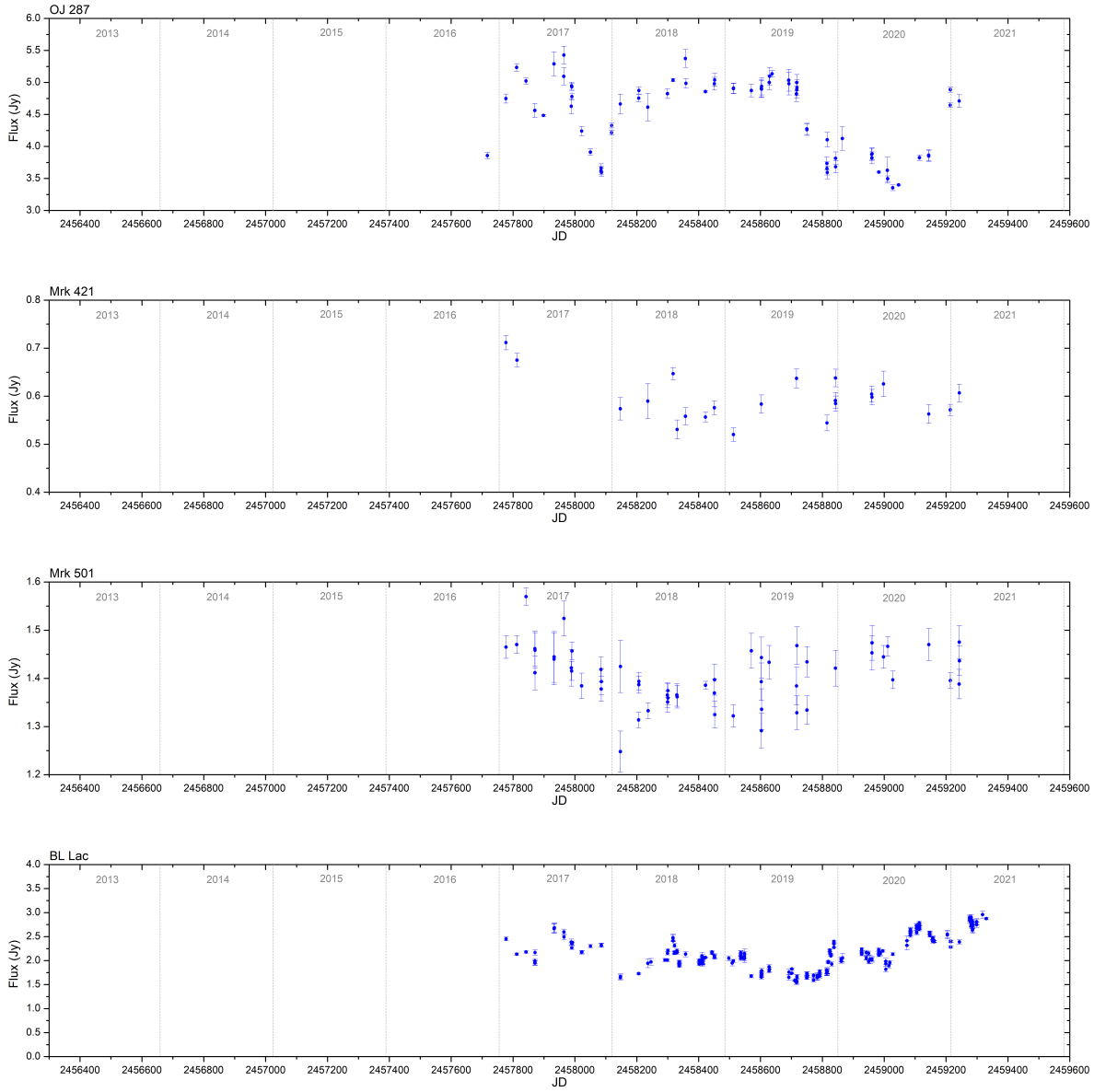

Figure 5.6: The radio curves of the AGNs at 4.8 GHz.

5.5 Data Analysis

The acquired data in radio wavelengths are grouped in one-day bins, thus we can only search for Short-term variability and Long-term variability. The methods implemented for the search of STV are the ones described in paragraphs 3.1, 3.2.

5.6 Search QPOs of short-term timescales

The frequency limits for the search of the period of STVs are set based on the observations. The upper limit of frequency is 0.3 cycles per day (cpd), which corresponds to a period of 3 days. The lower limit is set as 1/t (cpd), where t is the total duration of the observations (in days). The range of reliability of the detected frequencies is set from 2/t cpd, in order to detect at least two oscillations during the observations, to 0.15 cpd, which corresponds to 6 days, because we need at least 5 to 6 points to fit the trigonometric functions. A threshold was set in order to have at least 99% confidence in the detected periods.

5.6.1 Short-term QPOs at 37 GHz

The results from the search of QPOs of short-term timescales in the radio curves at 37 GHz can be found below. The tables with the short-term QPOs of each target can be found in Appendix G.1.

OJ 287

The short-term timescales of the detected QPOs in the radio curve of OJ 287 can be found in table 5.1.

Table 5.1: Period of the detected STVs in the radio curves of OJ 287 at 37 GHz.

JD	Duration	Discrete Fourier Transform (P04)			Fast Fourier Transform (Python)			Lomb-Scargle Periodogram		
	(days)	Period (days)	Amplitude	S/N	Period (days)	Amplitude	S/N	Period (days)	Amplitude	S/N
2456294-2459484	3190	313.07 ± 2.48	0.30 ± 0.04	5.4	310.09	0.33	25.2			
		225.62 ± 1.12	0.34 ± 0.04	6.2	227.40	0.34	27.4			
		181.88 ± 0.59	0.43 ± 0.04	7.7	179.53	0.46	49.6			
		128.69 ± 0.74	0.17 ± 0.04	3.1	126.33	0.13	3.8			
		110.62 ± 0.23	0.40 ± 0.04	7.3	110.03	0.32	23.9			
		91.31 ± 0.24	0.26 ± 0.04	4.7	92.19	0.45	47.7			

The shortest detected STV is 91-92 days (3 months). Also a QPO of 179-181 days was detected, which may possibly be a harmonic of the STV of 91-92 days.

Mrk 421

The short-term timescales of the detected QPOs in the radio curves of Mrk 421 can be found in table 5.2.

Table 5.2: Period of the detected STVs in the radio curves of Mrk 421 at 37 GHz.

JD	Duration	Discrete Fourier Transform (P04)			Fast Fourier Transform (Python)			Lomb-Scargle Periodogram		
	(days)	Period (days)	Amplitude	S/N	Period (days)	Amplitude	S/N	Period (days)	Amplitude	S/N
2456297-2457734	1437	124.54 ± 1.23	0.04 ± 0.01	3.8	125.67	0.045	5.3			
		54.35 ± 0.25	0.04 ± 0.01	3.5	56.55	0.034	3.0			

The detected QPOs have timescales of 54-56 and 124-125 days.

Mrk 501

The short-term timescales of the detected QPOs in the radio curves of Mrk 501 can be found in table 5.3.

Table 5.3: Period of the detected STVs in the radio curves of Mrk 501 at 37 GHz.

JD	Duration	Discrete Fourier Transform (P04)			Fast Fourier Transform (Python)			Lomb-Scargle Periodogram		
	(days)	Period (days)	Amplitude	S/N	Period (days)	Amplitude	S/N	Period (days)	Amplitude	S/N
2456297-2459381	3084	27.00 ± 0.03	0.03 ± 0.01	3.9	25.30	0.03	3.6			

The only detected QPOs has a timescale of 25-27 days.

BL Lac

The short-term timescales of the detected QPOs in the radio curves of BL Lac can be found in table 5.4.

Table 5.4: Period of the detected STVs in the radio curves of BL Lac at 37 GHz.

JD	Duration	Discrete Fourier Transform (P04)			Fast Fourier Transform (Python)			Lomb-Scargle Periodogram		
	(days)	Period (days)	Amplitude	S/N	Period (days)	Amplitude	S/N	Period (days)	Amplitude	S/N
2456294-2459485	3191	351.00 ± 2.08	0.51 ± 0.05	8.7	348.64	0.58	221.5			
		272.94 ± 1.80	0.35 ± 0.05	6.1	271.17	0.20	27.0			
		190.04 ± 0.85	0.36 ± 0.05	6.3	187.73	0.10	6.1			
		163.29 ± 0.65	0.35 ± 0.05	6.1	162.70	0.21	28.5			
		86.85 ± 0.20	0.32 ± 0.05	5.5	87.16	0.10	6.1			

The shortest detected STV is 86-87 days with a possible harmonic of 162-163 days detected.

The short-term timescales of the detected QPOs at 37 GHz of all the targets can be seen in Fig. 5.9.

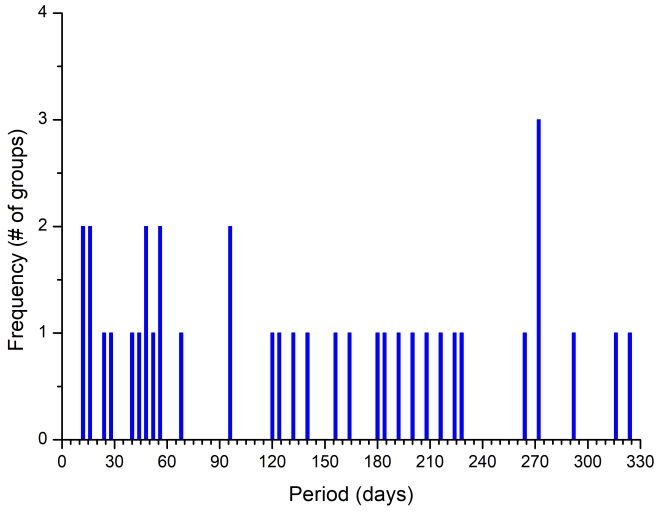

Figure 5.7: Frequency histogram of the detected period of STVs at 37 GHz, in 4-day bins.

The detected STVs have periods between 8 and 324 days, but most of the detected QPOs have timescales from 8 to 96 days, and a peak at 268 to 272 days. QPOs of greater timescales have been detected but due to the duration of the observations and the reliability limit we set in the search of the frequencies, those are less frequently detected.

5.6.2 Short-term QPOs at 15 GHz

The results from the search of QPOs of short-term timescales in the radio curves at 15 GHz can be found below. The tables with the detected periods can be found in Appendix G.2.

OJ 287

The short-term timescales of the detected QPOs in the radio curve of OJ 287 can be found in table 5.5.

Table 5.5: Period of the detected STVs in the radio curves of OJ 287 at 15 GHz.

JD	Duration	Discrete Fourier Transform (P04)			Fast Fourier Transform (Python)			Lomb-Scargle Periodogram		
	(days)	Period (days)	Amplitude	S/N	Period (days)	Amplitude	S/N	Period (days)	Amplitude	S/N
2454473-2459204	4731	645.35 ± 3.56	0.76 ± 0.06	11.3	650.00	0.58	43.4			
		323.37 ± 1.91	0.36 ± 0.06	5.3	325.00	0.94	115.6			
		128.46 ± 0.37	0.29 ± 0.06	4.3	130.00	0.86	95.0			
		108.44 ± 0.27	0.28 ± 0.06	4.2	108.33	0.45	26.0			

The shortest detected STV is 108 days (3.6 months).

Mrk 421

The short-term timescales of the detected QPOs in the radio curves of Mrk 421 can be found in table 5.6.

Table 5.6: Period of the detected STVs in the radio curves of Mrk 421 at 15 GHz.

JD	Duration	Discrete Fourier Transform (P04)			Fast Fourier Transform (Python)			Lomb-Scargle Periodogram		
	(days)	Period (days)	Amplitude	S/N	Period (days)	Amplitude	S/N	Period (days)	Amplitude	S/N
2454473-2459195	4722	438.37 ± 4.04	0.02 ± 0.01	4.1	363.43	0.042	95.3	443.18	0.27	6.1
		234.67 ± 0.68	0.04 ± 0.01	7.0	231.27	0.030	49.7	362.64	0.27	6.0
		178.72 ± 0.39	0.04 ± 0.01	7.1	159.00	0.012	7.9	177.83	0.27	6.1
		146.78 ± 0.42	0.02 ± 0.01	4.5	149.65	0.011	6.1	161.88	0.21	3.8
		77.26 ± 0.12	0.02 ± 0.01	4.2	77.09	0.010	5.0	148.75	0.23	4.7
		70.83 ± 0.11	0.02 ± 0.01	3.8	72.69	0.025	33.2			

The shortest detected timescale of QPO is 70-72 days (2.3 months), with a possible harmonic of 146-149 days.

Mrk 180

The short-term timescales of the detected QPOs in the radio curves of Mrk 180 can be found in table 5.7.

Table 5.7: Period of the detected STVs in the radio curves of Mrk 180 at 15 GHz.

JD	Duration	Discrete Fourier Transform (P04)			Fast Fourier Transform (Python)			Lomb-Scargle Periodogram		
	(days)	Period (days)	Amplitude	S/N	Period (days)	Amplitude	S/N	Period (days)	Amplitude	S/N
2454474-2459199	4725	887.32 ± 7.51	0.014 ± 0.001	9.9	165.27	0.011	73.5	888.19	0.35	29.4
		402.98 ± 2.64	0.008 ± 0.001	5.8	121.20	0.005	18.5	403.95	0.27	17.6
		338.10 ± 2.55	0.006 ± 0.001	4.2	106.94	0.004	11.5	335.24	0.20	9.5
		165.93 ± 0.76	0.005 ± 0.001	3.4				166.03	0.20	9.2
		108.81 ± 0.33	0.005 ± 0.001	3.4				119.70	0.14	5.0
								108.95	0.15	5.7

The shortest detected STV has a period of 84-86 days (2.8-2.9 months). QPOs with timescales of 104-112 days (3.5-3.7 months) and 183-189 days (6.1-6.3 months) were detected with all the methods.

Mrk 501

The short-term timescales of the detected QPOs in the radio curves of Mrk 501 can be found in table 5.8.

Table 5.8: Period of the detected STVs in the radio curves of Mrk 501 at 15 GHz.

JD	Duration	Discrete Fourier Transform (P04)			Fast Fourier Transform (Python)			Lomb-Scargle Periodogram		
	(days)	Period (days)	Amplitude	S/N	Period (days)	Amplitude	S/N	Period (days)	Amplitude	S/N
2454853-2459199	4346	370.02 ± 2.12	0.02 ± 0.01	6.5	376.20	0.038	106.7			
		186.57 ± 0.88	0.01 ± 0.01	4.0	188.10	0.009	5.9			
		159.23 ± 0.62	0.01 ± 0.01	4.2	156.75	0.007	3.5			
		143.94 ± 0.54	0.01 ± 0.01	3.9	144.69	0.017	20.5			
		135.21 ± 0.37	0.02 ± 0.01	5.0	134.36	0.015	15.5			
		54.67 ± 0.08	0.01 ± 0.01	3.6	53.74	0.007	3.5			

The shortest STV is 54-56 days (1.8-1.9 months). QPOs with timescales of 224-229 days (7.5-7.6 months) and 314-319 days (10.5-10.6 months) were detected with all the methods.

BL Lac

The short-term timescales of the detected QPOs in the radio curves of BL Lac can be found in table 5.9.

Table 5.9: Period of the detected STVs in the radio curves of BL Lac at 15 GHz.

JD	Duration	Discrete Fourier Transform (P04)			Fast Fourier Transform (Python)			Lomb-Scargle Periodogram		
	(days)	Period (days)	Amplitude	S/N	Period (days)	Amplitude	S/N	Period (days)	Amplitude	S/N
2454908-2459202	4294	245.47 ± 1.65	0.47 ± 0.09	3.8	248.25	0.13	7.6			
		66.339 ± 0.16	0.34 ± 0.09	2.8	66.20	0.33	49.1			
		43.38 ± 0.07	0.36 ± 0.09	2.9	43.17	0.12	6.7			

The timescale of the shortest detected QPO is 43 days (1.5 months).

The short-term timescales of the detected QPOs at 15 GHz of all the targets can be seen in Fig. 5.8.

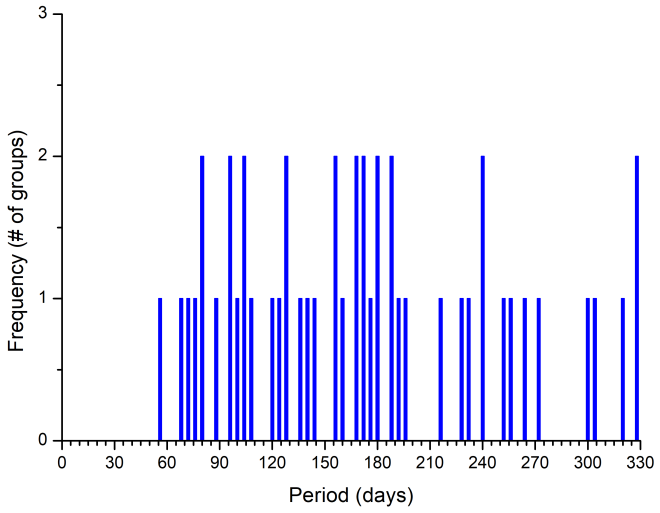

Figure 5.8: Frequency histogram of the detected period of STVs at 15 GHz, in 4-day bins.

The detected STVs have periods from 52 to 328 days.

5.6.3 Short-term QPOs at 4.8 GHz

The results from the search of QPOs of short-term timescales in the radio curves at 4.8 GHz can be found below. The tables with the detected periods can be found in Appendix G.3.

OJ 287

The short-term timescales of the detected QPOs in the radio curve of OJ 287 can be found in table 5.10.

Table 5.10: Period of the detected STVs in the radio curves of OJ 287 at 4.8 GHz.

JD	Duration	Discrete Fourier Transform (P04)			Fast Fourier Transform (Python)			Lomb-Scargle Periodogram		
	(days)	Period (days)	Amplitude	S/N	Period (days)	Amplitude	S/N	Period (days)	Amplitude	S/N
2457716-2459242	1526	28.017 ± 0.036	0.402 ± 0.051	6.4	26.63	0.23	3.2	28.02	0.61	15.6
		16.555 ± 0.011	0.459 ± 0.051	7.3				16.55	0.60	15.1

The detected STVs have timescales of 16 days and 26-28 days.

Mrk 421

The short-term timescales of the detected QPOs in the radio curve of Mrk 421 can be found in table 5.11.

Table 5.11: Period of the detected STVs in the radio curves of Mrk 421 at 4.8 GHz.

JD	Duration	Discrete Fourier Transform (P04)			Fast Fourier Transform (Python)			Lomb-Scargle Periodogram		
	(days)	Period (days)	Amplitude	S/N	Period (days)	Amplitude	S/N	Period (days)	Amplitude	S/N
2457777-2459243	1466	23.527 ± 0.024	0.026 ± 0.003	6.5				23.12	0.69	7.8
		18.696 ± 0.010	0.038 ± 0.003	9.5				18.14	0.58	5.5
		17.639 ± 0.012	0.030 ± 0.003	7.4				17.42	0.57	5.2
		11.734 ± 0.004	0.041 ± 0.003	10.4				11.15	0.66	7.1

The shortest detected STV is 11 to 12 days, with a possible harmonic of 23 days.

Mrk 501

The short-term timescales of the detected QPOs in the radio curves of Mrk 501 can be found in table 5.12.

Table 5.12: Period of the detected STVs in the radio curves of Mrk 501 at 4.8 GHz.

JD	Duration	Discrete Fourier Transform (P04)			Fast Fourier Transform (Python)			Lomb-Scargle Periodogram		
	(days)	Period (days)	Amplitude	S/N	Period (days)	Amplitude	S/N	Period (days)	Amplitude	S/N
2457777-2459243	1466	29.819 ± 0.071	0.036 ± 0.008	3.8				29.81	0.51	5.1
		10.254 ± 0.007	0.046 ± 0.008	4.9				10.24	0.62	7.7

The shortest detected STV has a period of 10 days with a possible harmonic of 29 days.

BL Lac

The short-term timescales of the detected QPOs in the radio curves of BL Lac can be found in table 5.13.

Table 5.13: Period of the detected STVs in the radio curves of BL Lac at 4.8 GHz.

JD	Duration	Discrete Fourier Transform (P04)			Fast Fourier Transform (Python)			Lomb-Scargle Periodogram		
	(days)	Period (days)	Amplitude	S/N	Period (days)	Amplitude	S/N	Period (days)	Amplitude	S/N
2458291 - 2459330	1039	18.52 ± 0.02	0.09 ± 0.01	5.2	18.65	0.04	1.7			
		15.90 ± 0.03	0.07 ± 0.01	3.0	16.43	0.04	1.9			
		11.26 ± 0.01	0.19 ± 0.01	5.3	11.69	0.04	2.2			

The shortest detected QPO has a timescale of 11 days.

The timescales of the detected QPOs at 37 GHz of all the targets can be seen in Fig. 5.9.

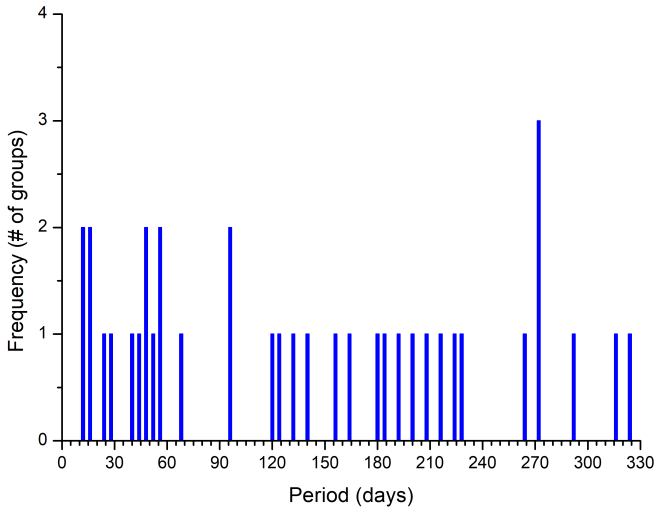

Figure 5.9: Frequency histogram of the detected period of STVs at 37 GHz, in 4-day bins.

The detected QPOs have timescales between 4 and 40 days, but most of the detected STVs are in the range of 4 to 20 days, and a peak at 268-272 days. QPOs of greater timescales have been detected but due to the duration of the observations and the reliability limit we set in the search of the frequencies, those are less frequently detected.

5.7 Search for Long-Term Variability (LTV)

The methods mentioned in paragraphs 3.1 and 3.2 were not implemented in the search of LTV on radio wavelengths. We searched for fluctuations and trends in the radio curves of the targets (Fig. 5.4, 5.5, and 5.6).

5.7.1 Long-term variability at 37 GHz

OJ 287

The radio curve of OJ 287 shows high variability, with multiple flare events in mid-2014, early

2017 and early 2018. The target was in high state from September 2016 to July 2017.

Mrk 421

There is no significant trend in the radio curve of Mrk 421 at 37 GHz.

Mrk 501

There is no significant trend in the radio curve of Mrk 501 at 37 GHz.

BL Lac

BL Lac is high variable with multiple flare events during the period that it was observed. The radio curve shows a downward trend from 2013 to mid 2019, and an upward trend from mid-2019 until the end of the observations.

5.7.2 Long-term variability at 15 GHz

OJ 287

The radio curve of OJ 287 shows high variability, with multiple flare events. The target was in high state from September 2016 until mid 2017, followed by a high increase of flux during a flare in early 2018. The radio curve at 15 GHz follows the behavior of the radio curve at 37 GHz.

Mrk 421

In the radio curve of Mrk 421 multiple flares can be detected. Also a downward trend can be seen, from 2013 until the flare of mid-2014, and from mid-2014 until 2019.

Mrk 180

There is no significant trend in the radio curve of Mrk 180 at 15 GHz, only a small downward trend from early 2015 until the end of the observations.

Mrk 501

Mrk 501 is highly variable at 15 GHz. An upward trend can be seen in the radio curve of the target from 2013 until mid-2015, followed by a decrease of flux from mid-2015 until early 2018. The flux was in an upward trend again from 2018 until the end of the observations.

BL Lac

The radio curve of BL Lac at 15 GHz shows great variability, with multiple flares. From 2013, until the flare in mid-2017 an upward trend can be seen in the radio curve, and a downward trend can be detected after the same flare until the end of the observations.

5.7.3 Long-term variability at 4.8 GHz

OJ 287

OJ 287 is highly variable and shows great decreasement of its flux in late 2017 and in late 2019.

Mrk 421

There are no enough data to search for a trend in the radio curve of Mrk 421 at 4.8 GHz.

Mrk 501

There are no enough data to search for a trend in the radio curve of Mrk 501 at 4.8 GHz.

BL Lac

The radio curve of BL Lac shows variability at 4.8 GHz. An upward trend can be seen from late 2019 until the end of the observations.

Chapter 6

Search for QPOs in X-rays

The data used for the search of QPOs in X-rays were acquired by the Neil Gehrels Swift Observatory by the X-ray telescope (XRT) in the frame of long-term Swift monitoring program of Fermi gamma-ray sources (Stroh & Falcone, 2013).

6.1 Neil Gehrels Swift Observatory

Neil Gehrels Swift Observatory or Swift is a multi-wavelength space observatory, with three instruments observing at gamma-rays, X-rays, ultraviolet and optical wavelengths. The Burst Alert Telescope (BAT) that observes in an energy range of 15-150 keV, the Ultraviolet/Optical Telescope (UVOT) that observes in ultraviolet and optical wavelengths and the X-Ray Telescope (XRT) that has an energy range from 0.2 to 10 keV.

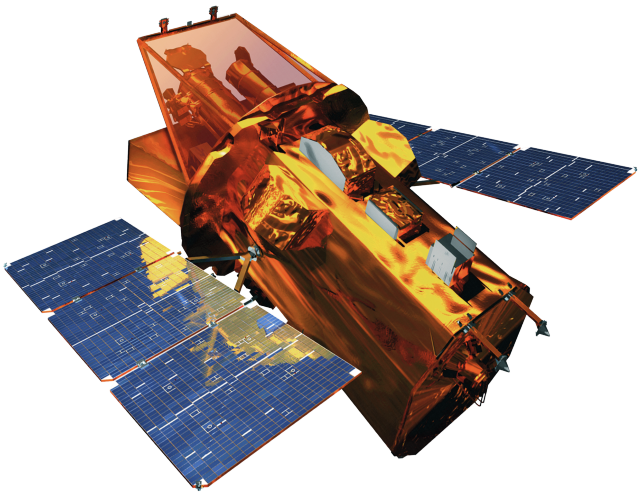

Figure 6.1: Model of Neil Gehrels Swift Observatory.

The XRT uses a grazing incidence Wolter Type I X-ray telescope with 12 nested mirrors. It has an effective area of 110 cm^2, with a 23.6×23.6 arcmin FOV, and a 18 arcsec resolution (half-power diameter). The telescope focuses on a CCD that has an image area of 600×602 pixels (40×40 microns), and operates at $-100°$ C to ensure low electronic noise.

6.2 Data acquisition

The *BOSS Project* targets that were observed by the Swift-XRT and their observing information can be found in table 6.1.

Table 6.1: Observing information of the Swift-XRT targets.

Target	**Number of nights**
1H 0323+342	152
PKS 0716+714	282
1ES 0836+71	87
OJ 287	699
PKS 0954+658	65
Mrk421	1193
3C 273	318
3C 279	370
PKS 1510-089	273
PKS 1553+113	359
Mrk501	764
1ES 1959+650	545
BL Lac	616
CTA102	145
3C 454.3	427
1ES 2344+514	220

The data were grouped in 1-day bins with the code of Appendix C. The flux sequence of the AGNs in X-rays are plotted below. In order to create the flux sequences the data are grouped in one-day bins.

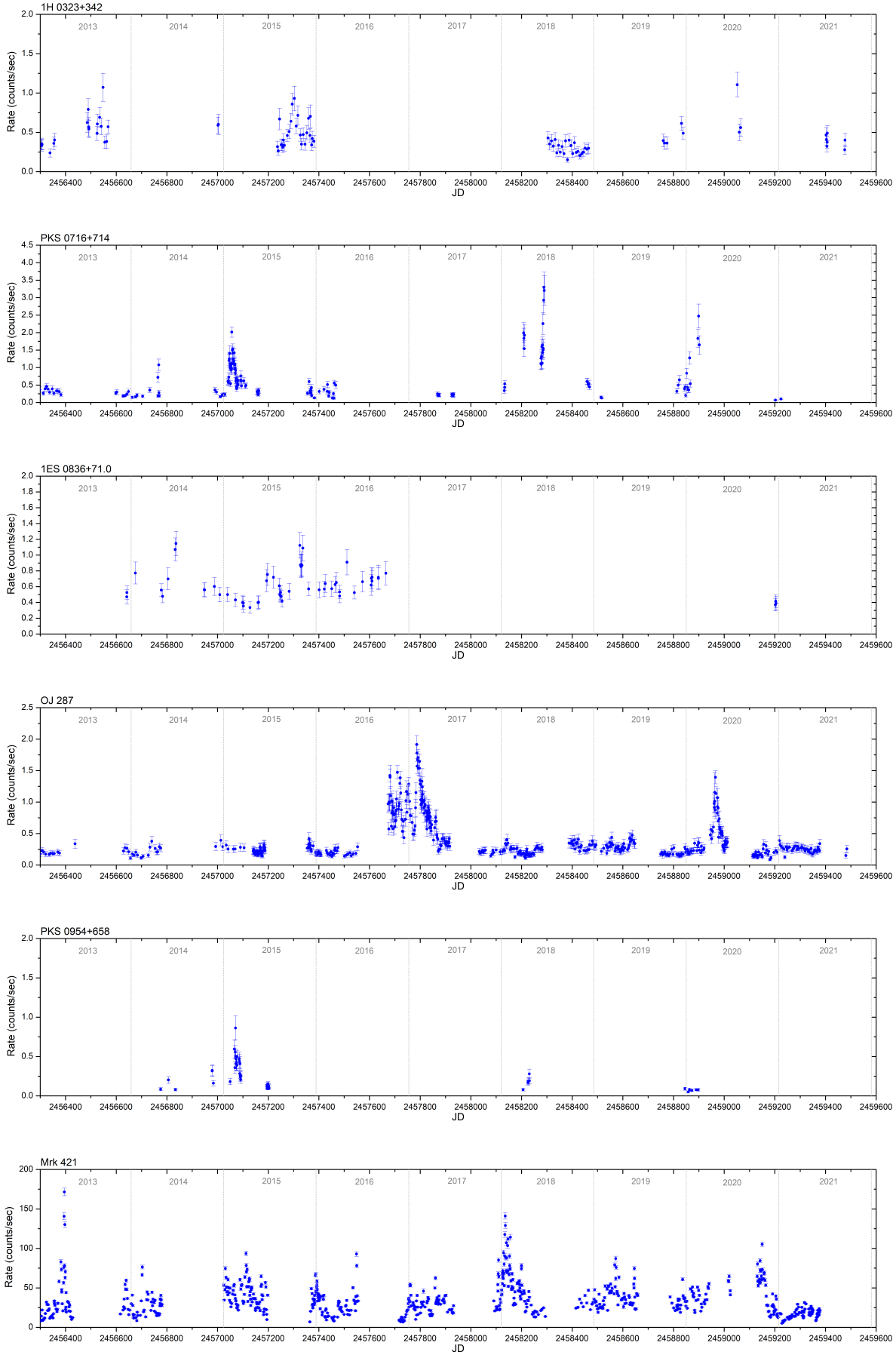

Figure 6.2: The flux sequence of the first 6 targets of table 6.1.

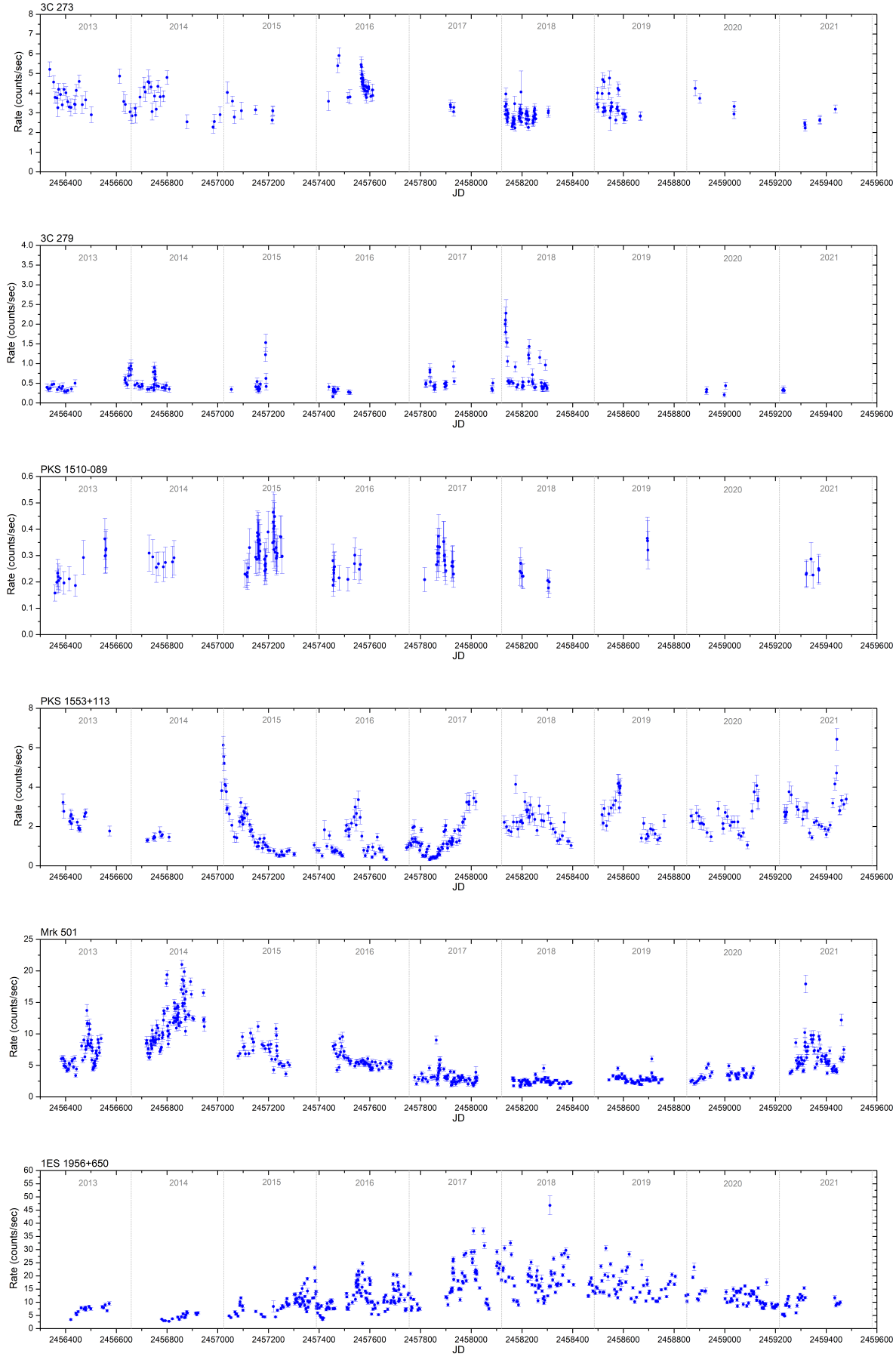

Figure 6.3: The flux sequence of the next 6 targets of table 6.1.

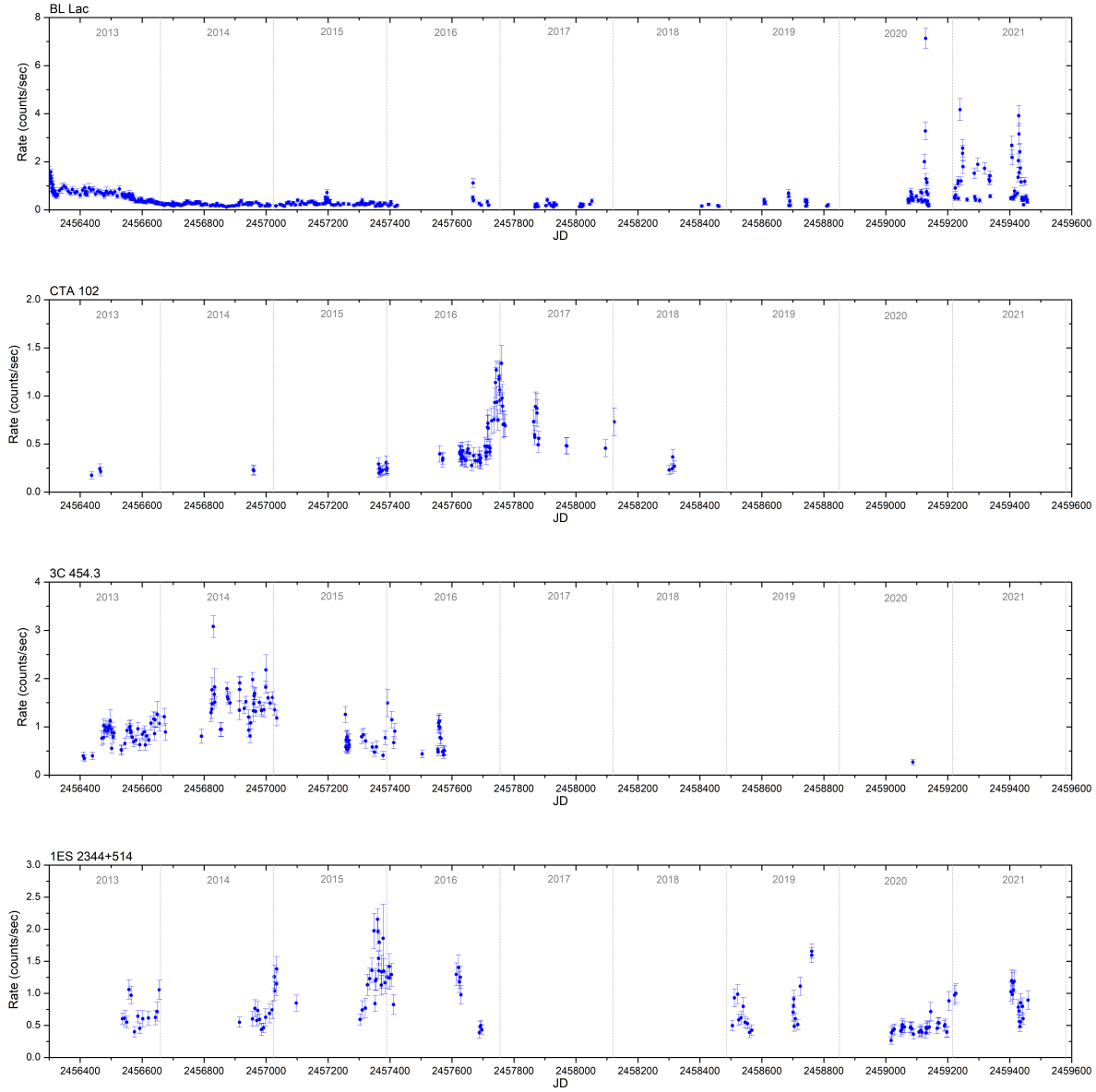

Figure 6.4: The flux sequence of the last 4 targets of table 6.1.

6.3 Data analysis

The data were analysed using the Discrete Fourier Transform and the Lomb-Scargle Periodogram, described in paragraphs 3.1 and 3.2.

6.4 Search for QPOs of intra-day timescales

In order to search for Quasi-Periodic oscillations with timescales of less than a day, high-cadence intra-day flux sequences are required. Thus IDVs were searched whenever it was possible, using the unbinned data.

The frequency limits for the search of periodic IDV are set based on the observations. The upper limit of frequency is 250 cycles per day (cpd), which corresponds to a period of 5.6 minutes. The lower limit is set as 1/t (cpd), where t is the total duration of the observations (in days). The range of reliability of the detected frequencies is set from 2/t cpd, in order to detect at least two oscillations during the observations, to 125 cpd, which corresponds roughly to 10 minutes, because we need at least 5 to 6 points to fit the trigonometric functions. A threshold was set in order to have at least 99% confidence in the detected periods. Also only the periods detected with at least two methods are considered significant. We set a limit of 3-5 minutes that we assume the detected periods are the same.

The results from the search of QPOs of intra-day timescales can be found below. The tables with the intra-day QPOs of each target can be found in Appendix H.1.

We assume that QPOs of intra-day timescales originate from instabilities that occur in the inner region of the AD and the quasi-periodic signal is either observed directly from the AD or it propagates along the jet of the source. A scale factor for the radius of the region that the instabilities arise, hence referred as ***region of origin***, and for the parameters of the SMBH, such as the mass of the BH, the Eddington luminosity and the upper accretion rate can be calculated. The parameters are calculated for a non-rotating and maximally rotating BH, and for emission that either comes from the AD or from the jet, thus the Doppler factor is considered in the calculations. The Doppler factor cannot be extracted directly from observations, but it has been estimated with different methods, thus many values for the Doppler factor have been proposed. Throughout this thesis the value of Doppler factor that was used is 6.87, which is based on a model suggested by Pei et al. (2022). Since we assumed that the periods detected with different methods are the same within a limit of 3-5 minutes, we use the mean value of these periods in order to calculate the parameters of the inner region of the AGN. The error in the calculation of the parameters is estimated based on the uncertainty of the detected timescales.

1H 0323+342

One X-ray intra-day flux sequence was studied in order to search for QPOs in 1H 0323+342. The timescales that were detected with at least 99% confidence can be found in table 6.2.

Table 6.2: Period of the detected IDVs in the X-ray flux sequence of 1H 0323+342.

JD	Duration (min)	Discrete Fourier Transform (P04)			Fast Fourier Transform (Python)			Lomb-Scargle Periodogram		
		Period (min)	Amplitude	S/N	Period (min)	Amplitude	S/N	Period (min)	Amplitude	S/N
2453922	1167.02	37.99 ± 0.23	0.06 ± 0.02	3.4	37.29	0.07	2.4	31.47	0.69	12.3
					31.62	0.06	2.1			

The timescales of the detected QPO are 31 and 37 minutes.

Since we only have searched for QPOs in only one flux sequence, we will assume that the timescale of 31 minutes, that was the shortest detected timescales, relates to fluctuations that originate in the marginally stable orbit in the AD, we can calculate the lower bound of the mass of the BH using equations 1.14 and 1.15. The calculated masses can be seen in table 6.3.

Table 6.3: The calculated mass of the SMBH of 1H 0323+342.

$\mathbf{M_{BH}(10^7 M_\odot)}$	Non-rotating BH	Rotating BH
M_{stable}	0.39 ± 0.02	2.44 ± 0.12
$M_{stable}(\delta)$	2.64 ± 0.13	16.80 ± 0.81

Based on spectroscopic data the mass of the SMBH of 1H 0323+342 is $M = 2 \times 10^7 M_\odot$

(Landt et al., 2017). This value is in line with the calculated lower limit of mass of a non-rotating black hole for non-Doppler boosted emission. 1H 0323+342 is a quasar, so its emission probably comes from the AD of the AGN, thus it is not Doppler boosted.

From the calculated mass, we can calculate the minimum radius of the stable orbit using equations 1.13. The radii of the region of origin, in case of a non-rotating and a maximally rotating BH, can be seen in table 6.4.

Table 6.4: Radii of region of origin of IDV of 1H 0323+342.

$\mathbf{R(10^{10}m)}$	**Non-rotating BH**	**Rotating BH**
R_{stable}	3.40 ± 0.17	4.33 ± 0.21
$R_{stable}(\delta)$	23.40 ± 1.13	29.70 ± 1.44

From the mass of the SMBH we can also calculate the lower bound of the Eddington luminosity using equation 1.1. The calculated luminosities can be seen in table 6.5.

Table 6.5: The calculated Eddington luminosity of 1H 0323+342.

$\mathbf{L_{Edd}(10^{12}L_{\odot})}$	**Non-rotating BH**	**Rotating BH**
$L_{Edd_{stable}}$	0.12 ± 0.01	0.78 ± 0.04
$L_{Edd_{stable}}(\delta)$	0.85 ± 0.04	5.37 ± 0.26

From Eddington luminosity we can calculate the Eddington accretion rate of the black hole, using equation 1.4. The calculated accretion rate can be found in table 6.6.

Table 6.6: The upper limit of accretion rate of 1H 0323+342.

$\mathbf{M_{BH}(M_{\odot}/yr)}$	**Non-rotating BH**	**Rotating BH**
$\dot{M}_{stable}$	0.085 ± 0.004	0.538 ± 0.026
$\dot{M}_{stable}(\delta)$	0.581 ± 0.028	3.693 ± 0.179

PKS 0716+714

In order to search for intra-day QPOs in X-rays in PKS 0716+714, two high-cadence flux sequences were studied. The detected timescales can be found in table 6.7.

Table 6.7: Period of the detected IDVs in the X-ray flux sequence of PKS 0716+714.

JD	Duration (min)	Discrete Fourier Transform (P04)			Fast Fourier Transform (Python)			Lomb-Scargle Periodogram		
		Period (min)	Amplitude	S/N	Period (min)	Amplitude	S/N	Period (min)	Amplitude	S/N
2457061	1069.89	33.55 ± 0.21	0.07 ± 0.02	3.7	35.14	0.11	3.5			
2457062	1318.67	260.31 ± 8.36	0.06 ± 0.02	2.2	257.76	0.09	2.5			
		49.73 ± 0.21	0.09 ± 0.02	4.3	51.55	0.10	3.1			

The shortest detected QPO has a timescale of 34 minutes. IDV of 50 and 257-260 minutes were also detected with at least 99% confidence.

The radius of the region of origin and the parameters of the SMBH of PKS 0716+714 were calculated in a previous chapter using the detected timescales of QPOs in optical. The shortest detected QPO is of the same scales in both X-rays and optical wavelengths, thus the calculated parameters are of the same scale.

1ES 0836+71

Two high-cadence X-ray flux sequences were studied in order to search for QPOs in 1ES 0836+71. The timescales detected with at least 99% confidence can be found in table 6.8.

Table 6.8: Period of the detected IDVs in the X-ray flux sequence of 1ES 0836+71.

JD	Duration (min)	Discrete Fourier Transform (P04)			Fast Fourier Transform (Python)			Lomb-Scargle Periodogram		
		Period (min)	Amplitude	S/N	Period (min)	Amplitude	S/N	Period (min)	Amplitude	S/N
2454194	1361.8224									
2454849	882.42	73.76 ± 1.33	0.02 ± 0.01	4.5	73.80	0.0	2.4			
		34.59 ± 0.22	0.02 ± 0.01	4.8	32.80	0.0	2.5			

In one of the two days of observations no significant QPO was detected. The shortest detected QPO has a timescale of 32-34 minutes. Also an IDV of 73 minutes was detected.

Assuming that the QPO originate from the inner region of the AD and that the timescale of 180-184 minutes, that was detected in most light-curves, relates to fluctuations that originate in the marginally stable orbit, we can calculate the lower bound of the mass of the BH using equations 1.14 and 1.15. The calculated masses can be seen in table 6.9.

Table 6.9: The calculated mass of the SMBH of 1ES 0836+71.

$\mathbf{M_{BH}(10^6 M_\odot)}$	Non-rotating BH	Rotating BH
M_{stable}	1.36 ± 0.06	8.61 ± 0.39
$M_{stable}(\delta)$	9.31 ± 0.42	59.2 ± 0.27

Based on spectroscopic data, the mass of the SMBH of 1ES 0836+71 is $M = 3 \times 10^9 M_\odot$ (Ghisellini et al., 2010), and is in line with the lower bound set by the detected timescales of QPOs.

From the calculated mass, we can calculate the minimum radius of the stable orbit using equations 1.13. The radii of the region of origin, in case of a non-rotating and a maximally rotating BH, can be seen in table 6.10.

Table 6.10: Radii of region of origin of IDV of 1ES 0836+71.

$\mathbf{R(10^{10}m)}$	**Non-rotating BH**	**Rotating BH**
R_{stable}	1.20 ± 0.05	1.52 ± 0.07
$R_{stable}(\delta)$	8.24 ± 0.38	10.50 ± 0.48

From the mass of the SMBH we can also calculate the lower bound of the Eddington luminosity using equation 1.1. The calculated luminosities can be seen in table 6.11.

Table 6.11: The calculated Eddington luminosity of 1ES 0836+71.

$\mathbf{L_{Edd}(10^{10}L_\odot)}$	**Non-rotating BH**	**Rotating BH**
$L_{Edd_{stable}}$	4.34 ± 0.20	27.60 ± 1.25
$L_{Edd_{stable}}(\delta)$	29.80 ± 1.35	189.00 ± 8.61

From Eddington luminosity we can calculate the Eddington accretion rate of the black hole, using equation 1.4. The calculated accretion rate can be found in table 6.12.

Table 6.12: The upper limit of accretion rate of 1ES 0836+71.

$\mathbf{\dot{M}_{BH}(M_\odot/yr)}$	**Non-rotating BH**	**Rotating BH**
$\dot{M}_{stable}$	0.030 ± 0.001	0.190 ± 0.009
$\dot{M}_{stable}(\delta)$	0.205 ± 0.009	1.302 ± 0.059

Mrk 421

A total of 15 high-cadence X-ray flux sequences were studied in order to earch for QPOs in Mrk 421. The detected timescales can be found in table H.5 in Appendix H.1.

The shortest detected IDV is 7-8 minutes. The detected timescales of IDVs can be found in the frequency histogram of Fig. 6.5, that shows the detected QPOs grouped in 4-minute bins.

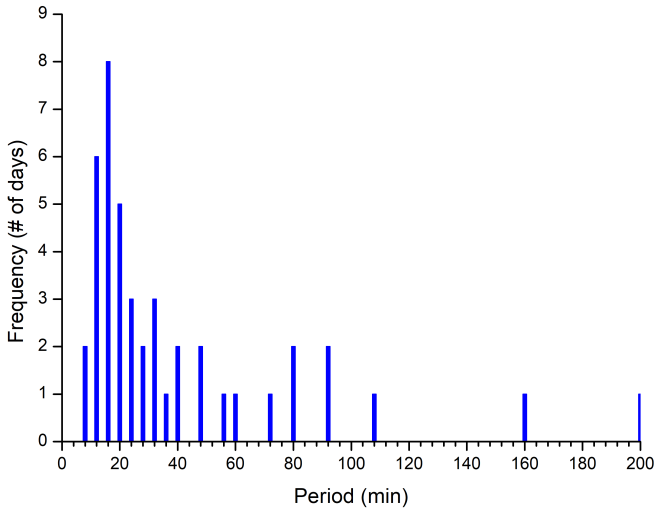

Figure 6.5: Frequency histogram of the detected period of IDVs of Mrk 421 in X-rays, in 4-minute bins. The data used to create this histogram can be found in table H.5 in Appendix H.1.

A QPO with timescale of 12-16 minutes was detected in 8 out of 15 days. The timescales of QPOs range from 7 to 200 minutes, but most of the IDVs are between 7 and 33 minutes.

The detected QPOs are in the same scale with the ones detected in optical wavelengths, thus the parameters calculated in the previous chapter are the same for both optical and X-rays.

3C 273

In order to search for QPOs of intra-day timescales a total of 15 flux sequences were studied. The detected timescales of QPOs in X-rays, with at least 99% in detection, can be found in table H.6 in Appendix H.1.

The shortest detected IDV is 6-7 minutes. The detected timescales of QPOs can be found in the frequency histogram of Fig. 6.6, which shows the detected QPOs grouped in 4-minute bins.

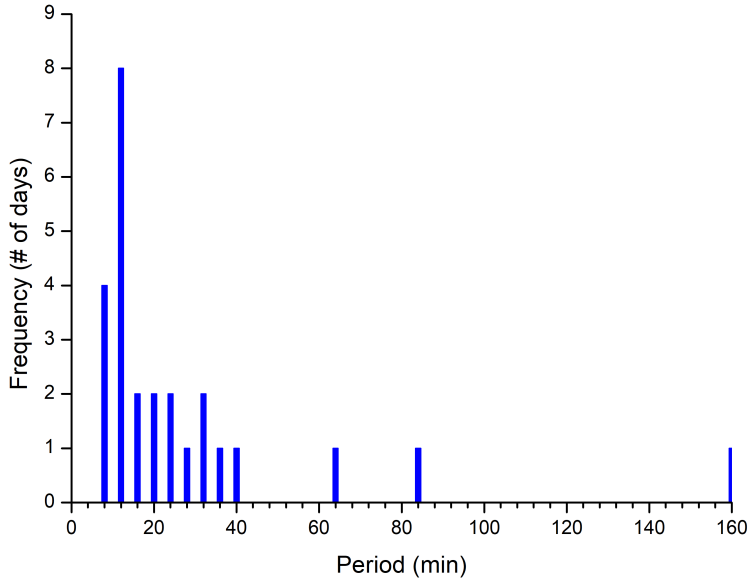

Figure 6.6: Frequency histogram of the detected period of IDVs of 3C 273 in X-rays, in 4-minute bins. The data used to create this histogram can be found in table H.6 in Appendix H.1.

In 8 out of 15 flux sequences, a QPO with a timescale of 8-12 minutes has been detected. Also most of the IDVs have periods between 6 and 32 minutes.

Assuming that the QPO originate from the inner region of the AD and that the timescale of 180-184 minutes, that was detected in most light-curves, relates to fluctuations that originate in the marginally stable orbit, we can calculate the lower bound of the mass of the BH using equations 1.14 and 1.15. The calculated masses can be seen in table 6.13.

Table 6.13: The calculated mass of the SMBH of 3C 273.

$\mathbf{M_{BH}(10^6 M_\odot)}$	**Non-rotating BH**	**Rotating BH**
M_{stable}	1.25 ± 0.17	7.96 ± 1.09
$M_{stable}(\delta)$	8.61 ± 1.17	54.70 ± 7.46

The mass of the SMBH of 3C 273 was calculated using the reverberation method to be $M = 6.6 \times 10^9 M_\odot$ (Paltani & Türler, 2005). This value is greater than the lower limit calculated using the timescales of QPOs.

From the calculated mass, we can calculate the minimum radius of the stable orbit using equations 1.13. The radii of the region of origin, in case of a non-rotating and a maximally rotating BH, can be seen in table 6.14.

Table 6.14: Radii of region of origin of IDV of 3C 273.

$\mathbf{R(10^{10}m)}$	**Non-rotating BH**	**Rotating BH**
R_{stable}	1.11 ± 0.15	1.41 ± 0.19
$R_{stable}(\delta)$	7.62 ± 1.04	9.68 ± 1.32

From the mass of the SMBH we can also calculate the lower bound of the Eddington luminosity using equation 1.1. The calculated luminosities can be seen in table 6.15.

Table 6.15: The calculated Eddington luminosity of 3C 273.

$\mathbf{L_{Edd}(10^{10}L_{\odot})}$	**Non-rotating BH**	**Rotating BH**
$L_{Edd_{stable}}$	4.01 ± 0.55	25.50 ± 3.47
$L_{Edd_{stable}}(\delta)$	27.50 ± 3.76	175.00 ± 23.90

From Eddington luminosity we can calculate the Eddington accretion rate of the black hole, using equation 1.4. The calculated accretion rate can be found in table 6.16.

Table 6.16: The upper limit of accretion rate of 3C 273.

$\mathbf{\dot{M}_{BH}(M_{\odot}/yr)}$	**Non-rotating BH**	**Rotating BH**
$\dot{M}_{stable}$	0.028 ± 0.004	0.175 ± 0.024
$\dot{M}_{stable}(\delta)$	0.189 ± 0.026	1.2032 ± 0.164

3C 279

A total of 8 X-ray flux sequences were studied in order to find QPOs of intra-day timescales in 3C 279. The detected timescales can be found in table 6.17.

Table 6.17: Period of the detected IDVs in the X-ray flux sequence of 3C 279.

JD	Duration (min)	Discrete Fourier Transform (P04)			Fast Fourier Transform (Python)			Lomb-Scargle Periodogram		
		Period (min)	Amplitude	S/N	Period (min)	Amplitude	S/N	Period (min)	Amplitude	S/N
2453748	1375.42	8.91 ± 0.01	0.02 ± 0.01	4.6	8.60	0.04	4.7			
2453749	1358.58	12.85 ± 0.02	0.03 ± 0.01	4.3	11.62	0.05	4.0			
2453752	1367.61	24.43 ± 0.09	0.013 ± 0.005	3.7	27.05	0.02	2.4			
		10.67 ± 0.01	0.020 ± 0.005	5.0	12.22	0.02	2.1			
		8.70 ± 0.01	0.018 ± 0.005	4.6	8.42	0.02	2.7			
2453753	1363.68	11.65 ± 0.02	0.02 ± 0.01	2.8	10.02	0.03	2.3			
2454795	794.02	8.14 ± 0.02	0.02 ± 0.01	5.0	9.12	0.04	2.1			
2454796	1167.84	7.42 ± 0.01	0.03 ± 0.01	3.5	8.11	0.05	5.2			
2454799	1256.28	72.31 ± 0.59	0.02 ± 0.01	3.3	70.27	0.04	8.1			
		10.35 ± 0.02	0.01 ± 0.01	4.3	11.33	0.04	5.9			
		8.91 ± 0.01	0.02 ± 0.01	4.7	8.37	0.03	2.8			
2454800	1162.63	101.92 ± 0.65	0.07 ± 0.01	8.7	23.20	0.06	5.3	102.85	0.46	2.1
		23.32 ± 0.09	0.03 ± 0.01	8.0						

The shortest detected timescale is 8 minutes, which is also the timescale that was detected in 5 out of 8 days, thus it possibly corresponds to a QPO.

Assuming that the QPO originate from the inner region of the AD and that the timescale of 8 minutes, that was detected in most light-curves, relates to fluctuations that originate in the marginally stable orbit, we can calculate the lower bound of the mass of the BH using equations 1.14 and 1.15. The calculated masses can be seen in table 6.18.

Table 6.18: The calculated mass of the SMBH of 3C 279.

$\mathbf{M_{BH}(10^5 M_\odot)}$	Non-rotating BH	Rotating BH
M_{stable}	6.87 ± 1.29	43.60 ± 8.18
$M_{stable}(\delta)$	47.20 ± 8.85	300.00 ± 56.20

The mass of the SMBH of 3C 279 was estimated to be $M = 8 \times 10^8 M_\odot$ using the empirical correlation between the bulge luminosity and the central BH mass (Nilsson et al., 2009). The estimated mass is in line with the lower limit set by the detected QPOs.

From the calculated mass, we can calculate the minimum radius of the stable orbit using equations 1.13. The radii of the region of origin, in case of a non-rotating and a maximally rotating BH, can be seen in table 6.19.

Table 6.19: Radii of region of origin of IDV of 3C 279.

$\mathbf{R(10^9 m)}$	Non-rotating BH	Rotating BH
R_{stable}	6.08 ± 1.14	7.73 ± 1.45
$R_{stable}(\delta)$	41.80 ± 7.83	53.10 ± 9.95

From the calculated mass of the SMBH we can calculate the lower limit of the Eddington luminosity using equation 1.1. The calculated luminosities can be seen in table 6.20.

Table 6.20: The calculated Eddington luminosity of 3C 279.

$\mathbf{L_{Edd}(10^{11}L_\odot)}$	**Non-rotating BH**	**Rotating BH**
$L_{Edd_{stable}}$	0.22 ± 0.04	1.40 ± 0.26
$L_{Edd_{stable}}(\delta)$	1.51 ± 0.28	9.59 ± 1.80

From Eddington luminosity we can calculate the lower limit of the Eddington accretion rate of the black hole, using equation 1.4. The calculated accretion rate can be found in table 6.21.

Table 6.21: The upper limit of accretion rate of 3C 279.

$\mathbf{M_{BH}(M_\odot/yr)}$	**Non-rotating BH**	**Rotating BH**
$\dot{M}_{stable}$	0.015 ± 0.003	0.096 ± 0.018
$\dot{M}_{stable}(\delta)$	0.104 ± 0.019	0.660 ± 0.124

PKS 1553+113

In order to search for QPOs in PKS 1553+113, a total of 3 flux sequences were studied. The intra-day timescales of the detected QPOs can be found in table 6.22.

Table 6.22: Period of the detected IDVs in the X-ray flux sequence of PKS 1553+113.

JD	**Duration (min)**	**Discrete Fourier Transform (P04)**			**Fast Fourier Transform (Python)**			**Lomb-Scargle Periodogram**		
		Period (min)	**Amplitude**	**S/N**	**Period (min)**	**Amplitude**	**S/N**	**Period (min)**	**Amplitude**	**S/N**
2453649	1262.46	41.97 ± 0.17	0.26 ± 0.06	4.3	40.32	0.32	3.3			
		30.18 ± 0.08	0.30 ± 0.06	5.7	32.26	0.35	3.9			
		24.22 ± 0.04	0.42 ± 0.06	5.9	23.04	0.37	4.4			
2459235	1352.58									
2459244	1352.95	8.81 ± 0.01	0.22 ± 0.05	7.4	8.29	0.40	4.1			

On 2459235 no significant QPO was detected. The shortest detected IDV is 8 minutes, with a possible harmonics of 23-24 and 30-32 minutes.

Since no timescale was detected in both days, we assume that the timescale of 8 minutes relates to QPOs that arise from the marginally stable orbit of the AD. We can calculate the lower bound of the mass of the BH using equations 1.14 and 1.15. The calculated masses can be seen in table 6.23.

Table 6.23: The calculated mass of the SMBH of PKS 1553+113.

$\mathbf{M_{BH}(10^5M_\odot)}$	**Non-rotating BH**	**Rotating BH**
M_{stable}	7.76 ± 1.45	49.30 ± 9.24
$M_{stable}(\delta)$	53.30 ± 9.99	339.00 ± 63.50

PKS 1553+113 is a black hole binary system, that its variability can be interpret with a two-jet precession model (Huang et al., 2021). The mass of the primary black hole was estimated to be $M = 3.47 \times 10^8 M_\odot$ based on the relation between jets and accretions disks (Huang et al., 2021). This value is in line with the lower limit set by the detected QPOs.

From the calculated mass, we can calculate the minimum radius of the stable orbit using equations 1.13. The radii of the region of origin, in case of a non-rotating and a maximally rotating BH, can be seen in table 6.24.

Table 6.24: Radii of region of origin of IDV of PKS 1553+113.

$\mathbf{R(10^9 m)}$	**Non-rotating BH**	**Rotating BH**
R_{stable}	6.87 ± 1.29	8.73 ± 1.64
$R_{stable}(\delta)$	47.20 ± 8.84	59.90 ± 11.20

From the mass of the SMBH we can calculate the lower limit of the Eddington luminosity using equation 1.1. The calculated luminosities can be seen in table 6.25.

Table 6.25: The calculated Eddington luminosity of PKS 1553+113.

$\mathbf{L_{Edd}(10^{10} L_\odot)}$	**Non-rotating BH**	**Rotating BH**
$L_{Edd_{stable}}$	2.48 ± 0.47	15.80 ± 2.96
$L_{Edd_{stable}}(\delta)$	17.10 ± 3.20	108.00 ± 20.30

From Eddington luminosity we can calculate the lower bound of the Eddington accretion rate of the BH, using equation 1.4. The calculated accretion rate can be found in table 6.26.

Table 6.26: The upper limit of accretion rate of PKS 1553+113.

$\mathbf{\dot{M}_{BH}(M_\odot/yr)}$	**Non-rotating BH**	**Rotating BH**
$\dot{M}_{stable}$	0.017 ± 0.003	0.108 ± 0.020
$\dot{M}_{stable}(\delta)$	0.117 ± 0.022	0.745 ± 0.140

Mrk 501

A total of 6 high-cadence X-ray flux sequences were studied in order to search for QPOs in Mrk 501. The detected timescales can be found in table 6.27.

Table 6.27: Period of the detected IDVs in the X-ray flux sequence of Mrk 501.

JD	Duration (min)	Discrete Fourier Transform (P04)			Fast Fourier Transform (Python)			Lomb-Scargle Periodogram		
		Period (min)	Amplitude	S/N	Period (min)	Amplitude	S/N	Period (min)	Amplitude	S/N
2454395	1402.92	54.43 ± 0.30	0.16 ± 0.04	3.0	56.16	0.2	3.51			
		26.43 ± 0.05	0.23 ± 0.04	8.4	24.07	0.2	4.33			
2454979	1350.06									
2456395	783.82	7.33 ± 0.02	0.08 ± 0.04	2.9	7.43	0.2	3.66			
2456487	402.54	10.78 ± 0.06	0.26 ± 0.10	2.6	10.29	0.4	3.72			
2456748	579.37	11.49 ± 0.06	0.12 ± 0.05	5.4	11.87	0.4	5.45			
2457871	590.00									
		25.75 ± 0.15	0.28 ± 0.07	3.9	25.44	0.4	6.15			

The shortest detected IDV has a period of 6 minutes. In 2 out of 6 light curves QPOs of 10-11 and 25-26 minutes were detected.

Assuming that the QPO originate from the inner region of the AD and that the timescale of 10-11 minutes, that was the shortest most frequently detected timescale, relates to fluctuations that originate in the marginally stable orbit, we can calculate the lower bound of the mass of the BH using equations 1.14 and 1.15. The calculated masses can be seen in table 6.28.

Table 6.28: The calculated mass of the SMBH of Mrk 501.

$\mathbf{M_{BH}(10^6 M_\odot)}$	Non-rotating BH	Rotating BH
M_{stable}	1.28 ± 0.19	8.10 ± 1.22
$M_{stable}(\delta)$	8.76 ± 1.31	55.70 ± 8.35

Based on direct measurements of stellar velocity dispersion the mass of the SMBH of Mrk 501 is estimated to be $M = 1.62 \times 10^9 M_\odot$ (Woo & Urry, 2002). The lower limit of the mass that we calculated based on the detected QPOs is in line with the value of literature.

From the calculated mass, we can calculate the minimum radius of the stable orbit using equations 1.13. The radii of the region of origin, in case of a non-rotating and a maximally rotating BH, can be seen in table 6.29.

Table 6.29: Radii of region of origin of IDV of Mrk 501.

$\mathbf{R(10^{10} m)}$	Non-rotating BH	Rotating BH
R_{stable}	1.13 ± 0.17	1.43 ± 0.22
$R_{stable}(\delta)$	7.75 ± 1.16	9.86 ± 1.48

From the mass of the SMBH we can calculate the lower limit of the Eddington luminosity using equation 1.1. The calculated luminosities can be seen in table 6.30.

Table 6.30: The calculated Eddington luminosity of Mrk 501.

$L_{Edd}(10^{10}L_{\odot})$	Non-rotating BH	Rotating BH
$L_{Edd_{stable}}$	4.08 ± 0.61	25.90 ± 3.89
$L_{Edd_{stable}}(\delta)$	28.00 ± 4.21	178.00 ± 26.70

From Eddington luminosity we can calculate the lower bound of the Eddington accretion rate of the BH, using equation 1.4. The calculated accretion rate can be found in table 6.31.

Table 6.31: The upper limit of accretion rate of Mrk 501.

$\dot{M}_{BH}(M_{\odot}/yr)$	Non-rotating BH	Rotating BH
$\dot{M}_{stable}$	0.028 ± 0.004	0.178 ± 0.027
$\dot{M}_{stable}(\delta)$	0.193 ± 0.029	1.225 ± 0.184

1ES 1959+650

A total of 5 high-cadence flux sequences were studied in order to search for QPOs of intra-day timescales in 1ES 1959+650. The detected timescales can be found in table 6.32.

Table 6.32: Period of the detected IDVs in the X-ray flux sequence of 1ES 1959+650.

JD	Duration (min)	Discrete Fourier Transform (P04)			Fast Fourier Transform (Python)			Lomb-Scargle Periodogram		
		Period (min)	Amplitude	S/N	Period (min)	Amplitude	S/N	Period (min)	Amplitude	S/N
2453479	776.30									
2453878	306.58									
2453882	690.64									
2453883	296.58	55.90 ± 2.23	0.21 ± 0.08	4.3	57.60	0.52	4.5			
		27.45 ± 0.44	0.25 ± 0.08	6.8	28.80	0.50	4.2			
2453884	300.20	79.87 ± 1.35	0.57 ± 0.07	34.6	77.14	0.37	2.4			

In 3 out of 5 flux sequences, no significant QPOs were detected. The shortest detected QPO has a timescale of 27-28 minutes, with a possible harmonic of 55-57 minutes.

Since the detected timescales are detected only once, we will assume that the shortest detected IDV relates to fluctuations that originate in the marginally stable orbit of the AD. we can calculate the lower bound of the mass of the BH using equations 1.14 and 1.15. The calculated masses can be seen in table 6.33.

Table 6.33: The calculated mass of the SMBH of 1ES 1959+650.

$M_{BH}(10^{6}M_{\odot})$	Non-rotating BH	Rotating BH
M_{stable}	3.40 ± 0.19	21.60 ± 1.20
$M_{stable}(\delta)$	23.30 ± 1.30	148.00 ± 8.24

From direct measurements of the velocity dispersion, the mass of the BH of 1ES 1959+650 is estimated to be $M = 1.23 \times 10^{8} M_{\odot}$ (Woo & Urry, 2002). This value is in line with the calculated lower limit that was calculated based on the detected timescales, with the exception

in the case of a maximally rotating BH where the emission is Doppler boosted, but the values are of the same order.

From the calculated mass, we can calculate the minimum radius of the stable orbit using equations 1.13. The radii of the region of origin, in case of a non-rotating and a maximally rotating BH, can be seen in table 6.34

Table 6.34: Radii of region of origin of IDV of 1ES 1959+650.

$\mathbf{R(10^{10}m)}$	**Non-rotating BH**	**Rotating BH**
R_{stable}	3.01 ± 0.17	3.82 ± 0.21
$R_{stable}(\delta)$	20.70 ± 1.15	26.30 ± 1.46

From the mass of the SMBH we can calculate the lower limit of the Eddington luminosity using equation 1.1. The calculated luminosities can be seen in table 6.35.

Table 6.35: The calculated Eddington luminosity of 1ES 1959+650.

$\mathbf{L_{Edd}(10^{11}L_\odot)}$	**Non-rotating BH**	**Rotating BH**
$L_{Edd_{stable}}$	1.09 ± 0.60	6.91 ± 0.38
$L_{Edd_{stable}}(\delta)$	7.47 ± 0.42	47.50 ± 2.64

From Eddington luminosity we can calculate the lower bound of the Eddington accretion rate of the black hole, using equation 1.4. The calculated accretion rate can be found in table 6.36.

Table 6.36: The upper limit of accretion rate of 1ES 1959+650.

$\mathbf{\dot{M}_{BH}(M_\odot/yr)}$	**Non-rotating BH**	**Rotating BH**
$\dot{M}_{stable}$	0.075 ± 0.004	0.475 ± 0.026
$\dot{M}_{stable}(\delta)$	0.513 ± 0.029	3.263 ± 0.181

BL Lac

In order to search for QPOs in X-rays, 2 flux sequences were studied. No significant QPOs with high signal to noise ratio were detected.

The radius of the region of origin and the parameters of the SMBH of BL Lac were calculated in a previous chapter using the detected QPOs in the optical light curves.

3C 454.3

One X-ray flux sequence was studied in order to search for QPOs in 3C 454.3. The detected timescales can be found in table 6.37.

Table 6.37: Period of the detected IDVs in the X-ray flux sequence of 3C 454.3.

JD	Duration (min)	Discrete Fourier Transform (P04)			Fast Fourier Transform (Python)			Lomb-Scargle Periodogram		
		Period (min)	Amplitude	S/N	Period (min)	Amplitude	S/N	Period (min)	Amplitude	S/N
2453485	1366.34	18.46 ± 0.04	0.10 ± 0.03	4.2	18.14	0.14	2.4			

The only detected QPO has a timescale of 18 minutes.

Assuming that the QPO originate from the inner region of the AD and that the timescale of 8 minutes relates to fluctuations that originate in the marginally stable orbit, we can calculate the lower bound of the mass of the BH using equations 1.14 and 1.15. The calculated masses can be seen in table 6.38.

Table 6.38: The calculated mass of the SMBH of 3C 454.3.

$\mathbf{M_{BH}(10^6 M_\odot)}$	Non-rotating BH	Rotating BH
M_{stable}	1.28 ± 0.11	8.11 ± 0.68
$M_{stable}(\delta)$	8.77 ± 0.73	55.70 ± 4.65

The mass of the BH of 3C 454.3 was estimated to be $M = 3.4 \times 10^8 M_\odot$, by using the relation between the radius of the BLR and the mass of the BH and assuming an isotropic velocity filed (Bonnoli et al., 2011). This value is in line with the lower limit calculated by the detected QPOs.

From the calculated mass, we can calculate the minimum radius of the stable orbit using equations 1.13. The radii of the region of origin, in case of a non-rotating and a maximally rotating BH, can be seen in table 6.39

Table 6.39: Radii of region of origin of IDV of 3C 454.3.

$\mathbf{R(10^{10} m)}$	Non-rotating BH	Rotating BH
R_{stable}	1.13 ± 0.09	1.44 ± 0.12
$R_{stable}(\delta)$	7.76 ± 0.65	9.87 ± 0.82

From the mass of the SMBH we can calculate the lower limit of the Eddington luminosity using equation 1.1. The calculated luminosities can be seen in table 6.40.

Table 6.40: The calculated Eddington luminosity of 3C 454.3.

$\mathbf{L_{Edd}(10^{10} L_\odot)}$	Non-rotating BH	Rotating BH
$L_{Edd_{stable}}$	4.09 ± 0.34	26.00 ± 2.16
$L_{Edd_{stable}}(\delta)$	28.10 ± 2.34	178.00 ± 14.90

From lower limit of Eddington luminosity we can calculate the Eddington accretion rate of the black hole, using equation 1.4. The calculated accretion rate can be found in table 6.41.

Table 6.41: The upper limit of accretion rate of 3C 454.3.

$\mathbf{M_{BH}(M_\odot/yr)}$	**Non-rotating BH**	**Rotating BH**
$\dot{M}_{stable}$	0.028 ± 0.002	0.179 ± 0.015
$\dot{M}_{stable}(\delta)$	0.193 ± 0.016	1.226 ± 0.102

The intra-day timescales of the detected QPOs in X-rays of all the targets can be seen in Fig. 6.7.

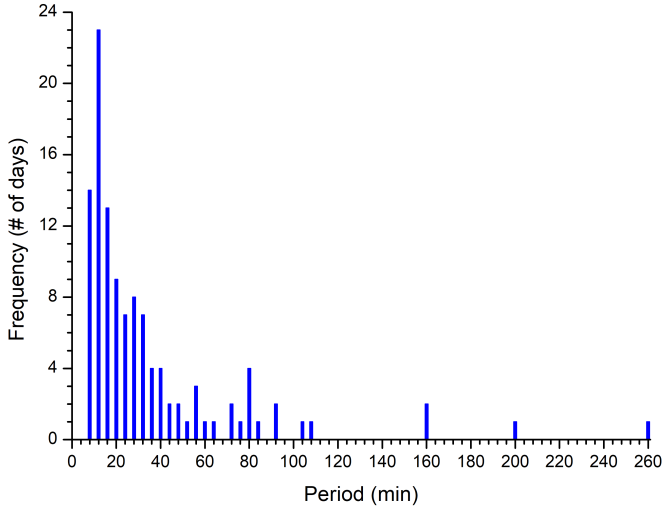

Figure 6.7: Frequency histogram of the detected period of IDVs in X-rays, in 4-minute bins.

The detected QPOs have timescales between 9 and 280 minutes, but most of the detected IDVs are in the range of 9 to 40 minutes, with a smaller peak around 80 minutes. QPOs of greater timescales have been detected but due to the duration of the observations and the reliability limit we set in the search of the frequencies, those are less frequently detected.

6.5 Search for QPOs of short-term timescales

To search for STVs, a large amount of data for several, preferably continuous, nights must be acquired. The data used for the search for STVs were grouped in 1-day bins.

The frequency limits for the search of the period of STVs are set based on the observations. The upper limit of frequency is 0.3 cycles per day (cpd), which corresponds to a period of 3 days. The lower limit is set as 1/t (cpd), where t is the total duration of the observations (in days). The range of reliability of the detected frequencies is set from 2/t cpd, in order to detect at least two oscillations during the observations, to 0.15 cpd, which corresponds to 6 days, because we need at least 5 to 6 points to fit the trigonometric functions. A threshold was set in order to have at least 99% confidence in the detected periods.

The results from the search of QPOs of short-term timescales in optical can be found below. The tables with the short-term QPOs of each target can be found in Appendix H.2.

1ES 0836+71

The short-term timescales of the detected QPOs in the X-ray flux sequence of 1ES 0836+81 can be found in table 6.42.

Table 6.42: Period of the detected STVs in the X-ray flux sequence of 1ES 0836+71.

JD	Duration	Discrete Fourier Transform (P04)			Fast Fourier Transform (Python)			Lomb-Scargle Periodogram		
	(days)	Period (days)	Amplitude	S/N	Period (days)	Amplitude	S/N	Period (days)	Amplitude	S/N
2456675-2457664	989	30.65 ± 0.05	0.13 ± 0.02	4.8				31.11	0.60	3.5

The only detected QPO has a timescale of 30-31 days.

OJ 287

The short-term timescales of the detected QPOs in the X-ray flux sequence of OJ 287 can be found in table 6.43.

Table 6.43: Period of the detected STVs in the X-ray flux sequence of OJ 287.

JD	Duration	Discrete Fourier Transform (P04)			Fast Fourier Transform (Python)			Lomb-Scargle Periodogram		
	(days)	Period (days)	Amplitude	S/N	Period (days)	Amplitude	S/N	Period (days)	Amplitude	S/N
2457673-2457917	244	80.27 ± 6.80	0.08 ± 0.04	1.8	78.60	0.22	16.3			
		44.45 ± 0.82	0.19 ± 0.04	4.5	43.67	0.16	8.5			

The shortest detected QPO has a timescale of 43-44 days.

Mrk 421

The short-term timescales of the detected QPOs in the X-ray flux sequence of Mrk 421 can be found in table 6.44.

Table 6.44: Period of the detected STVs in the X-ray flux sequence of Mrk 421.

JD	Duration	Discrete Fourier Transform (P04)			Fast Fourier Transform (Python)			Lomb-Scargle Periodogram		
	(days)	Period (days)	Amplitude	S/N	Period (days)	Amplitude	S/N	Period (days)	Amplitude	S/N
2457024-2457555	531	27.18 ± 0.12	8.71 ± 1.41	5.0	25.95	11.43	9.7			
		22.08 ± 0.11	6.28 ± 1.41	3.6	21.63	8.83	5.9			
		15.54 ± 0.06	5.74 ± 1.41	3.3	15.26	5.29	2.1			
2458090-2458294	204	58.40 ± 2.16	11.99 ± 2.80	3.42	60.60	13.2	5.4			
		25.17 ± 0.42	11.51 ± 2.80	3.3	23.31	11.21	3.9			
		11.91 ± 0.20	5.35 ± 2.80	1.5	11.22	9.06	2.6			
2459130-2459377	247	87.57 ± 2.30	12.28 ± 1.65	6.08	90.00	16.4	43.1			
		68.19 ± 1.06	16.16 ± 1.65	8.0	72.00	4.70	3.6			
		27.20 ± 0.21	12.69 ± 1.65	6.2	24.00	6.40	6.7			

The shortest detected QPO has a timescale of 11 days. A QPO with timescales of 24-27 days was detected in all the studied flux sequences.

3C 273

The short-term timescales of the detected QPOs in the X-ray flux sequence of 3C 273 can be found in table 6.45.

Table 6.45: Period of the detected STVs in the X-ray flux sequence of 3C 273.

JD	Duration	Discrete Fourier Transform (P04)			Fast Fourier Transform (Python)			Lomb-Scargle Periodogram		
	(days)	Period (days)	Amplitude	S/N	Period (days)	Amplitude	S/N	Period (days)	Amplitude	S/N
2455170-2457217	2047	78.97 ± 0.27	0.61 ± 0.10	4.9	78.60	0.51	4.4			
		38.97 ± 0.10	0.39 ± 0.10	3.2	39.30	0.29	2.1			

The shortest detected STV has a period of 38-39 days, with a possible harmonic of 78 days.

Mrk 501

The short-term timescales of the detected QPOs in the X-ray flux sequence of Mrk 501 can be found in table 6.46.

Table 6.46: Period of the detected STVs in the X-ray flux sequence of Mrk 501.

JD	Duration	Discrete Fourier Transform (P04)			Fast Fourier Transform (Python)			Lomb-Scargle Periodogram		
	(days)	Period (days)	Amplitude	S/N	Period (days)	Amplitude	S/N	Period (days)	Amplitude	S/N
2455623-2456138	515	83.06 ± 1.80	1.03 ± 0.25	3.3	82.50	1.5	10.1			
		7.21 ± 0.01	2.10 ± 0.25	6.7	7.67	1.0	4.7			
2456717-2456946	229	47.81 ± 0.56	2.82 ± 0.29	7.8	45.00	1.6	4.1			
		37.91 ± 0.48	2.07 ± 0.29	5.7	38.57	2.1	6.9			
		32.53 ± 0.25	2.85 ± 0.29	7.9	33.75	1.4	3.2			

The shortest detected QPO has a timescale of 7 days.

1ES 1959+650

The short-term timescales of the detected QPOs in the X-ray flux sequence of 1ES 1959+650 can be found in table 6.47.

Table 6.47: Period of the detected STVs in the X-ray flux sequence of 1ES 1959+650.

JD	Duration	Discrete Fourier Transform (P04)			Fast Fourier Transform (Python)			Lomb-Scargle Periodogram		
	(days)	Period (days)	Amplitude	S/N	Period (days)	Amplitude	S/N	Period (days)	Amplitude	S/N
2457045-2457797	752	54.21 ± 0.43	1.82 ± 0.36	4.0	51.60	1.63	2.6			
		22.30 ± 0.07	1.84 ± 0.36	4.1	22.43	2.85	7.8			
2457900-2459317	1417	73.16 ± 0.52	1.97 ± 0.49	3.2	75.00	2.42	4.1			
		50.39 ± 0.25	1.94 ± 0.49	3.2	50.00	2.65	4.9			
		39.12 ± 0.14	2.14 ± 0.49	3.5	39.47	2.26	3.6			
		25.83 ± 0.07	1.83 ± 0.49	3.0	22.73	2.88	5.8			

The shortest detected STV has a period of 22-25 days and was detected in both studied flux sequences. Also a QPO of 50-54 days was detected in both flux sequences.

BL Lac

The short-term timescales of the detected QPOs in the X-ray flux sequence of BL Lac can be found in table 6.48.

Table 6.48: Period of the detected STVs in the X-ray flux sequence of BL Lac.

JD	Duration	Discrete Fourier Transform (P04)			Fast Fourier Transform (Python)			Lomb-Scargle Periodogram		
	(days)	Period (days)	Amplitude	S/N	Period (days)	Amplitude	S/N	Period (days)	Amplitude	S/N
2456175-2457423	1248	72.42 ± 0.89	0.07 ± 0.03	2.2	76.71	0.07	16.8			
		51.70 ± 0.45	0.07 ± 0.03	2.3	51.14	0.05	9.6			
		36.39 ± 0.17	0.09 ± 0.03	2.9	35.80	0.06	12.0			
		30.15 ± 0.17	0.06 ± 0.03	2.0	29.03	0.05	9.3			

The shortest detected QPO has a timescale 29-30 days. STV of 35-36 days was detected, with a possible harmonic of 72-76 days.

CTA 102

The short-term timescales of the detected QPOs in the X-ray flux sequence of CTA 102 can be found in table 6.49.

Table 6.49: Period of the detected STVs in the X-ray flux sequence of CTA 102.

JD	Duration	Discrete Fourier Transform (P04)			Fast Fourier Transform (Python)			Lomb-Scargle Periodogram		
	(days)	Period (days)	Amplitude	S/N	Period (days)	Amplitude	S/N	Period (days)	Amplitude	S/N
2457560-2457970	410	53.96 ± 1.06	0.13 ± 0.03	3.0	100.50	0.2	16.36	96.0	0.4851	4.7059
		40.41 ± 0.63	0.12 ± 0.03	2.8	50.25	0.1	3.58			
					40.20	0.1	2.11			

The shortest detected STV has a period of 40 days.

3C 454.3

The short-term timescales of the detected QPOs in the X-ray flux sequence of 3C 454.3 can be found in table 6.50.

Table 6.50: Period of the detected STVs in the X-ray flux sequence of 3C 454.3.

JD	Duration	Discrete Fourier Transform (P04)			Fast Fourier Transform (Python)			Lomb-Scargle Periodogram		
	(days)	Period (days)	Amplitude	S/N	Period (days)	Amplitude	S/N	Period (days)	Amplitude	S/N
2454613-2455213	600	74.08 ± 0.48	0.54 ± 0.05	8.6	74.57	0.3	16.30			
		53.10 ± 0.32	0.42 ± 0.05	6.7	52.20	0.5	31.84			
		41.24 ± 0.15	0.55 ± 0.05	8.7	40.15	0.2	7.87			
		37.04 ± 0.14	0.45 ± 0.05	7.2	37.29	0.4	19.86			
		25.00 ± 0.08	0.38 ± 0.05	6.1	24.86	0.2	3.56			
		23.26 ± 0.06	0.43 ± 0.05	6.9	23.73	0.1	2.31			
		19.59 ± 0.09	0.20 ± 0.05	3.2	18.00	0.2	4.95			

The shortest detected STV has a timescale of 18-19 days, with a possible harmonic of 37 days.

The short-term timescales of the detected QPOs in X-rays of all the targets can be seen in Fig. 6.8.

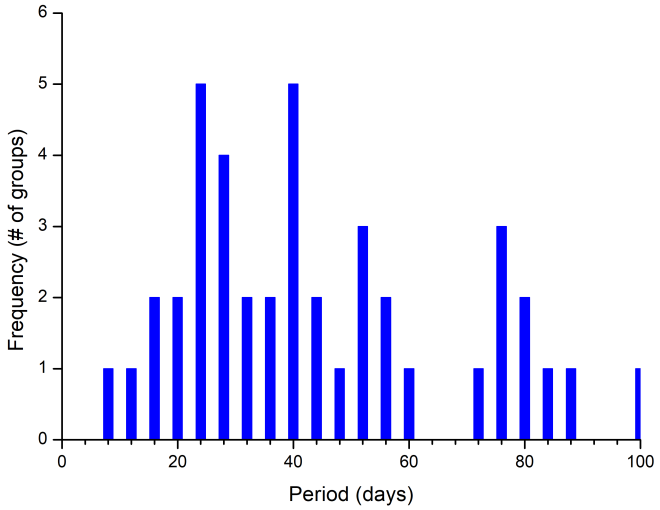

Figure 6.8: Frequency histogram of the detected period of STVs in X-rays, in 4-day bins.

The detected QPOs have timescales between 6 and 80 days, but most of the detected STVs are in the range of 8 to 20 minutes. QPOs of greater timescales have been detected but are less frequently detected.

6.6 Search for Long-Term Variability (LTV)

In the search for the Long-Term Variability non of the methods mentioned in paragraphs 3.1 and 3.2 were implemented. We searched for fluctuations and trends in the flux sequence of the targets (Fig. 6.2, 6.3, and 6.4).

1H 0323+342

There are no enough data to search for a trend in the flux sequence of the target.

PKS 0716+714

The flux sequence of PKS 0716+714 shows multiple flare events, but there are no enough data to search for LTV.

1ES 0836+71

The flux sequence of 1ES 0836+71 shows variability, but there are no enough data to search for LTV.

OJ 287

Two flare events can be detected in the flux sequence of OJ 287. The first flare event started in October 2016 and the flux returned to its mean value in May 2017. The second flare event started in April 2020 and ended in May 2020. Apart from these two events, no trend can be detected in the flux sequence of the target.

PKS 0954+658

There are no enough data to search for a trend in the flux sequence of the target.

Mrk 421

There is no significant trend in the flux sequence of Mrk 421, but multiple flare events can be detected.

3C 273

The flux sequence of 3C 273 shows variability, but no significant trend can be detected.

3C 279

3C 279 shows no significant trend, but a flare event in early 2017 can be detected.

PKS 1510-089

Multiple flare events can be seen in the flux sequence of PKS 1510-089, but no LTV can be detected.

PKS 1553+113

The flux sequence of PKS 1553+113 shows high variability, with multiple flare events. The target seems to be in a low state from mid-2015, after the end of a flare event, until mid-2017, and in a medium state in 2013, 2014, and from mid-2017 until 2021, when the observations end.

Mrk 501

Mrk 501 shows high variability in X-rays, with several flare events. In 2014 the targets is in a high state, in 2013, 2015, 2016 and 2021 the target is in a medium state, and from 2017 to 2020 the target is in a low state. Flare events are detected when the target is in medium or high state.

1ES 1959+650

The flux sequence of the target shows great variability. An upward trend can be seen from 2014 to early 2018, when a decrease of flux following a downward trend starts. The decrease of the flux continues until the end of observations in 2021.

BL Lac

The flux sequence of BL Lac shows no significant variability with the exception of some flare events in 2020 and 2021.

CTA 102

A flare event can be seen in the flux sequence of CTA 102 in late 2016. There are no enough data to search for LTV in X-rays for this target.

3C 454.3

3C 454.3 shows hugh variability during the observations, with an upward trend from 2013 to mid-2014. There are no enough data to search for LTV.

1ES 2344+514

In the flux sequence of 1ES 2344+514 no significant trend can be detected, but several flare events can be seen.

Chapter 7

Discussion and Conclusions

The search for QPOs in the signal of AGNs is a recent and active field of Astrophysics. This is due to the fact that periodic signals provide information about the processes that occur in the inner regions of an AGN, which most of the time cannot be observed directly. Moreover information about the structure of the AGN and the region of origin can be extracted, as shown in previous chapters.

Although a multi-wavelength approach is adopted in most of the recent studies, multi-wavelength studies that include data from optical wavelengths are quite rare. This is due to the lack of observations in these wavelengths. As referred in previous chapters, in order to search for QPOs a high-cadence intra-day and short-term observations are required, thus dedicated monitoring programms are needed. *BOSS Project* with continuous and long-run observations in optical wavelengths is one of the few programms that have enough optical data to search for QPOs in AGNs. From the detected timescales of QPOs and the physical parameters that were calculated using them we can extract information about the emitting region.

7.1 Study of the optical emitting region

By using the Eddington luminosity of the AGNs that was calculated in previous chapters based on the assumption that QPOs are a result of quasi-periodic injection of plasma into the jet due to instabilities that arise in the inner region of the accretion disk, we can calculate the upper limit of the luminosity of the accretion disk. The dividing line between BL Lac objects and FSRQs is calculated based on the relation between BLR luminosity and disk luminosity utilizing a Bayesian Information Criterion is given in terms of the disk luminosity from the equation 6.1 (Pei et al., 2022).

$$\frac{L_{disk}}{L_{Edd}} = 4.68 \times 10^{-3} \tag{6.1}$$

Thus we assume that for FSRQs the disk luminosity can be estimated as: $L_{disk} = 4.68 \times 10^{-3} L_{Edd}$, and for BL Lac objects as :$L_{disk} = 10^{-4} L_{Edd}$.

By using the mean magnitude, m, of each target we can calculate its luminosity. Assuming that the Hubble constant is $H_o = 70\ km/s$ we can calculate the distance, d, of each AGN and

the absolute magnitude, M, using equation 6.2.

$$M = m - 5 \cdot log\left(\frac{d}{10pc}\right) \tag{6.2}$$

The mean luminosity of the AGN can then be calculated using equation 6.3.

$$L = 10^{0.4\cdot(M_\odot - M)} L_\odot \tag{6.3}$$

where $M_\odot = 4.85$. By comparing the upper limit of the luminosity of the accretion disk, L_{disk}, with the calculated R-band luminosity of the AGN, L, we can examine whether the emission comes from the accretion disk or the jet of the AGN. If the computed luminosity of the accretion disk is greater than the R-band luminosity of the AGN then the emission can originate from the accretion disk, whereas if it is lesser the emission comes from the jet. The calculated parameters and the emitting region of each target can be seen in table 7.1. (The Eddington luminosity that was used is the one extracted from the marginally stable orbit of a non-rotating SMBH.)

Table 7.1: Calculated parameters of the AGNs and the emitting region.

Target	**Distance (Mpc)**	$\mathbf{m_{mean}}$	$\mathbf{M_{mean}}$	$\mathbf{L(10^{44}erg/s)}$	$\mathbf{L_{Edd}(10^{46}erg/s)}$	$\mathbf{L_{disk}(10^{44}erg/s)}$	**Emitting Region**
1H 0343+342	270.000	14.90	-30.83	2.66	30.10	14.10	Disk
PKS 0716+714	1328.571	13.40	-27.22	257.00	2.70	0.03	Jet
1ES 0836+71	9471.429	14.05	-22.26	10.70	1.82	0.02	Jet
OJ 287	1311.429	14.00	-26.59	144.00	6.67	0.07	Jet
Mrk 421	132.857	13.20	-22.42	3.09	1.23	0.01	Jet
3C 273	677.143	13.40	-25.75	66.70	80.70	0.81	Jet
3C 279	2297.143	15.40	-25.75	122.00	5.36	2.51	Jet
PKS 1553+113	1552.714	14.80	-26.14	95.40	6.08	0.06	Jet
Mrk 501	145.714	13.60	-22.22	122.00	5.36	0.03	Jet
1ES 1959+650	205.714	12.80	-23.77	10.70	1.82	0.02	Jet
BL Lac	295.714	13.50	-23.85	19.80	1.98	0.02	Jet
3C 454.3	3681.429	14.50	-28.33	716.00	9.99	0.10	Jet

From the above calculations, that are based on the detected timescales of QPOs, it is clear that the emission of blazars comes from the jet of the AGN, while in quasars (1H 0323+342 and 3C 279) the emission can come either from the jet or the accretion disk.

7.2 Comparative study of the detected QPOs for different optical activity states

AGNs and especially blazars show different states of activity in optical wavelengths. This can be easily seen in Fig. 4.2, 4.3, 4.4, and 4.5. The different states of activity are based on the optical luminosity of the AGN, thus when the AGN is more luminous and shows flaring activity it is in **high-state**, when no flare events are happening the AGN is in **low-state**, and when its shows intermediate activity it is in **intermediate state** (or **intermediate state**). Since the characterisation of the state of activity of the target is based in optical wavelengths, the activity states are called **optical activity states**.

Based on the observations we have in all energy bands, we can study the blazars by comparing their flux in different states of optical activity. This can be easily done with the use of their spectral energy distribution (SED) in the different states.

OJ 287

The SED of OJ 287 for different optical activity states can be seen in Fig. 7.1.

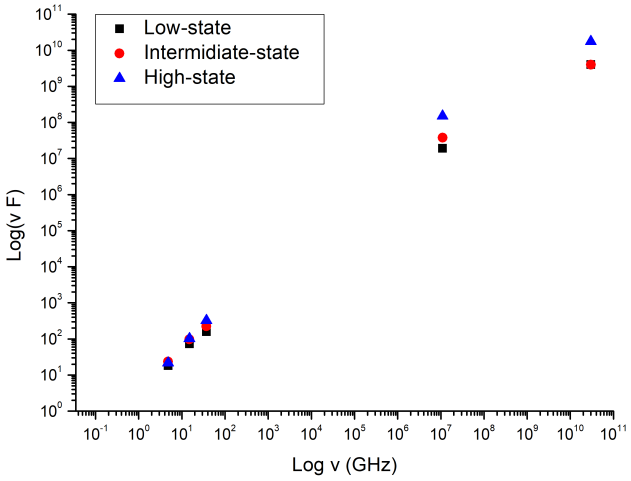

Figure 7.1: The SED of OJ287 during optical low, intermediate, and high state.

In low energies (4.8 and 15 GHz), the difference between the flux of each state of activity is small. In 15GHz, optical and X-rays, the flux difference is greater when the target is in high-state, than when the target is in intermediate and/or low state. Especially, in X-rays the flux is similar when the target is in optically intermediate and low state.

Based on the SED, it is clear that when OJ287 has high optical activity, the activity in the other wavelengths is also increased. On the other hand, when the targets is in intermediate and low optical state, the difference between the activity in the other energy bands is smaller.

Mrk 421

The SED of Mrk 421 for different optical activity states can be seen in Fig. 7.2.

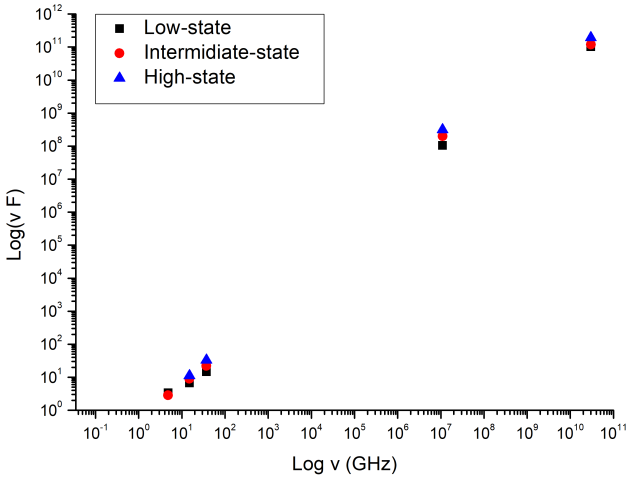

Figure 7.2: The SED of Mrk 421 during optical low, intermediate, and high state.

In 4.8 GHz, the flux is of the same scale for the different states of optical activity of Mrk 421. In the other wavelengths, the activity seems to follow the optical activity state of Mrk 421,

thus when the blazar is in high optical state, the activity is also increased in X-rays, 15 GHz and 37 GHz. On the other hand, the intermediate and low states of these energy bands the target has fluxes of similar scale, which means that the activity state is also similar.

Mrk 501

The SED of Mrk 501 for different optical activity states can be seen in Fig. 7.3.

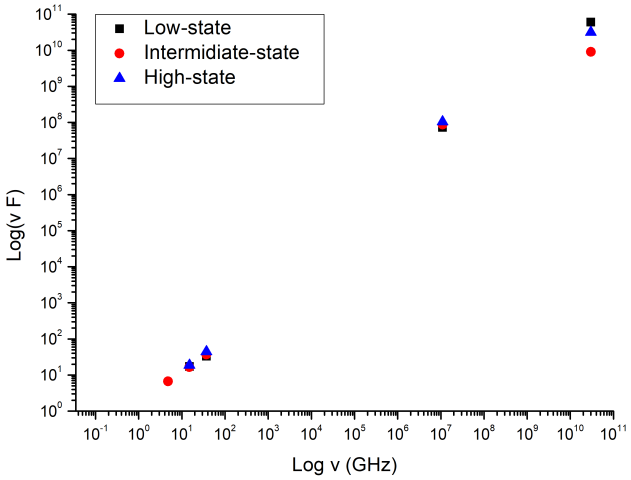

Figure 7.3: The SED of Mrk 501 during optical low, intermediate, and high state.

In radio, the flux is of the same scale for the different states of optical activity. On the other hand, the activity in X-rays differs from the one in optical. The flux is greater when the target is in low optical state, than when the target is in high and intermediate state of optical activity. This means that during the low activity state in optical, Mrk 501 was active in X-rays. On the other hand, during the intermediate state in optical the target showed low activity.

BL Lac

The SED of BL Lac for different optical activity states can be seen in Fig. 7.4.

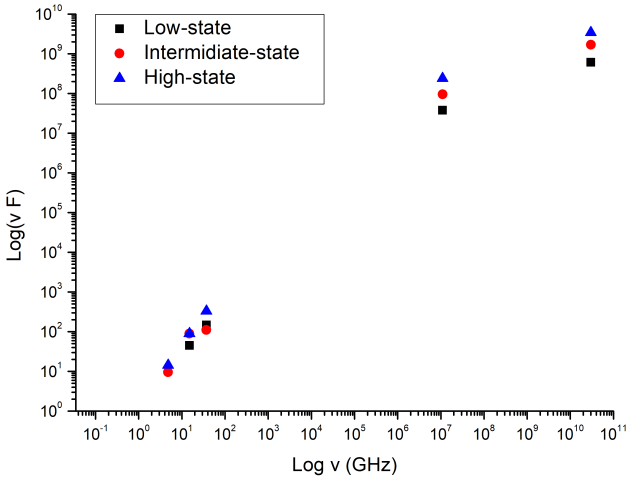

Figure 7.4: The SED of BL Lac during optical low, intermediate, and high state.

Based on the SED, it is clear that in X-rays and in 4.8 GHz the state of activity is similar with the optical activity state. In 15 GHz, the flux is of the same scale when the target is in high and intermediate optical state, which means that the activity level is similar. On the other hand, in 37 GHz the flux is smaller when BL Lac is in intermediate optical state, than when it is in intermediate state. Which means that it has increased activity in 37 GHz when the target is in low optical state.

In most cases there is a correlation between the activity in different wavelengths and the optical activity of the AGNs. This means that a connection exists between the different energy bands, leading to a dependent behavior.

The fluxes of the AGNs differ between the high, intermediate and low optical states as seen in the SEDs above. It is interesting to search if the different optical states of the targets lead to different timescales of QPOs for each state of activity. The comparison of the timescales detected during different states, whenever that was possible, is discussed next.

OJ 287

The histogram that shows the frequency of the detected timescales of QPOs in the optical light curves of OJ 287 during high and intermediate state can be seen in Fig. 7.5, that shows the QPOs grouped in 4-minute bins.

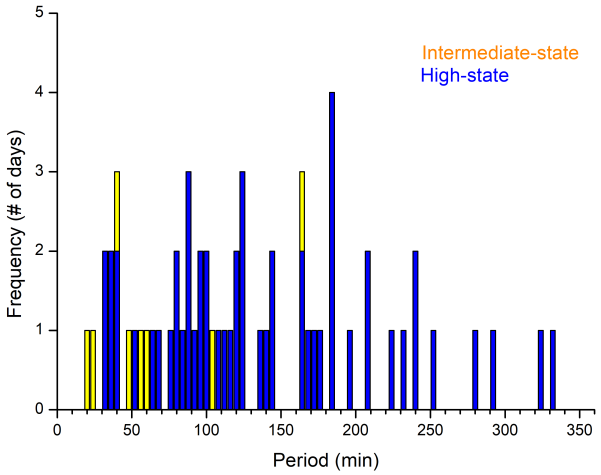

Figure 7.5: Frequency histogram of the detected period of IDVs of OJ287 during high and intermediate state, in 4-minute bins. The data used to create this histogram can be found in table F.3 in Appendix F.1.

By comparing the timescales that were detected during the target's high and intermediate state we see that the period of 120-123 minutes that was detected more frequently was during the high state. In most of the days that OJ 287 was searched for IDVs was in high-optical state, thus the detected timescales show greater range when the target is in high-state than when the target is in intermediate optical state.

Mrk 421

The histogram that shows the frequency of the detected timescales of QPOs in the optical light curves of Mrk 421 during low, intermediate and high state can be seen in Fig. 7.6, that shows the QPOs grouped in 3-minute bins.

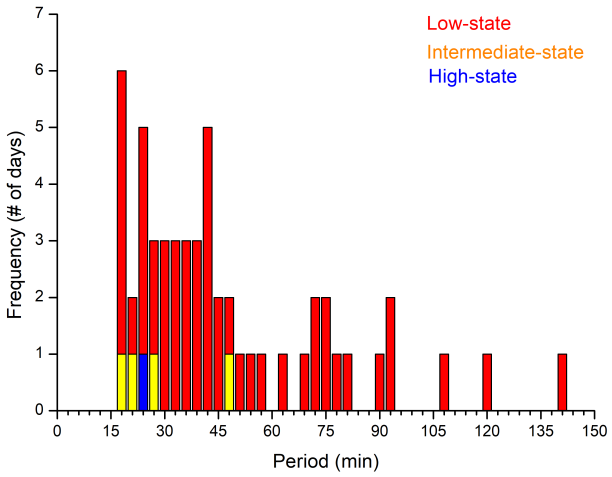

Figure 7.6: Frequency histogram of the detected period of IDVs in the optical light curves of Mrk 421 during different states of activity, in 3-minute bins. The data used to create this histogram can be found in table F.4 in Appendix F.1.

By comparing the timescales that were detected during the target's high, intermediate, and low state we see that during the high and intermediate state the QPOs have shorter timescales, while during low state the timescales of QPOs range from 16 to 143 minutes.

Mrk 421 was also studied in X-rays in order to detect QPOs of intra-day timescales. The histogram that shows the frequency of the detected timescales of QPOs in the X-ray flux sequences during the high, intermediate and low states of optical activity can be seen in Fig. 7.7, that shows the QPOs grouped in 3-minute bins.

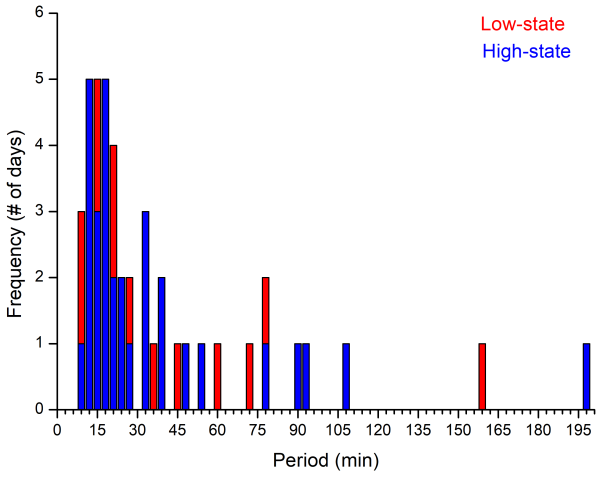

Figure 7.7: Frequency histogram of the detected period of IDVs of Mrk 421 in X-rays during different states of activity, in 3-minute bins. The data used to create this histogram can be found in table H.5 in Appendix H.1.

The timescales of QPOs during the high-state of optical activity tend to be shorter in comparison with the ones detected when the target was in low-state. Also in low state the detected QPOs are almost evenly spread across the range of 8 to 160 minutes, while during high-state the most timescales are in the range of 8 to 39 minutes.

Mrk 501

The histogram that shows the frequency of the detected timescales of QPOs in the X-ray flux sequences during high, intermediate and low state of optical activity can be seen in Fig. 7.8, that shows the QPOs grouped in 3-minute bins.

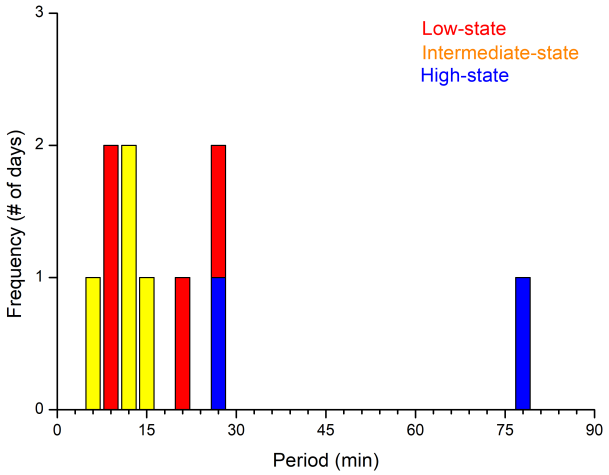

Figure 7.8: Frequency histogram of the detected period of IDVs of Mrk 501 in X-rays during different states of activity, in 3-minute bins. The data used to create this histogram can be found in table 6.27.

By comparing the timescales that were detected during the target's high, intermediate, and low state, we can see during the high state the QPOs have greater timescales, while during intermediate and low state the timescales of QPOs tend to be shorter.

BL Lac

The histogram that shows the frequency of the detected timescales of QPOs in the optical light curves of BL Lac during high and intermediate state of optical activity can be seen in Fig. 7.9, that shows the QPOs grouped in 3-minute bins.

The QPOs detected during the high-state of optical activity tend to have shorter timescales, in the range of 18 to 72 minutes. The detected timescales of QPOs during the intermediate state of activity are more evenly distributed across a range of 15 to 198 minutes.

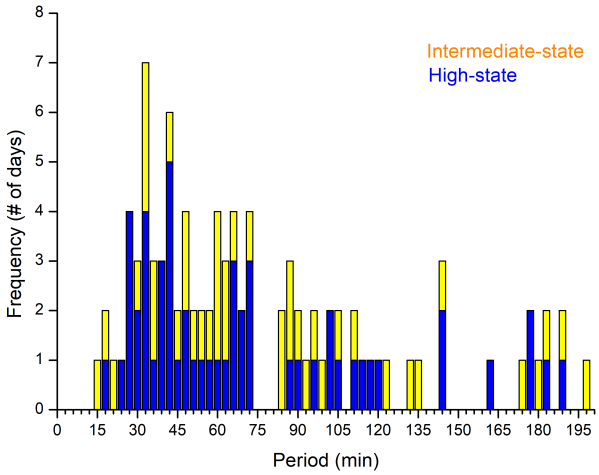

Figure 7.9: Frequency histogram of the detected period of IDVs of BL Lac in optical during different states of activity, in 3-minute bins. The data used to create this histogram can be found in table F.5 in Appendix F.1.

7.3 Comparative study of the detected timescales of QPOs in different wavelengths

A comparative study of the detected timescales of QPOs from all wavelengths is needed in order to better understand the processes that occur in AGNs. The comparison of the detected timescales of QPOs in different wavelengths can provide information on whether the QPOs arise from the same region of the AGN or they originate from different regions for different wavelengths.

The intra-day timescales of QPOs that were detected in the optical light-curves and the X-ray flux sequences of all the targets can be seen in the histograms of Fig. 7.10.

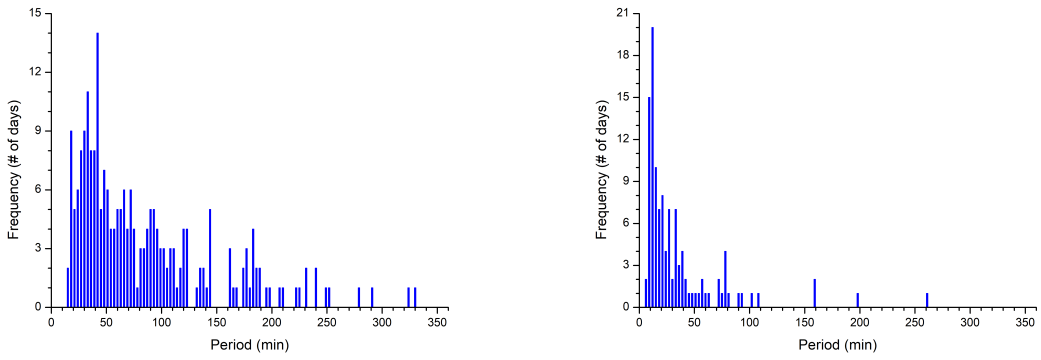

Figure 7.10: Frequency histograms of the detected period of IDVs of all targets in optical (left) and X-rays (right), in 3-minute bins. The data used to create this histogram can be found in Appendix F.1 and H.1, accordingly.

Based on these histograms, it is clear that the timescales of QPOs in X-rays are shorter that the ones detected in optical wavelengths. It should be pointed out though that due to the limit that was set in the search of QPOs in optical wavelengths, due to the duration of our observations, periods lower than 15 minutes cannot be detected in optical wavelengths. Also a different

number of light curves were studied in each wavelengths, which is the reason that in optical the QPOs range between larger scales unlike the QPOs detected in X-rays.

In both wavelengths it can be seen that most QPOs have timescales shorter than a hour. This means that extremely fast phenomena occur near the SMBH.

QPOs of short-term timescales were also studied in 5 energy bands. The detected timescales of QPOs can be seen in the histograms of Fig. 7.11.

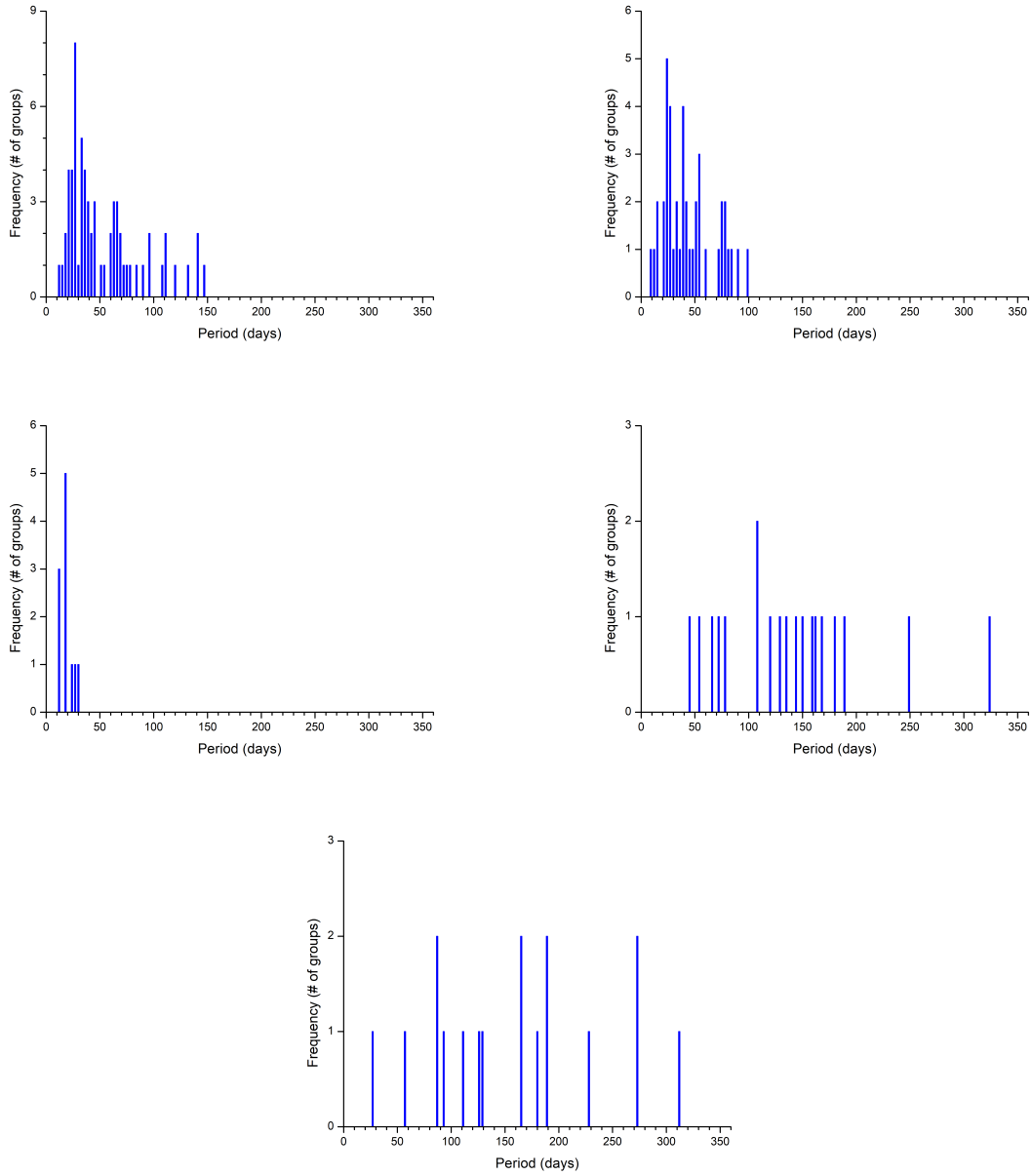

Figure 7.11: Frequency histograms of the detected period of STVs of all targets in optical (upper-left), X-rays (upper-right), 4.8 GHz (middle-left), 15 GHz (middle-right), and 37 GHz (lower), in 3-minute bins.

In optical and X-rays the timescales of 20-30 days are dominant. Also shorter timescales can be seen in the histogram of the detected QPOs in 4.8 GHz. In 15 GHz and 37 GHz, the QPOs are almost evenly distributed in a range of 30 to 360 days.

The detection of QPOs of greater timescales in optical and X-rays is difficult due to the

duration of the observations and the reliability limit we set in order to search for periods.

In order to have a better understanding about the correlation of the timescales between different wavelengths a comparison of the detected QPOs of each target in different energy bands is needed. The comparison was done whenever it was possible based on our data.

PKS 0716+714

QPOs with timescales of 49-51 minutes were detected in the X-ray flux sequences of PKS 0716+714. IDVs of similar timescales, with periods of 48-51 minutes were detected in the optical light curves of the target. The fact that QPOs of the same timescale were detected in both X-rays and optical wavelengths is a strong evidence that the periodic signal originates from the same region near the SMBH.

OJ 287

In the 4.8GHz radio curves of OJ 287 QPOs with short-term timescales of 16 days and 26-28 days were detected. In 15 GHz, dominant quasi periodic signals of 108 days and 129 days were found, while in the radio curves of 37 GHz STVs of 91 days, 110 days and 126-128 days were detected. In the optical light curves QPOs with timescales of 36-39 days were found and in X-ray flux sequences quasi-periodic signals of 43-44 days were detected. The QPOs detected in the radio curves of 15 and 37 GHz are of the same timescales, thus they probably originate from the same region. Respectively the STVs that were detected in the optical light curves, the 4.8 GHz radio curves and the X-ray flux sequences are of the similar scale, thus there is strong evidence that they arise from the same region.

Mrk 421

In the intra-day X-ray flux sequences of Mrk 421 a dominant quasi periodic signal with timescale of 12-16 minutes was detected. IDVs of the same scale (15-18 minutes) were also discovered in the intra-day optical light curves of the target. This fact provides strong evidence that the fluctuations arise from the same region near the SMBH. A more detailed study of the detected timescales of QPOs in X-rays and optical wavelengths was also done by comparing the detected timescales of QPOs of similar Julian dates.

- On 2456368 and 2456369, in X-rays QPOs with timescales of 14 minutes, 33-34 minutes and 77-78 minutes were found, while in optical light curves an IDV of 24 minutes was detected.
- On 2457785 and 2457799, in the X-ray flux sequence quasi-periodic signal of 18-19 minutes was discovered, and in optical light curves QPOs with timescales of 19 minutes and 25-27 minutes.
- On 2458136 and 2458137, in the X-ray flux sequence QPOs of 14 minutes, 16 minutes, 23-24 minutes and 38-40 minutes were detected. In the optical light curve, QPOs with timescales of 22-23 minutes, 25 minutes, 35-36 minutes and 41 minutes were found.

In most cases, the detected QPOs in optical and X-rays are of the same scale, providing a strong evidence that they originate from the same region.

In the radio curves of 4.8 GHz QPOs of 11 days, 17 days, 18 days and 23 days were detected. In 15 GHz, quasi-periodic signals of 71 days and 77 days were discovered, and in 37 GHz STVs of 55 days and 128 days were found. In the X-ray flux sequence, QPOs with timescales of 24-27 days were detected. Lastly in optical light curves quasi-periodic signals of 24-27 days were discovered. In optical, X-rays and 4.8 GHz, QPOs are of the same scale. This shows that there

is a correlation between these energy bands and provide strong evidence that the QPOs originate from the same region.

Comparing the results of QPOs of intra-day and short-term timescales provide strong evidence that QPOs possibly originate the same region.

Mrk 501

In the radio light curve of 4.8 GHz of Mrk 501, QPOs with short-term timescales of 10 days and 29 days were discovered. In 15 GHz, a QPO of 53-54 days was detected, and in 37 GHz, STVs of 25-27 days were found. In the X-ray flux sequence of Mrk 501, QPOs of 36 days were discovered. Lastly in optical, STVs with periods of 32-33 days were discovered. The detected QPOs in most energy bands are of the same scale (25-36 minutes) thus there is a strong evidence that the fluctuations arise from the same region of the accretion disk.

BL Lac

In order to search for intra-day quasi-periodic signal in the X-ray sequence of BL Lac data before 2013 were used. Thus the comparison of QPOs of intra-day timescales cannot provide solid data for the origin of the fluctuation. On the other hand, conclusions can be extracted from the timescales of short-term QPOs.

In 4.8 GHz STVs of 11, 17, 18 and 23 days were detected. In the radio curve of 15 GHz, a quasi-periodic signal of 43, 66 and 247 days were detected. In 37 GHz, periods of 86 days, which can be a possible harmonic of 43 days, and 182 days were found. In optical, QPOs of 18-21 days and 24-27 days were detected, and in the X-ray flux sequence STVs of 29-30 days were discovered. In optical and X-rays, a QPO of the same scale was detected, thus possibly the fluctuations in these wavelengths arise from the same region. In optical and 4.8 GHz the detected quasi-periodic signal are of the same timescale thus providing strong evidence that QPOs detected in these energy bands originate from the same region.

In most of the targets, there is strong evidence that the fluctuations possibly arise from the same region, thus the model that suggests that QPOs originate from instabilities in the inner region of the accretion disk and propagate along the jet is most likely confirmed based on our study, since the QPOs are detected with 99% confidence.

7.4 Conclusions

In the frame of this thesis, we studied AGNs using data from 5 different wavelengths (optical (R-band), X-rays 4.8 GHz, 15 GHz, and 37 GHz). We searched for QPOs of intra-day and short-term timescales in all the studied wavelengths by applying 3 different methods of time-series analysis, the *Discrete Fourier Transform*, the *Fast Fourier Transform* and the *Lomb-Scargle Periodogram*, and a threshold of 99% confidence in the detection of the timescales was set. QPOs of intra-day and short-term timescales were detected in most targets. The detected intra-day and short term timescales of QPOs of all the targets in all the frequencies can be seen in Fig. 7.10 and 7.11 accordingly. In many targets, there are dominant timescales of QPOs that appear in different cycles. The timescales detected less frequently may be due to stochastic processes, but dominant QPOs most likely arise from the same region.

Based on our data, during different states of optical activity, the detected QPOs have different timescales, but dominant timescales are detected independently of the activity state of

the AGN. In most cases, when the AGN is in high-state, QPOs tend to have shorter intra-day timescales, in the scale of several minutes, whereas during low and intermediate state the QPOs are almost equally distributed from some minutes to several hours. This can possibly mean that during the low and intermediate state of activity, the fluctuations can arise due to stochastic processes, but since dominant timescales are detected, the related to them fluctuations probably arise from instabilities in the accretion disk in orbits that are stable regardless of the activity state of the AGN.

The comparison between the SEDs of the AGNs during different states of optical activity, based on our data in different wavelengths, showed that in most cases the activity state is the same across the energy bands that were studied. One possible scenario that can explain this behavior is that the radiation of different energy bands originates from the same region and then propagates to the emission region, which is in agreement with the model that suggests that the luminosity of QPOs is due to the accretion of matter from the accretion disk into the SMBH.

Although there is yet no theoretical model that can sufficiently explain the detection of quasi-periodic signals from AGNs, time-domain analysis of multi-wavelength light curves of AGNs is a useful tool in the better understanding of the processes that occur in the inner regions of AGNs, under certain assumptions. Especially in the case of blazars, where direct observation of the inner regions is difficult, QPOs can provide information about the parameters of the regions close to the SMBH.

One of the parameters of the inner regions of AGNs that can be extracted from the detected QPOs is the mass of the SMBH, if we assume that the quasi-periodic signals originate from the inner region of the accretion disk and then propagate along the jet. The mass of AGNs is usually estimated by stellar and gas kinematics and reverberation mapping that are reliable methods but require high spatial resolution spectroscopy. Blazars have almost featureless continuum, thus these methods have several constraints. On the other hand, QPOs can be a useful tool in the estimation of the mass of the SMBH of blazars, under certain assumptions, as shown in this study. The lower limit of the mass of the SMBH based on the detected timescales is in agreement with the values in literature. This also provides strong evidence that our assumption that QPOs originate from the inner regions of the accretion disk is most likely correct. The calculated lower limit of the mass and the value from literature can be seen in Fig. 7.12.

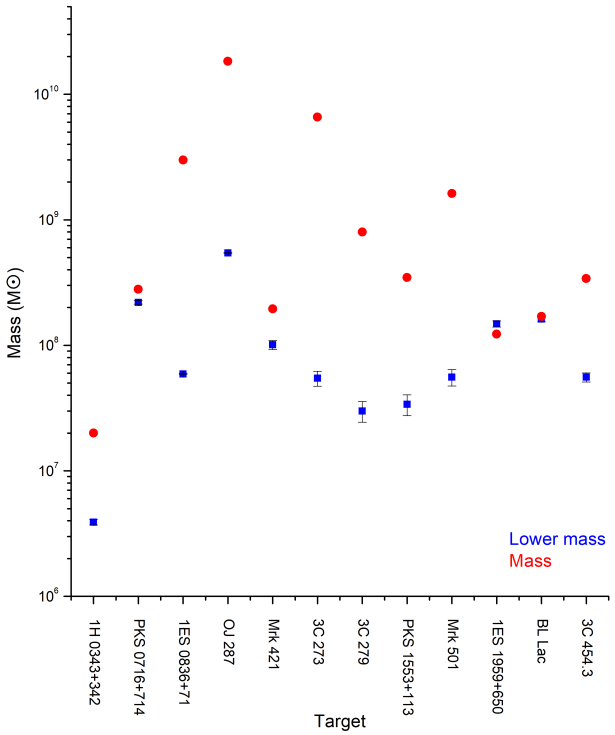

Figure 7.12: Graphic display of the calculated lower limit (blue) of mass and the value from literature (red).

A histogram that shows the calculated masses of the AGNs can be seen in Fig. 7.13.

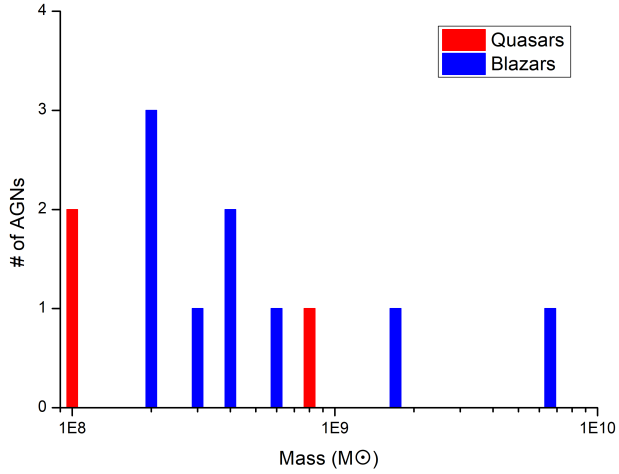

Figure 7.13: Frequency histogram of the masses of AGNs calculated from the detected QPOs.

From the above histogram it is clear that the SMBHs of quasars, in most cases, tend to have smaller masses than the ones of blazars. Also most of the SMBH masses are of the order of $10^8 M_\odot$. Based on the mass of the SMBH, the Eddington luminosity and the upper limit of the accretion rate can be calculated. From the upper limit of luminosity, we can calculate the upper limit of the luminosity of the accretion disk, using a certain model about the disk luminosity. By comparing the results of the disk luminosity, with the luminosity of the AGN in optical

wavelengths, the emitting region can be found. As expected, the emission of blazars comes from the jet.

Multi-wavelength time-domain analysis of AGNs can also help reveal the nature of QPOs, especially when a large amount of blazars is studied. By comparing the timescales of QPOs of different energies we can spread light in the origins of QPOs. In particular, we can study the region where QPOs originate for different wavelengths. Our analysis showed that the QPOs detected with at least 99% confidence, in most cases, have similar intra-day and short-term timescales across the wavelengths that we studied. Thus QPOs of intra-day and short-term timescales most likely originate from the same region in most cases. This is in accordance with the model which suggests that QPOs arise from instabilities in the accretion disk that quasi-periodically inject plasma in the jet of the AGN. Moreover, this possibly solidifies the assumptions made in order to calculate the parameters of the inner region of the AGNs.

Throughout our study there are strong evidence that QPOs originate from the accretion disk and then propagate through the jet due to quasi-periodic injection of plasma. Directly related evidence to the detected QPOs, which have a high level of confidence due to the threshold we set, are the existence of dominant timescales in different cycles and the correlation between the timescales of different wavelengths. Also evidence that are indirectly related to the QPOs are the parameters of the SMBH, which were calculated based on the assumption that QPOs originate from the inner region of the accretion disk, and are in symphony with the literature, thus proving that our assumption is likely correct.

Summarising, quasi-periodic oscillations are a great tool in the study of AGNs and especially blazars. The detected QPOs can set constraints in the physical parameters of the SMBH, under certain assumptions, and also spread light in the processes that occur in the inner regions of the AGNs. The comparison of the detected timescales in different wavelengths can also shed light to the mechanism that lead to quasi-periodic signals in the light curves of AGNs. In order to better understand the nature of AGNs time-domain multi-wavelength studies of large samples of AGNs should be done.

Bibliography

Abazajian K. N., et al., 2009, ApJ, 182, 543

Abdo A. A., et al., 2010, ApJ, 721, 1425

Abramowicz M. A., Nobili L., 1982, Nature, 300, 506

Ackermann M., et al., 2015, ApJ, 813, L41

Acton L. W., 1964, Nature, 204, 64

Adams T. F., Weedman D. W., 1975, ApJ, 199, 19

Agarwal A., et al., 2019, MNRAS, 488, 4093

Ait Benkhali F., Hofmann W., Rieger F. M., Chakraborty N., 2020, A&A, 634, A120

Aleksić J., et al., 2014, A&A, 569, A46

Aliu E., et al., 2013, ApJ, 779, 88

Anderhub H., et al., 2009, ApJ, 706, L27

Angel J. R. P., Stockman H. S., 1980, ARA&A, 18, 321

Antonucci R., 1993, ARA&A, 31, 473

Bañados E., et al., 2018, Nature, 553, 473

Bachev R., et al., 2017, MNRAS, 471, 2216

Beckmann V., Gehrels N., Shrader C. R., Soldi S., 2006, ApJ, 638, 642

Begelman M. C., Blandford R. D., Rees M. J., 1984, Reviews of Modern Physics, 56, 255

Berton M., Braito V., Mathur S., Foschini L., Piconcelli E., Chen S., Pogge R. W., 2019, A&A, 632, A120

Bessell M. S., 1990, PASP, 102, 1181

Bhatta G., 2017, ApJ, 847, 7

Bhatta G., 2019, MNRAS, 487, 3990

Bhatta G., Dhital N., 2020, , 891, 120

Bhatta G., et al., 2016, ApJ, 832, 47

Bicknell G. V., 1985, PASA, 6, 130

Blandford R. D., Rees M. J., 1978, in Wolfe A. M., ed., BL Lac Objects. pp 328–341

Blandford R. D., Znajek R. L., 1977, MNRAS, 179, 433

Boller T., Balestra I., Kollatschny W., 2007, A&A, 465, 87

Bonnoli G., Ghisellini G., Foschini L., Tavecchio F., Ghirlanda G., 2011, MNRAS, 410, 368

Böttcher M., 1997, PhD thesis, University of Bonn, Germany

Böttcher M., Dermer C. D., 2002, ApJ, 564, 86

Böttcher M., et al., 2007, ApJ, 670, 968

Britzen S., Witzel A., Krichbaum T. P., Campbell R. M., Wagner S. J., Qian S. J., 2000, A&A, 360, 65

Burbidge E. M., Rosenberg F. D., 1965, ApJ, 142, 1673

Calcidese P., Raiteri C. M., Villata M., Carnerero M. I., Acosta-Pulido J. A., GASP-WEBT Collaboration 2016, The Astronomer's Telegram, 9868, 1

Camenzind M., Krockenberger M., 1992, A&A, 255, 59

Chernyakova M., et al., 2019, A&A, 631, A177

Chiu H.-Y., 1964, Physics Today, 17, 21

Ciprini S., Dutka M., 2011, The Astronomer's Telegram, 3831, 1

Ciprini S., Fermi Large Area Telescope Collaboration 2015, The Astronomer's Telegram, 7870, 1

Cohen R. D., Rudy R. J., Puetter R. C., Ake T. B., Foltz C. B., 1986, ApJ, 311, 135

D'Ammando F., et al., 2011, A&A, 529, A145

D'Ammando F., et al., 2013, MNRAS, 431, 2481

Dai H., Xie G. Z., Zhou S. B., Li H. Z., Chen L. E., Ma L., 2007, AJ, 133, 2187

Dai B. Z., et al., 2009, MNRAS, 392, 1181

Dermer C. D., Schlickeiser R., 1993, ApJ, 416, 458

Espaillat C., Bregman J., Hughes P., Lloyd-Davies E., 2008a, ApJ, 679, 182

Espaillat C., Bregman J., Hughes P., Lloyd-Davies E., 2008b, ApJ, 679, 182

Fan J. H., Peng Q. S., Tao J., Qian B. C., Shen Z. Q., 2009, AJ, 138, 1428

Fan J. H., Kurtanidze O., Liu Y., Richter G. M., Chanishvili R., Yuan Y. H., 2014, ApJ, 213, 26

Fanaroff B. L., Riley J. M., 1974, MNRAS, 167, 31P

Filippenko A. V., 1986, in Swarup G., Kapahi V. K., eds, Vol. 119, Quasars. p. 289

Foschini L., et al., 2006, , 455, 871

Foschini L., Bonnoli G., Ghisellini G., Tagliaferri G., Tavecchio F., Stamerra A., 2013, A&A, 555, A138

Fugmann W., 1989, A&A, 222, 45

Fukumura K., Kazanas D., 2008, ApJ, 679, 1413

Gaur H., et al., 2019, MNRAS, 484, 5633

Gazeas K., 2016, in Revista Mexicana de Astronomia y Astrofisica Conference Series. pp 22–23

Gazeas K., Bhatta G., Max-Moerbeck W., Petropoulou M., Hovatta T., Vasilopoulos G., Mastichiadis A., 2015. Hel.A.S Conference Series

Ghisellini G., Maraschi L., 1989, ApJ, 340, 181

Ghisellini G., Celotti A., Fossati G., Maraschi L., Comastri A., 1998, MNRAS, 301, 451

Ghisellini G., et al., 2010, MNRAS, 405, 387

Gierliński M., Middleton M., Ward M., Done C., 2008, Nature, 455, 369

Giommi P., Padovani P., 1994, MNRAS, 268, L51

Giommi P., Ansari S. G., Micol A., 1995, A&A, 109, 267

Giommi P., Padovani P., Perlman E., 2000, MNRAS, 317, 743

Guise E., et al., 2022, MNRAS, 510, 3145

Gupta A. C., 2014, Journal of Astrophysics and Astronomy, 35, 307

Gupta A. C., Banerjee D. P. K., Ashok N. M., Joshi U. C., 2004, A&A, 422, 505

Gupta A. C., Fan J. H., Bai J. M., Wagner S. J., 2008, AJ, 135, 1384

Gupta A. C., Srivastava A. K., Wiita P. J., 2009, ApJ, 690, 216

Gupta S. P., Pandey U. S., Singh K., Rani B., Pan J., Fan J. H., Gupta A. C., 2012, NewA, 17, 8

H. E. S. S. Collaboration et al., 2012, A&A, 539, A149

Hawkins M. R. S., 1978, MNRAS, 182, 361

Hayashida M., 2008, PhD thesis, LMU Munich, Germany

Healey S. E., et al., 2008, ApJ, 175, 97

Hermsen W., et al., 1977, Nature, 269, 494

Hocke K., Kämpfer N., 2009, ACP, 9, 4197

Hovatta T., Lehto H. J., Tornikoski M., 2008, A&A, 488, 897

Hovatta T., et al., 2015, MNRAS, 448, 3121

Hroch F., 1998, in Dusek J., ed., 20th Stellar Conference of the Czech and Slovak Astronomical Institutes. p. 30

Huang S., Yin H., Hu S., Chen X., Jiang Y., Alexeeva S., Wang Y., 2021, ApJ, 922, 222

Impey C. D., Lawrence C. R., Tapia S., 1991, ApJ, 375, 46

Jang M., Miller H. R., 1997, AJ, 114, 565

Jones D. H., et al., 2009, MNRAS, 399, 683

Kallunki J., Lavonen N., Järvelä E., Uunila M., 2012, Baltic Astronomy, 21, 255

Kaspi S., Maoz D., Netzer H., Peterson B. M., Vestergaard M., Jannuzi B. T., 2005, ApJ, 629, 61

Keel W. C., 1980, AJ, 85, 198

Kellermann K. I., Sramek R., Schmidt M., Shaffer D. B., Green R., 1989, AJ, 98, 1195

Khachikian E. Y., Weedman D. W., 1974, ApJ, 192, 581

Kollatschny W., 2003, A&A, 412, L61

Kollatschny W., Welsh W. F., 2001, in Cantó J., Rodríguez L. F., eds, Revista Mexicana de Astronomia y Astrofisica Conference Series Vol. 10, Revista Mexicana de Astronomia y Astrofisica Conference Series. pp 79–82

Kühr H., Pauliny-Toth I. I. K., Witzel A., Schmidt J., 1981, AJ, 86, 854

Laine S., et al., 2020, ApJL, 894, L1

Landt H., et al., 2017, MNRAS, 464, 2565

Larionov V. M., et al., 2016, MNRAS, 461, 3047

Larionov V. M., et al., 2020, , 492, 3829

Lehto H. J., Valtonen M. J., 1996, ApJ, 460, 207

Lenz P., Breger M., 2005, Communications in Asteroseismology, 146, 53

Li H. Z., Jiang Y. G., Guo D. F., Chen X., Yi T. F., 2016, PASP, 128, 074101

Li X.-P., Luo Y.-H., Yang H.-Y., Yang C., Cai Y., Yang H.-T., 2017, ApJ, 847, 8

Li X.-P., et al., 2018, Journal of Astrophysics and Astronomy, 39, 30

Li X.-P., Zhao L., Yan Y., Wang L.-S., Yang H.-T., Cai Y., Luo Y.-H., 2021, Journal of Astrophysics and Astronomy, 42, 92

Li H.-Z., et al., 2022, PASP, 134, 044101

Liang E. W., Liu H. T., 2003, MNRAS, 340, 632

Lindfors E. J., et al., 2016, A&A, 593, A98

Lister M. L., Homan D. C., 2005, AJ, 130, 1389

Liu J., Liu X., 2015, Ap&SS, 357, 165

Liu F. K., Zhao G., Wu X.-B., 2006, ApJ, 650, 749

Liu X., et al., 2017, MNRAS, 469, 2457

Liu X., Wang X., Chang N., Liu J., Cui L., Yang X., Krichbaum T. P., 2021, Universe, 7, 15

Lomb N. R., 1976, Ap&SS, 39, 447

Longair M. S., 2011, High Energy Astrophysics, 3 edn. Cambridge University Press, doi:10.1017/CBO9780511778346

Lovell J. E. J., et al., 2008, ApJ, 689, 108

Lynden-Bell D., 1969, Nature, 223, 690

Ma L., Xie G. Z., Yi T. F., Zhou S. B., Li K. H., Zhang X., Dai H., 2010, Ap&SS, 327, 35

Maiolino R., Rieke G. H., 1995, ApJ, 454, 95

Mangalam A. V., Wiita P. J., 1993a, ApJ, 406, 420

Mangalam A. V., Wiita P. J., 1993b, ApJ, 406, 420

Mannheim K., 1993, A&A, 269, 67

Mao L. S., 2011, NewA, 16, 503

Mao L.-S., Xie G.-Z., Bai J.-M., Liu H.-T., 2005, ChJAA, 5, 471

Maraschi L., Ghisellini G., Celotti A., 1992, ApJ, 397, L5

Marscher A. P., et al., 2010, ApJ, 710, L126

McElroy R. E., et al., 2016, A&A, 593, L8

Miller H. R., Green R. F., 1983, in Bulletin of the American Astronomical Society. p. 957

Miniutti G., et al., 2019, Nature, 573, 381

Mücke A., Protheroe R. J., 2001, Astroparticle Physics, 15, 121

Nass P., Bade N., Kollgaard R. I., Laurent-Muehleisen S. A., Reimers D., Voges W., 1996, in Zimmermann H. U., Trümper J., Yorke H., eds, Roentgenstrahlung from the Universe. pp 487–488

Nilsson K., Pursimo T., Sillanpää A., Takalo L. O., Lindfors E., 2008, A&A, 487, L29

Nilsson K., Pursimo T., Villforth C., Lindfors E., Takalo L. O., 2009, A&A, 505, 601

Osterbrock D. E., Mathews W. G., 1986, ARA&A, 24, 171

Padovani P., Giommi P., 1995, ApJ, 444, 567

Paliya Vaidehi S., 2015, ApJ, 804, 74

Paliya V. S., Sahayanathan S., Parker M. L., Fabian A. C., Stalin C. S., Anjum A., Pandey S. B., 2014, ApJ, 789, 143

Paltani S., Türler M., 2005, A&A, 435, 811

Pei Z., Fan J., Yang J., Huang D., Li Z., 2022, ApJ, 925, 97

Penston M. V., Cannon R. D., 1969, Commmunications of the Konkoly Observatory Hungary, 65, 485

Perkins D. H., 2009, Particle astrophysics, 2nd ed. edn. Oxford University Press

Perlman E. S., et al., 1996, ApJ, 104, 251

Peterson B. M., 1993, PASP, 105, 247

Peterson B. M., 1997, An Introduction to Active Galactic Nuclei. Cambridge University Press, doi:10.1017/CBO9781139170901

Pihajoki P., Valtonen M., Ciprini S., 2013, MNRAS, 434, 3122

Raiteri C. M., Ghisellini G., Villata M., de Francesco G., Lanteri L., Chiaberge M., Peila A., Antico G., 1998, A&A, 127, 445

Raiteri C. M., et al., 2001, A&A, 377, 396

Raiteri C. M., et al., 2003, A&A, 402, 151

Raiteri C. M., Acosta Pulido J. A., Villata M., Carnerero M. I., Romano P., Vercellone S., 2020, MNRAS, 493, 2793

Richards J. L., et al., 2011, ApJS, 194, 29

Rieger F. M., Mannheim K., 2000, A&A, 359, 948

Rödig C., Burkart T., Elbracht O., Spanier F., 2009, A&A, 501, 925

Rybicki G. B., Lightman A. P., 1986, Radiative Processes in Astrophysics

Safna P. Z., Stalin C. S., Rakshit S., Mathew B., 2020, MNRAS, 498, 3578

Sandrinelli A., Covino S., Dotti M., Treves A., 2016, AJ, 151, 54

Sandrinelli A., et al., 2017, A&A, 600, A132

Sarkar A., Gupta A. C., Chitnis V. R., Wiita P. J., 2021, MNRAS, 501, 50

Scargle J. D., 1982, ApJ, 263, 835

Schmidt M., 1965, ApJ, 141, 1295

Schmitt J. L., 1968, Nature, 218, 663

Seyfert C. K., 1943, ApJ, 97, 28

Shen Y., Loeb A., 2010, ApJ, 725, 249

Shu F., 1982, The Physical Universe: An Introduction to Astronomy. Series of books in astronomy, University Science Books, https://books.google.gr/books?id=NfhrH6FS7TYC

Sillanpää A., Haarala S., Valtonen M. J., Sundelius B., Byrd G. G., 1988, ApJ, 325, 628

Sitko M. L., Junkkarinen V. T., 1985, PASP, 97, 1158

Smith H. J., Hoffleit D., 1963, Nature, 198, 650

Spiridonova O. I., Vlasyuk V. V., Moskvitin A. S., Bychkova V. S., 2015, The Astronomer's Telegram, 7057, 1

Stickel M., Fried J. W., Kuehr H., 1993, A&A, 98, 393

Strauss M. A., Huchra J. P., Davis M., Yahil A., Fisher K. B., Tonry J., 1992, ApJ, 83, 29

Stroh M. C., Falcone A. D., 2013, ApJS, 207, 28

Syunyaev R. A., Shakura N. I., 1977, Soviet Astronomy Letters, 3, 138

Taylor A. R., Gregory P. C., 1982, ApJ, 255, 210

Taylor A. R., Kenny H. T., Spencer R. E., Tzioumis A., 1992, ApJ, 395, 268

Titarchuk L., Seifina E., 2017, A&A, 602, A113

Ulrich M. H., 1978, ApJ, 222, L3

Urry C. M., Mushotzky R. F., 1982, ApJ, 253, 38

Urry C. M., Padovani P., 1995, PASP, 107, 803

Valtaoja E., Terasranta H., Urpo S., Nesterov N. S., Lainela M., Valtonen M., 1992, A&A, 254, 80

Villata M., et al., 1997, A&A, 121, 119

Villata M., et al., 2004, A&A, 421, 103

Villata M., et al., 2008, A&A, 481, L79

Wagner S. J., Witzel A., 1995, ARA&A, 33, 163

Wagner S. J., et al., 1993, A&A, 271, 344

Wagner S. J., et al., 1995, A&A, 298, 688

Wang J.-Y., An T., Baan W. A., Lu X.-L., 2014, MNRAS, 443, 58

Wang Y., Zhu S., Xue Y., Gu M., Weng S., Le H. A. N., 2019, ApJ, 885, 8

Webb J. R., Smith A. G., Leacock R. J., Fitzgibbons G. L., Gombola P. P., Shepherd D. W., 1988, AJ, 95, 374

Weedman D. W., 1972, ApJ, 171, 5

Wills B. J., Wills D., Breger M., Antonucci R. R. J., Barvainis R., 1992, ApJ, 398, 454

Woo J.-H., Urry C. M., 2002, ApJ, 579, 530

Wu J., et al., 2006, , 132, 1256

Zhang B.-K., Wang S., Zhao X.-Y., Dai B.-Z., Zha M., 2013, MNRAS, 428, 3630

Zhang B.-K., Jin M., Zhao X.-Y., Zhang L., Dai B.-Z., 2021, Research in Astronomy and Astrophysics, 21, 186

Zhou H., et al., 2007, ApJ, 658, L13

Zhou B., Dai B., Yang J., 2021, PASJ, 73, 850

Appendix A

Radiation mechanisms

The emission of a blazar is dominated by the emission of the jets (Blandford & Rees, 1978). There are two models for the emission of the jets, the leptonic and the hadronic model. The leptonic model is based on the acceleration of electrons (Ghisellini & Maraschi, 1989) and the hadronic model is based on the acceleration of both electrons and protons (Mannheim, 1993).

From radio to UV (even soft X-rays) the emission is due to synchrotron radiation (Urry & Mushotzky, 1982), and at higher energies is due inverse Compton (IC) process (Ghisellini et al., 1998) or due to hadronic processes (Mücke & Protheroe, 2001).

The widely accepted model is the leptonic, which proposes that the emission is due to synchrotron radiation and IC process (Ghisellini et al., 1998). The photons for the IC scattering can be produced in the accretion disk (Dermer & Schlickeiser, 1993), the BLR (Ghisellini et al., 1998) or they are the ones produced by the synchrotron radiation (Maraschi et al., 1992). The latter is named synchrotron-self Compton model.

A.1 Synchrotron radiation

Charged particles that move in regions with magnetic field will radiate. When high energy particles, e.g. extremely relativistic particles, radiate due to centrifugal acceleration in a magnetic field then the radiation is named *Synchrotron radiation* (Longair, 2011). The frequency of the emission is the frequency of the gyration in the magnetic field.

The total energy loss rate due to synchrotron radiation can be equated with the luminosity of a single electron from synchrotron radiation. The average energy loss rate is given by equation:

$$P_{syn} = -\left(\frac{\mathrm{d}E}{\mathrm{d}t}\right) = \frac{4}{3}\,\sigma_T\,c\,U_{mag}\left(\frac{u}{c}\right)^2\gamma^2 \tag{1.6}$$

where σ_T is the Thompson cross section, u is the velocity of the electron, c is the speed of light, $U_{mag} = B^2/8\pi$ is the magnetic field energy density and γ is the Lorentz factor (Longair, 2011).

A.2 Inverse Compton process

Inverse Compton process is the scattering between a relativistic electron and a low-energy photon. This process produces a high-energy photon and the electron loses the same amount of energy that the photon acquired. The rate of this process is proportional to the density of the photons (Acton, 1964).

The total energy loss rate due to inverse Compton scattering can be equated with the luminosity of a single electron from inverse Compton process. The average energy loss rate is given by equation:

$$P_{compt} = -\left(\frac{\mathrm{d}E}{\mathrm{d}t}\right) = \frac{4}{3}\,\sigma_T\,c\,U_{ph}\left(\frac{u}{c}\right)^2\gamma^2 \tag{1.7}$$

where U_{ph} is the density of the photons (Rybicki & Lightman, 1986).

By dividing equation 1.6 and 1.7 results to:

$$\frac{P_{syn}}{P_{compt}} = \frac{U_{mag}}{U_{ph}} \tag{1.8}$$

The ratio of energy losses due to synchrotron radiation and inverse Compton scattering is the same with the ratio of the magnetic field energy density to the photon energy density (Rybicki & Lightman, 1986).

Appendix B

Optical light curves of targets with little data

The optical light curves of the targets with little data can be found below.

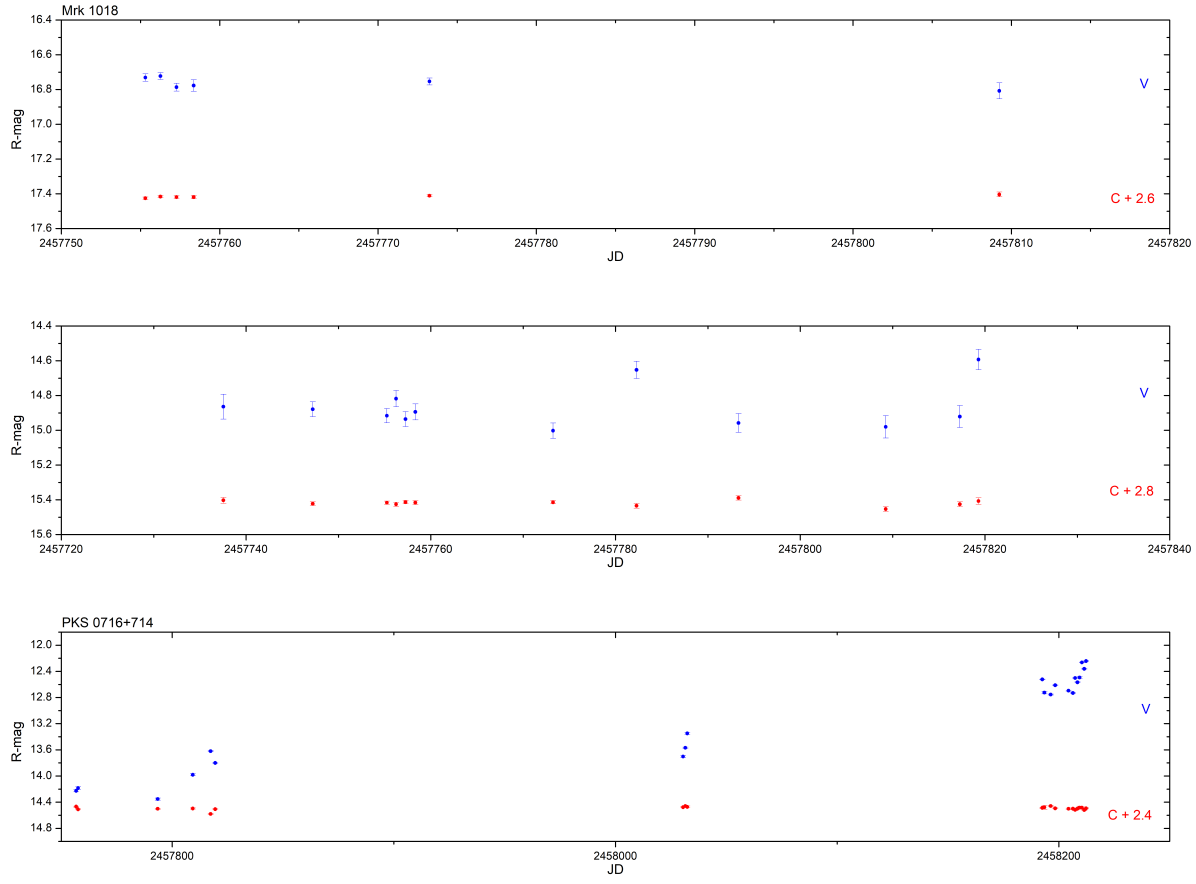

Figure B.1: Zoomed optical light curves of the target of table 4.2.

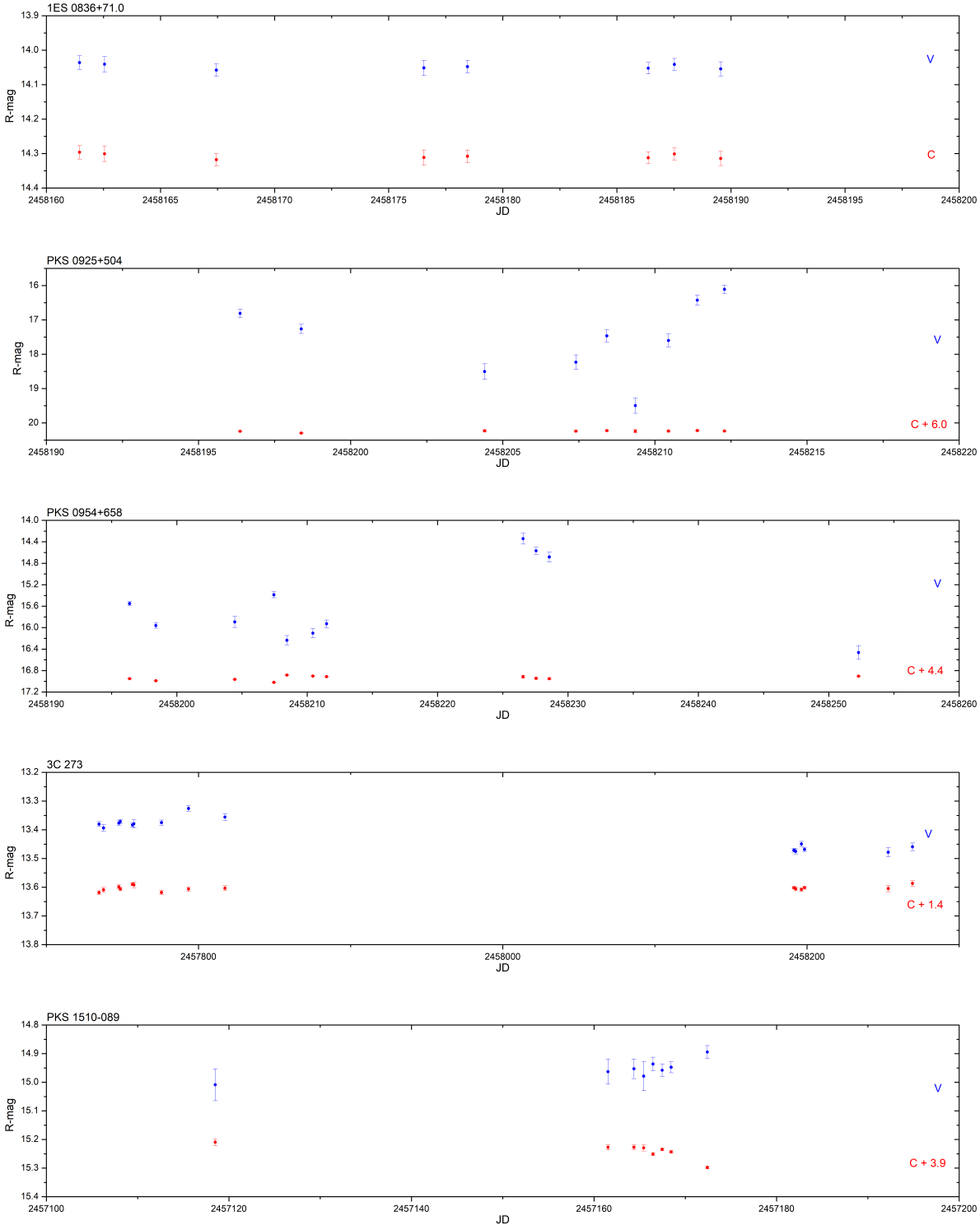

Figure B.2: Zoomed optical light curves of the target of table 4.2.

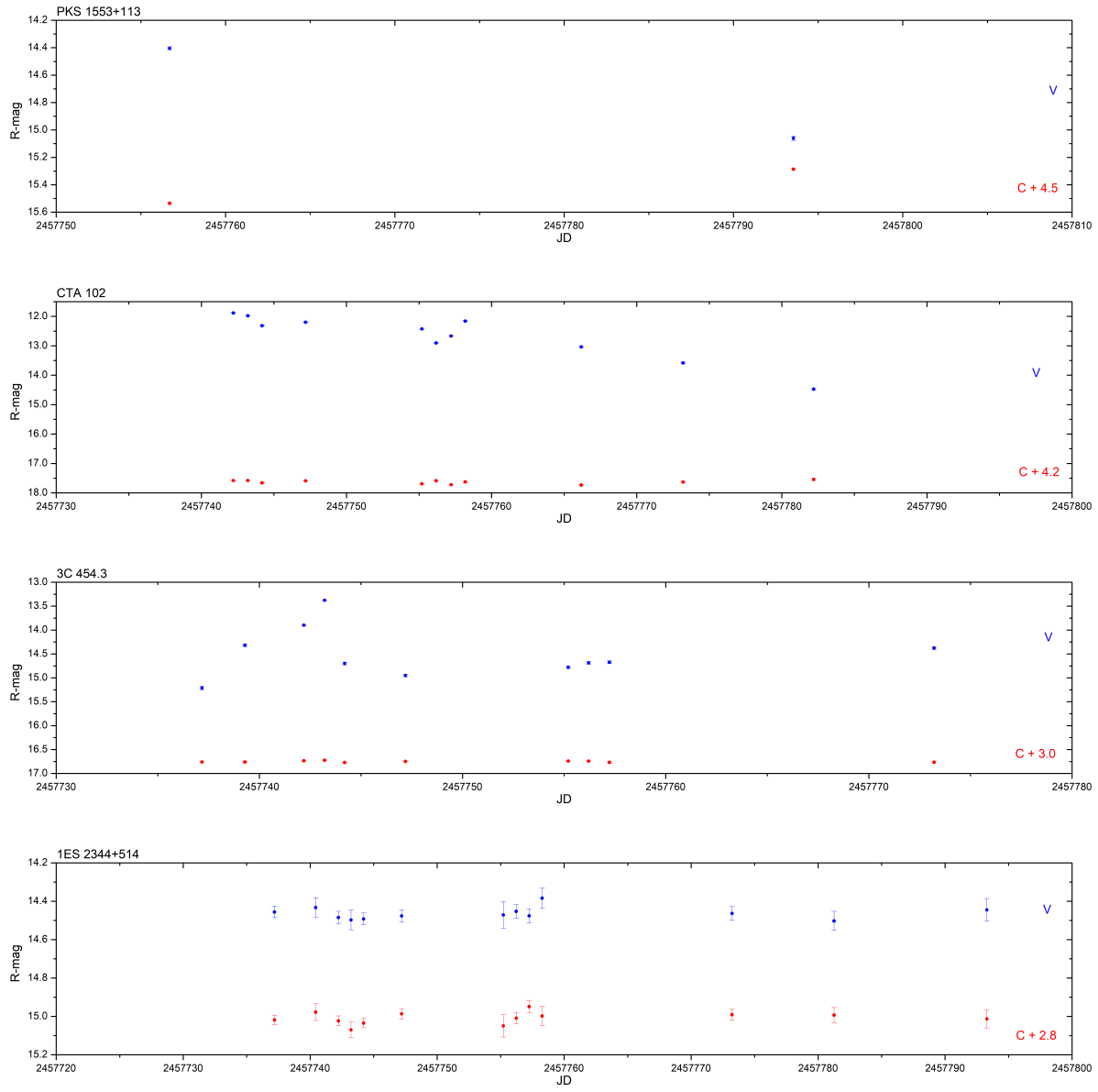

Figure B.3: Zoomed optical light curves of the target of table 4.2.

Appendix C

Data binning algorithm (One-day binning)

At first we import the libraries and the dataset.

```
import numpy as np
import pandas as pd
import matplotlib.pyplot as plt
import math
data = pd.read_csv("directory\filename.txt", sep='\t')
```

We change the name of the tags for easier use.

```
data.columns=['Julian_date','V','V_error','C','C_error']
time=pd.Series(data.Julian_date)
flux=pd.Series(data.V)
error=pd.Series(data.V_error)
# The index are timestamps in Julian Date, and differential magnitude
```

```
# The data in Plot form...
plt.plot(time.values, flux.values, '.', alpha=0.4)
plt.legend(['V-C'], loc=1)
plt.title("Light curve")
plt.xlabel("Julian Date")
plt.ylabel("R-mag")
plt.grid()
plt.tight_layout()
```

To do the 1-day binning we have to use the integer part of the Julian Date. We input that data to the array.

```
int_JD=pd.Series(time).astype(int)
df=pd.DataFrame(data)
df['intJD']=int_JD
```

We group the data based on the integer part of the Julian date.

```
new_data=df.groupby(['intJD']).agg({'Julian_date':['mean','size'],'V':'mean',
                                    'V_error':'mean','C':'mean','C_error':'mean'}).
                                    →reset_index()
new_data.head()
```

We export the array as a txt file.

```
new_data.to_csv(r"directory\filename.txt", sep='\t', float_format='%.5f')
```

Appendix D

Discrete Fourier Transform and Lomb-Scargle Periodogram algorithm

At first we set up the needed libraries.

```
import matplotlib.pyplot as plt
import numpy as np
from scipy.signal import find_peaks
from scipy.signal import lombscargle
from scipy.signal import welch
from scipy.stats import gamma
from scipy.stats import norm
import scipy.stats as st
import scipy.signal as signal
from astropy.timeseries import LombScargle
```

```
#Estimate noise power through the power spectral density over the range of large
 frequencies
#References: Pnevmatikakis et al, Neuron 2016
def estimate_noise(y, range_ff=[0.25, 0.5], method='mean'):
    ff, Pxx = welch(y)
    ind = np.logical_and(ff > range_ff[0], ff < range_ff[1])
    Pxx_ind = Pxx[ind]
    sn = {'mean': lambda Pxx_ind: np.sqrt(np.mean(Pxx_ind / 2)),
        'median': lambda Pxx_ind: np.sqrt(np.median(Pxx_ind / 2)),
        'logmexp': lambda Pxx_ind: np.sqrt(np.exp(np.mean(np.log(Pxx_ind / 2))))
    }[method](Pxx_ind)

    return sn
```

D.1 Uploading the data

```
data=np.loadtxt("directory\filename.txt", skiprows=1,usecols=(0, 1))
relflux = data[:,1] #flux data
JD = data[:,0] #time data
noise_data=estimate_noise(relflux) #estimate noise of signal
```

```
# Fourier Transform
DFT = np.fft.rfft(relflux)
freqs = np.fft.rfftfreq(n=relflux.size, d=0.01) # d gives the scale
power = np.abs(DFT)** 2.0

# Lomb-Scargle Periodogram

N_freqs = 1000000 #Number of steps

# Frequency limits
frequencies = np.linspace(3, 200, N_freqs)
#frequencies=np.linspace(N_min, N_max, N_freqs)

# create the periodograms
ls = LombScargle(JD, relflux)
periodogram=ls.power(frequencies)
```

D.2 Discrete Fourier Transform

Plotting the result of DFT.

```
plt.plot(24*1.0/freqs, power, ".-", color='k')
plt.xlim([0,8])
plt.xlabel("Period (h)")
plt.ylim([0,1])
plt.ylabel("Power")
plt.title("Discrete Fourier Power Spectrum")
plt.savefig('filename.eps', format='eps')
```

Finding the peaks and extracting the results.

```
#Level of confidence
threshold_DFT= power/2 + gamma.isf(q=0.01/2, a=1, scale=noise_data) #q=0.01/2 ->
                                                                    ->99\% confidence

# Get frequency of original signal
ff_ii = np.where((power>threshold_DFT)) #[0][0] # Just get one frequency, the other
                                       one is just mirrored freq at negative value
#print('frequency of:', ff_ii)

# Get the complex vector at that frequency to retrieve amplitude and phase shift
yy = DFT[ff_ii]
print('The frequencies are:', freqs[ff_ii])
print('The periods are:', 24*60/freqs[ff_ii])#For IDV: period=24*60/freqs[ff_ii] (min)
                                            for STV: period=1/freqs[ff_ii] (days)
index=np.asarray(ff_ii[0])

# Calculate the amplitude
T = freqs.shape[0] # domain of x; which we will divide height to get freq amplitude
A = 2*np.sqrt(yy.real**2 + yy.imag**2)/T
print('amplitude of:', A)

#Calculate signal to noise
noise=estimate_noise(power)
print("The noise is", noise)
snr=power[ff_ii]/noise
```

```
print("Signal to noise is:", snr)
```

```
data = np.array([freqs[ff_ii], 24*60/freqs[ff_ii], A, snr])
data_DFT=data.transpose()
np.savetxt("filename.txt" , data_DFT, delimiter='\t',fmt='%.4f',
            header="Frequency \t Period \t Amplitude \t S/N", comments="")
```

D.3 Lomb-Scargle Periodogram

Plotting the data.

```
plt.plot(24*1.0/frequencies, periodogram, color="k", label="Total unstacked")
plt.xlim([0,8])
plt.ylim([0,0.1])
plt.xlabel("Period (h)")
plt.ylabel("Power")
plt.title("Lomb-Scargle Periodogram")
plt.legend()
plt.savefig('filename.eps', format='eps')
```

Finding the peaks and extracting the results.

```
#Level of significance
threshold_LSP = np.abs(periodogram)**2/2 + norm.isf(q=0.01/2,scale=noise_data)
#q=0.01/2 -> 99\% confidence

#Searching for peaks
peaks1=find_peaks(periodogram, height=threshold_LSP)
height1=peaks1[1]['peak_heights']
peak_pos1=frequencies[peaks1[0]]

print('The frequencies are:', peak_pos1)
print('The periods are:', 24*60/peak_pos1)

# Calculate the amplitude
A1 = np.sqrt(height1)
print('amplitude of:', A1)

#Calculate signal to noise ratio
noise1=estimate_noise(height1)
print("The noise is:", noise1)
snr1=height1/noise1
print("Signal to noise is:", snr1)
```

```
data1 = np.array([peak_pos, 24*60/peak_pos, A1, snr1])
data_LS=data1.transpose()
np.savetxt("filename.txt" , data_LS, delimiter='\t',fmt='%.4f',
            header="Frequency \t Period \t Amplitude \t S/N", comments="")
```

Appendix E

Discrete Fourier Transform and Lomb-Scargle Periodogram testing algorithm

E.1 First test of DFT and LSP methods – Intermittent synthetic signal with known periods

For checking the quality of the methods used in the detection of QPOs (DFT, LSP), we created a synthetic light curve with 5 known periods. The signal and the detected periods can be seen in Fig. E.1, with red dashed line are the input periods of the periodic signal.

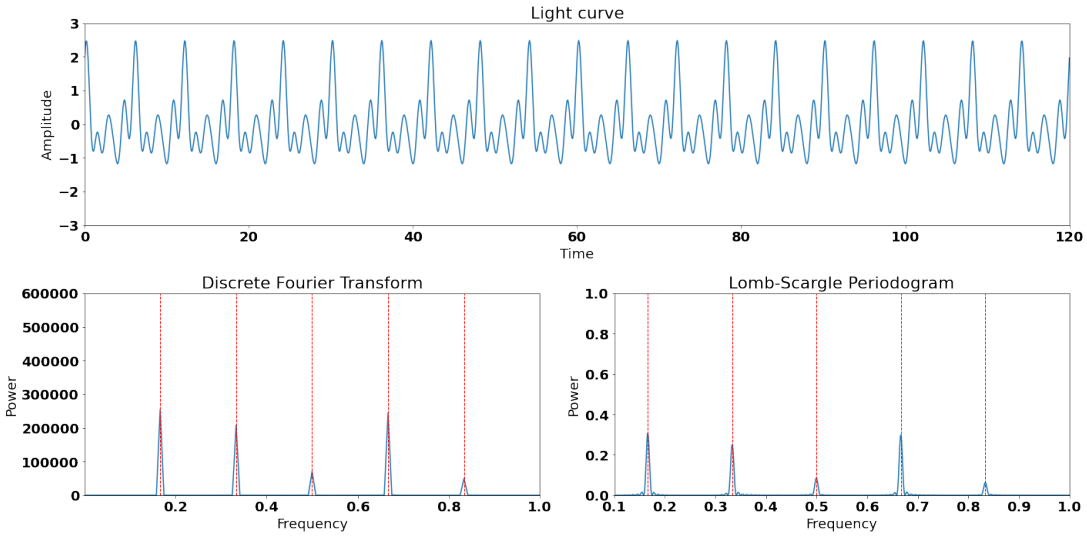

Figure E.1: Synthetic light curve and the periods detected using the DFT and the LSP.

Our original signal is noisy, thus white noise was added to the synthetic signal, in order to have signal to noise ratio equal to 5. The DFT and the LSP were applied to search for the input signal. The light curve and the detected periods are shown in Fig. E.2.

The periods are detected with great accuracy with both methods. Due to the fact that our original data are unevenly spaced, the study of a synthetic intermittent light curve is needed.

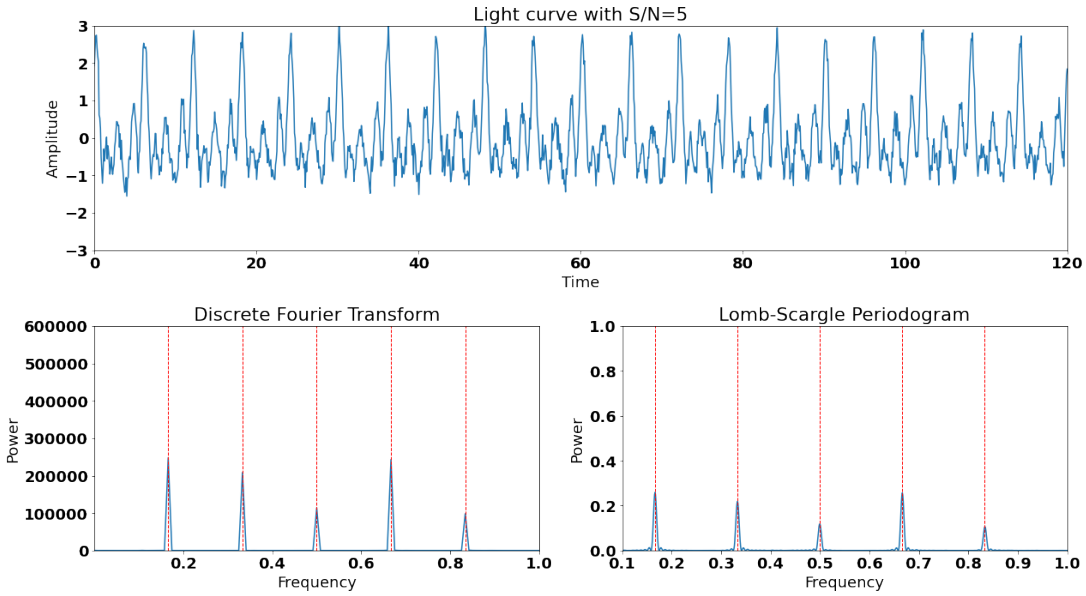

Figure E.2: Synthetic light curve with S/N=5 and the periods detected using the DFT and the LSP.

From the signal with S/N=5, we produced an intermittent light curve. The light curve and the detected periods can be seen in Fig. E.3.

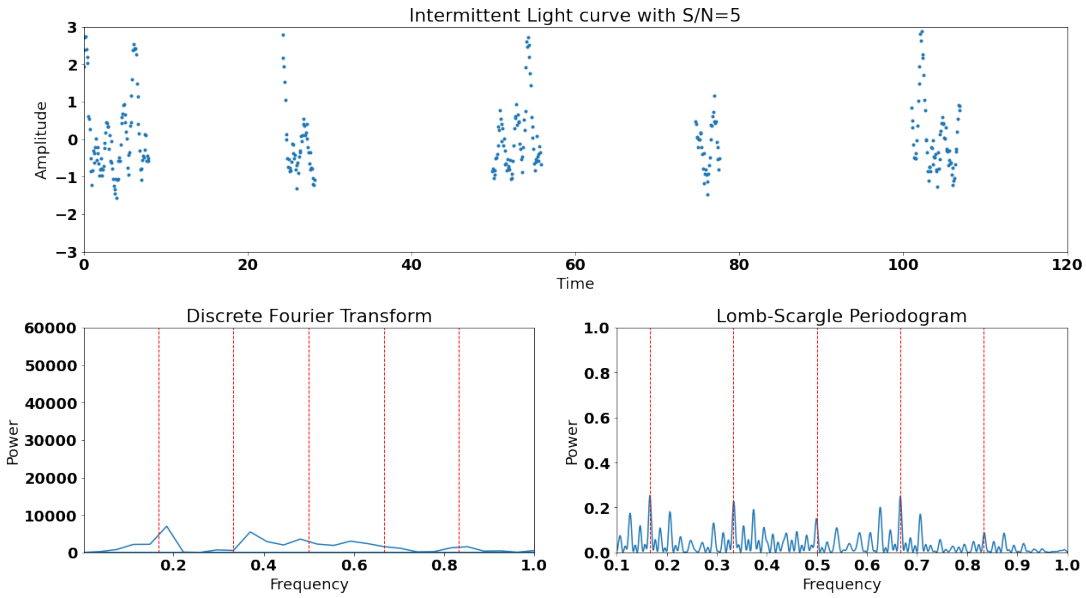

Figure E.3: Intermittent synthetic light curve with S/N=5 and the periods detected using the DFT and the LSP.

The periods of the signal can be successfully retrieved with both methods, but with lower accuracy in the detected frequencies, thus the methods are considered reliable even with sparse and noisy data, but a confidence interval is needed in order to retrieve the real periods.

The algorithm used for this test can be found below.

```
import matplotlib.pyplot as plt
import numpy as np
from scipy.signal import lombscargle

N_data = 5*24*12 #points in the time interval
t_max = 5*24 #how long you observe
half = N_data // 2

t = np.linspace(0, t_max, N_data)


#N = 120
#t = np.linspace(0, 120, N)
f0 = 1/6
phi = np.pi/2
A =  1

x = 7*A/10 * np.sin(2 * np.pi * f0 * t + phi)
+(np.sqrt(40)*A/10) * np.sin(2 * np.pi * 2*f0 * t + phi)
+ (np.sqrt(18)*A/9) * np.sin(2 * np.pi * 3*f0 * t + 0)
+(np.sqrt(13)*A/11+np.sqrt(15)*A/10) * np.sin(2 * np.pi * 4*f0 * t + 2*phi/3)
+(np.sqrt(12)*A/8) * np.sin(2 * np.pi * 5*f0 * t + phi/3)


# This gives us the fourier transform - it is a power for every frequency
DFT = np.fft.fft(x)

# This gives us the frequencies associated with each fourier transform power
freq = np.fft.fftfreq(x.size) * N_data/t_max

# Let's only take the positive half of the Fourier transform
half = len(x) // 2

font = {'family' : 'DejaVu Sans',
        'weight' : 'bold',
        'size'   : 18}

plt.rc('font', **font)

fig = plt.figure(figsize=(18,10))
a0 = plt.subplot2grid((2, 2), (0, 0), colspan=2)
a1 = plt.subplot2grid((2, 2), (1, 0), colspan=1)
a2 = plt.subplot2grid((2, 2), (1, 1), colspan=1)

a0.plot(t, x)
a0.axis([0, t_max, -3, 3])
a0.set_xlabel('Time')
a0.set_ylabel('Amplitude')


#fig = plt.figure(figsize=(10,5))
#plt.plot(t, x)

#plt.axis([0, t_max, -2, 2])
#plt.xlabel('Time')
#plt.ylabel('Amplitude')

#plt.show()

a1.plot(freq[:half], np.abs(DFT[:half])**2)
```

```
a1.axvline(f0, color='r',linestyle='--',linewidth=1)
a1.axvline(2*f0, color='r',linestyle='--',linewidth=1)
a1.axvline(3*f0, color='r',linestyle='--',linewidth=1)
a1.axvline(4*f0, color='r',linestyle='--',linewidth=1)
a1.axvline(5*f0, color='r',linestyle='--',linewidth=1)

a1.set_xlabel('Frequency')
a1.set_ylabel('Power')

a1.axis([0.001, 1, 0, 600000])

# Lomb-Scargle Periodogram
freq_max = 1
N_freq_test = 1000

frequencies = np.linspace(0.1, freq_max, N_freq_test)
angular_frequencies = 2 * np.pi * frequencies

# Create the periodogram
periodogram = lombscargle(t, x, angular_frequencies, normalize=True)

# Plot the periodogram
a2.plot(frequencies, periodogram, label='S/N=5')
a2.axvline(f0, color='r', linewidth=1, linestyle='--')
a2.axvline(2*f0, color='r', linewidth=1, linestyle='--')
a2.axvline(3*f0, color='r', linewidth=1, linestyle='--')
a2.axvline(4*f0, color='r', linewidth=1, linestyle='--')
a2.axvline(5*f0, color='r', linewidth=1, linestyle='--')
a2.set_xlabel('Frequency')
a2.set_ylabel('Power')
a2.set_xlim(0.1, freq_max)
a2.set_ylim(0, 1)

a0.set_title('Light curve')
a1.set_title('Discrete Fourier Transform')
a2.set_title('Lomb-Scargle Periodogram')

plt.tight_layout()
plt.show()
```

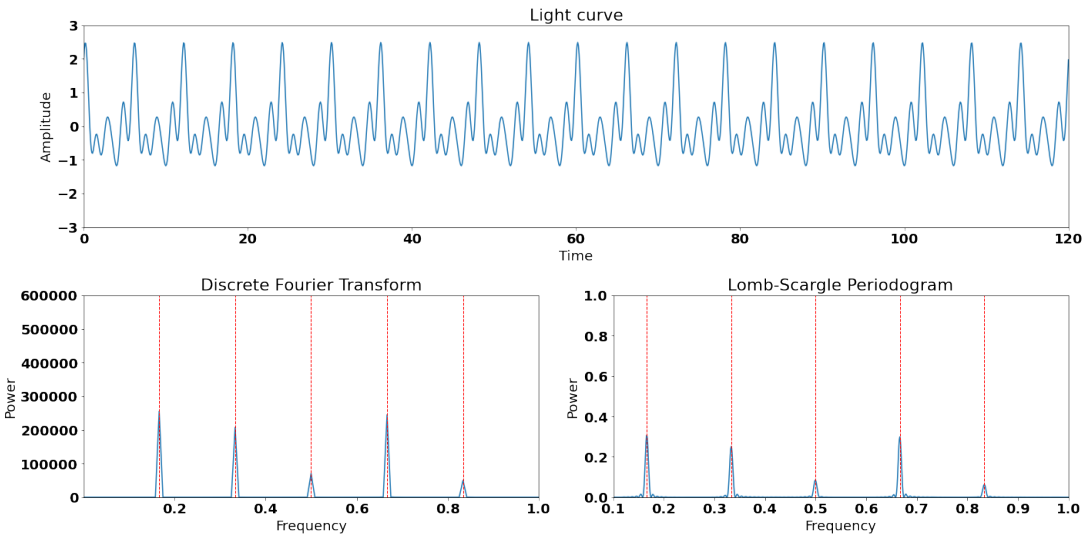

```
N=N_data
fig = plt.figure(figsize=(10,5))
noise1 = np.random.normal(0,0.2,N)

# First, we can take the Fourier transform to find the power per frequency
DFT = np.fft.fft(noise1)

# Now, we have to calculate the frequencies
freq = np.fft.fftfreq(noise1.size)

font = {'family' : 'DejaVu Sans',
        'weight' : 'bold',
        'size'   : 18}

plt.rc('font', **font)

f, (a0, a1) = plt.subplots(1, 2, gridspec_kw={'width_ratios': [3, 2]}, figsize=(20,8))
a0.plot(t, noise1, label='STDV=0.2')

a0.axis([0, t_max, -3, 3])
a0.set_xlabel('Time')
a0.set_ylabel('Amplitude')
a0.legend()


#fig = plt.figure(figsize=(10,5))
#plt.plot(t, x)

#plt.axis([0, t_max, -2, 2])
#plt.xlabel('Time')
#plt.ylabel('Amplitude')

#plt.show()

a1.plot(freq[:half], np.abs(DFT[:half])**2, label='STDV=0.2')

#a1.axvline(f0, color='r',linestyle='--',linewidth=1)

# Make plot pretty
a1.set_xlabel('Frequency')
a1.set_ylabel('Power')

a1.axis([0.001, 0.5, 0, 6000])
a1.legend()

# Lomb-Scargle Periodogram
freq_max = 1
N_freq_test = 1000

# do not change these...
frequencies = np.linspace(0.1, freq_max, N_freq_test)
angular_frequencies = 2 * np.pi * frequencies

# create the periodograms
periodogram_ns = lombscargle(t, noise1, angular_frequencies, normalize=True)

# Plot the periodogram
a2.plot(frequencies, periodogram_ns, label='S/N=5')
a2.set_xlabel('Frequency')
a2.set_ylabel('Power')
```

```
a2.set_xlim(0.1, freq_max)
a2.set_ylim(0, 1)

a0.set_title('White noise')
a1.set_title('Discrete Fourier Transform')
a2.set_title('Lomb-Scargle Periodogram')

plt.tight_layout()
plt.show()
```

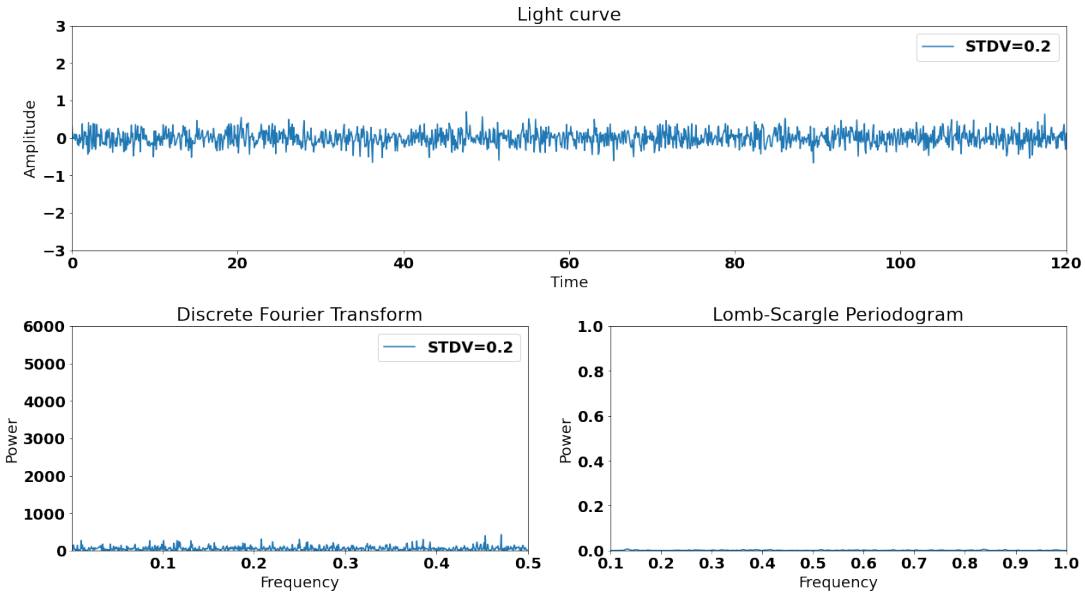


```
S1=x+noise1

# Run the Fourier transforms
DFT = np.fft.fft(S1)
freq = np.fft.fftfreq(S1.size)*N/t_max


font = {'family' : 'DejaVu Sans',
        'weight' : 'bold',
        'size'   : 18}

plt.rc('font', **font)

fig = plt.figure(figsize=(18,10))
a0 = plt.subplot2grid((2, 2), (0, 0), colspan=2)
a1 = plt.subplot2grid((2, 2), (1, 0), colspan=1)
a2 = plt.subplot2grid((2, 2), (1, 1), colspan=1)

a0.plot(t, S1, label='S/N=5')
a0.axis([0, t_max, -3, 3])
a0.set_xlabel('Time')
a0.set_ylabel('Amplitude')

a1.plot(freq[:half], np.abs(DFT[:half])**2, label='S/N=5')

a1.axvline(f0, color='r',linestyle='--',linewidth=1)
a1.axvline(2*f0, color='r',linestyle='--',linewidth=1)
a1.axvline(3*f0, color='r',linestyle='--',linewidth=1)
a1.axvline(4*f0, color='r',linestyle='--',linewidth=1)
a1.axvline(5*f0, color='r',linestyle='--',linewidth=1)
```

```
# Make plot pretty
a1.set_xlabel('Frequency')
a1.set_ylabel('Power')
a1.axis([0.001, 1, 0, 600000])

# Lomb-Scargle Periodogram
freq_max = 1
N_freq_test = 1000

# do not change these...
frequencies = np.linspace(0.1, freq_max, N_freq_test)
angular_frequencies = 2 * np.pi * frequencies

# create the periodograms
periodogram0 = lombscargle(t, S1, angular_frequencies, normalize=True)

# Plot the periodogram
a2.plot(frequencies, periodogram0, label='S/N=5')
a2.axvline(f0, color='r', linewidth=1, linestyle='--')
a2.axvline(2*f0, color='r', linewidth=1, linestyle='--')
a2.axvline(3*f0, color='r', linewidth=1, linestyle='--')
a2.axvline(4*f0, color='r', linewidth=1, linestyle='--')
a2.axvline(5*f0, color='r', linewidth=1, linestyle='--')
a2.set_xlabel('Frequency')
a2.set_ylabel('Power')
a2.set_xlim(0.1, freq_max)
a2.set_ylim(0, 1)

a0.set_title('Light curve with S/N=5')
a1.set_title('Discrete Fourier Transform')
a2.set_title('Lomb-Scargle Periodogram')

plt.tight_layout()
plt.show()
```

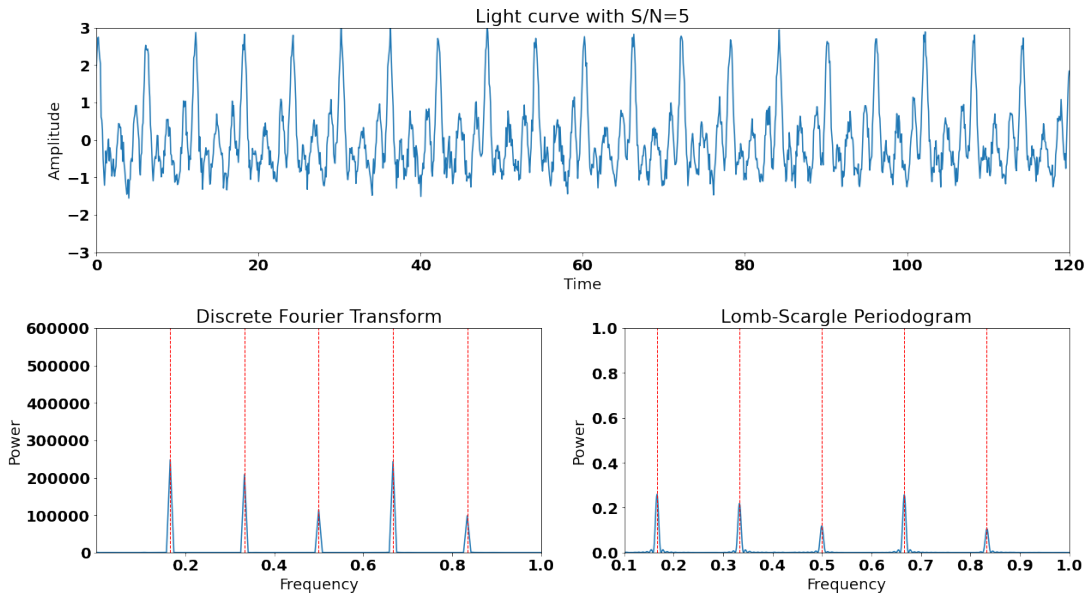


```
S1d=S1[0:int(1*24*12/3)] #8hours
S1d=np.append(S1d, S1[int(1*24*12+3):int(1*24*12+3)+int(1*24*12/6)]) #4hours
S1d=np.append(S1d, S1[int(2*24*12+22):int(2*24*12+22)+int(1*24*12/4)]) #6hours
S1d=np.append(S1d, S1[int(3*24*12+31):int(3*24*12+31)+int(1*24*12/8)]) #3hours
S1d=np.append(S1d, S1[int(4*24*12+59):int(4*24*12+59)+int(1*24*12/4)]) #6hours
```

```
td=t[0:int(1*24*12/3)] #8hours
td=np.append(td, t[int(1*24*12+3):int(1*24*12+3)+int(1*24*12/6)]) #4hours
td=np.append(td, t[int(2*24*12+22):int(2*24*12+22)+int(1*24*12/4)]) #6hours
td=np.append(td, t[int(3*24*12+31):int(3*24*12+31)+int(1*24*12/8)]) #3hours
td=np.append(td, t[int(4*24*12+59):int(4*24*12+59)+int(1*24*12/4)]) #6hours

# Run the Fourier transforms
DFT = np.fft.fft(S1d)
freq = np.fft.fftfreq(S1d.size)*N/t_max


font = {'family' : 'DejaVu Sans',
        'weight' : 'bold',
        'size'   : 18}

plt.rc('font', **font)


fig = plt.figure(figsize=(18,10))
a0 = plt.subplot2grid((2, 2), (0, 0), colspan=2)
a1 = plt.subplot2grid((2, 2), (1, 0), colspan=1)
a2 = plt.subplot2grid((2, 2), (1, 1), colspan=1)

a0.plot(td, S1d, '.', label='S/N=5')

a0.axis([0, t_max, -3, 3])
a0.set_xlabel('Time')
a0.set_ylabel('Amplitude')

a1.plot(freq[:half], np.abs(DFT[:half])**2, label='S/N=5')

a1.axvline(f0, color='r',linestyle='--',linewidth=1)
a1.axvline(2*f0, color='r',linestyle='--',linewidth=1)
a1.axvline(3*f0, color='r',linestyle='--',linewidth=1)
a1.axvline(4*f0, color='r',linestyle='--',linewidth=1)
a1.axvline(5*f0, color='r',linestyle='--',linewidth=1)

# Make plot pretty
a1.set_xlabel('Frequency')
a1.set_ylabel('Power')
a1.axis([0.001, 1, 0, 60000])


# Lomb-Scargle Periodogram
freq_max = 1
N_freq_test = 1000

frequencies = np.linspace(0.1, freq_max, N_freq_test)
angular_frequencies = 2 * np.pi * frequencies

# create the periodograms
periodogram2 = lombscargle(td, S1d, angular_frequencies, normalize=True)

# Plot the periodogram
a2.plot(frequencies, periodogram2, label='S/N=5')
a2.axvline(f0, color='r', linewidth=1, linestyle='--')
a2.axvline(2*f0, color='r', linewidth=1, linestyle='--')
a2.axvline(3*f0, color='r', linewidth=1, linestyle='--')
a2.axvline(4*f0, color='r', linewidth=1, linestyle='--')
a2.axvline(5*f0, color='r', linewidth=1, linestyle='--')
```

```
a2.set_xlabel('Frequency')
a2.set_ylabel('Power')
a2.set_xlim(0.1, freq_max)
a2.set_ylim(0, 1)

a0.set_title('Intermittent Light curve with S/N=5')
a1.set_title('Discrete Fourier Transform')
a2.set_title('Lomb-Scargle Periodogram')

plt.tight_layout()
plt.show()
```

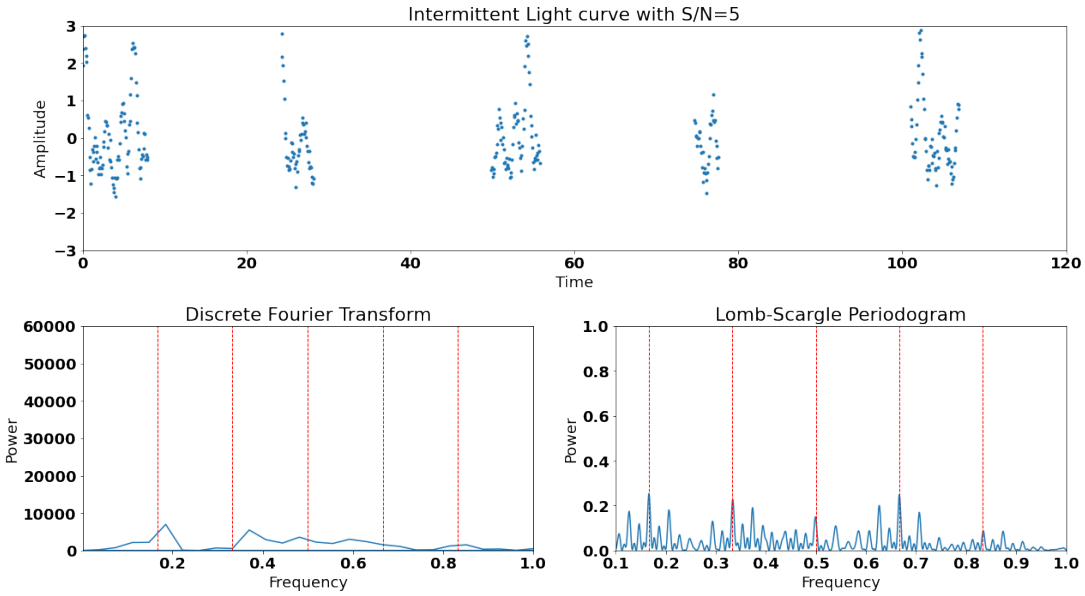

E.2 Second test of significance of DFT and LSP – Added noise to original data

Another way to check the significance of the detected QPOs is by comparing the detected signals in the light curve of one of our targets with the detected signals in the same light curve when noise was added. The detected QPOs of the noisy data series are identical to the original signal, and thus the methods used are considered reliable.

The noisy data that were used to check the significance of the methods were created using the following commands. The noise of the original data was used in order to create the noisy signal.

```
noise_data=estimate_noise(relflux)
print("Noise is:", noise_data)

relflux_1=relflux+np.random.normal(0, 2*noise_data, relflux.size)
data_1=np.array([JD, relflux_1])
```

E.3 Third test of significance of DFT and LSP – Added a periodicity in the original data

Similarly to the second method, to check the quality of the detected QPOs we used the observed data set from one of the targets. A intermittent signal with a known period was added to the original data set. The DFT and the LSP were used to search for the original signals, and detected both the original QPOs and the input signal. Thus the methods used are considered reliable.

The data that were used to check the significance of the methods were created using the following algorithm.

```
x = 13.67+ noise_data* np.sin(2 * np.pi * 34.3 * JD)
x_new=np.random.choice(x, round(0.25*JD.size), replace=False)
t= np.random.uniform(min(JD), max(JD), round(0.25*JD.size))

data_per=np.array([t,x_new])

data_trans=data.transpose()
data2=np.append(data_trans, data_per, axis=1)
data_2=data2.transpose()

relflux_2 = data_2[:,1] #flux data
JD_2 = data_2[:,0] #time data
```

Appendix F

Tables of detected timescales of QPOs in optical wavelengths

F.1 Tables of intra-day timescales of QPOs in optical wavelengths

1ES 0236+61

Table F.1: Period of the detected IDVs in the optical light curves of 1ES 0236+61.

JD	Duration (min)	Discrete Fourier Transform (P04)			Fast Fourier Transform (Python)			Lomb-Scargle Periodogram		
		Period (min)	Amplitude	S/N	Period (min)	Amplitude	S/N	Period (min)	Amplitude	S/N
2457747	604.04	106.93±1.45	0.007±0.001	10.4				106.90	0.50	24.4
		47.01±0.52	0.004±0.001	5.0				46.97	0.28	7.4
		18.25±0.07	0.004±0.001	5.2				18.25	0.33	10.4
		15.10±0.06	0.003±0.001	5.7				15.12	0.26	6.4
2457756	496.70	73.75±0.88	0.003±0.001	6.5	96.55	0.002	3.0	96.87	0.14	3.0
		62.21±0.73	0.003±0.001	5.4	73.88	0.002	3.1	74.07	0.27	10.8
		26.44±0.17	0.002±0.001	4.8	42.48	0.002	3.9	61.69	0.24	8.4
					29.30	0.002	3.4	42.78	0.19	5.2
								28.57	0.17	4.5
								26.47	0.19	5.1

PKS 0716+714

Table F.2: Period of detected IDVs in the optical light curves of PKS 0716+714.

JD	Duration (min)	Discrete Fourier Transform (P04)			Fast Fourier Transform (Python)			Lomb-Scargle Periodogram		
		Period (min)	Amplitude	S/N	Period (min)	Amplitude	S/N	Period (min)	Amplitude	S/N
2458030	359.61	52.13±1.43	0.010±0.001	9.2				52.30	0.3	3.3
2458031	471.34	231.96±6.58	0.017±0.002	4.8	227.31	0.011	7.8	227.41	0.4983	77.6
		66.56±1.54	0.006±0.002	5.9	138.37	0.006	2.3	138.45	0.1919	11.5
		50.51±0.81	0.007±0.002	5.0	63.65	0.008	4.4	64.43	0.1697	9.0
		32.55±0.28	0.008±0.002	2.5				50.86	0.1814	10.3
								32.53	0.2197	15.1
2458032	238.85	48.79±5.96	0.007±0.001	2.9	49.95	0.009	1.8			

OJ 287

Table F.3: Period of the detected IDVs in the optical light curves of OJ 287.

JD	Duration (min)	Discrete Fourier Transform (P04)			Fast Fourier Transform (Python)			Lomb-Scargle Periodogram		
		Period (min)	Amplitude	S/N	Period (min)	Amplitude	S/N	Period (min)	Amplitude	S/N
2457354	844.24	182.64±1.17	0.031±0.002	9.1	181.33	0.005	5.5	182.26	0.59	15.2
		121.08±0.57	0.028±0.002	16.1	85.89	0.005	4.9	120.31	0.33	4.9
		97.35±0.44	0.023±0.002	15.9	81.60	0.005	5.6	95.67	0.20	1.8
		78.74±0.62	0.011±0.002	4.4				85.38	0.28	3.5
2457360	943.00	239.81±3.50	0.031±0.003	4.1	236.27	0.009	6.4	221.67	0.21	6.5
		109.88±0.26	0.090±0.003	8.9	219.97	0.008	4.4	168.13	0.23	7.6
		89.96±0.20	0.077±0.003	11.2	167.87	0.011	9.2	137.45	0.27	10.8
					138.68	0.013	11.5	108.90	0.17	4.4
					111.92	0.006	3.0			
					86.21	0.009	5.5			
2457362	1315.24	291.97±1.09	0.076±0.002	16.9	331.62	0.013	7.9	327.26	0.27	7.3
					289.11	0.012	7.2			
2457365	1285.36	517.90±15.37	0.026±0.003	1.6	518.40	0.013	15.1			
		36.33±0.49	0.004±0.003	5.4	34.95	0.008	6.1			
		29.94±0.38	0.003±0.003	3.0	30.95	0.013	15.2			
					29.48	0.012	11.9			
2457366	1195.2432	98.70±0.75	0.014±0.002	2.4	96.23	0.010	3.8	95.63	0.28	2.2
2457367	728.64	93.27±1.44	0.004±0.001	2.2	118.50	0.004	3.3	120.02	0.20	2.1
		40.68±0.41	0.003±0.001	3.5	92.68	0.003	2.1			
					39.72	0.004	4.4			
2457369	972.49	206.34±5.69	0.030±0.007	3.3	324.00	0.020	5.8	319.05	0.28	2.2
		125.27±4.75	0.013±0.007	1.5	204.63	0.026	9.4	193.64	0.28	2.2
					194.40	0.021	6.1			
					121.50	0.014	2.6			
2457373	679.12	248.08±1.85	0.046±0.002	6.7	252.90	0.006	9.7	237.02	0.47	5.0
		179.30±8.12	0.006±0.002	2.1	238.02	0.007	12.7	136.76	0.19	0.8
		143.35±0.84	0.034±0.002	15.6	183.93	0.004	3.8	86.92	0.18	0.7
		117.34±1.30	0.015±0.002	4.6	144.51	0.005	6.2			
		82.95±0.70	0.014±0.002	4.1	134.88	0.004	4.7			
		65.07±0.65	0.009±0.002	1.9	119.01	0.005	5.2			
					62.25	0.004	4.7			
2457376	1180.43	382.80±3.38	0.056±0.003	6.7	387.60	0.010	10.8			
2457377	703.20	183.76±3.80	0.035±0.005	2.1	184.00	0.008	2.3			
		74.60±6.17	0.004±0.005	0.4	74.43	0.009	2.9			
2457380	443.23	173.79±4.94	0.037±0.005	3.4	184.80	0.009	5.9	184.34	0.27	9.0
		124.84±2.78	0.034±0.005	9.1	170.58	0.008	5.2	120.38	0.19	4.7
		98.49±2.20	0.026±0.005	9.9	119.87	0.007	3.5	92.00	0.20	5.1
		68.71±3.54	0.008±0.005	0.8	98.56	0.007	3.4			
					67.20	0.006	3.1			
2457396	1083.23				277.60	0.005	4.5	280.85	0.36	8.8
					208.20	0.009	15.8	207.81	0.27	4.9
					161.19	0.005	4.2	160.56	0.29	5.8
					116.20	0.006	5.9	113.23	0.23	3.7
					80.59	0.005	5.7	79.22	0.25	4.2

Table F.3 continued from previous page

2457407	446.07				93.26	0.004	4.0	91.45	0.30	4.1
					50.22	0.004	4.2	49.55	0.17	1.4
2457445	557.08	29.70±0.34	0.002±0.001	1.3	37.38	0.004	8.2	38.28	0.19	2.9
					34.00	0.003	3.6	34.31	0.17	2.4
								31.94	0.21	3.6
2457464	1069.37	232.34±5.58	0.018±0.004	1.9	173.83	0.004	4.6	228.36	0.28	7.5
		161.96±2.35	0.021±0.004	1.7	162.24	0.004	4.9	176.76	0.34	11.4
					143.15	0.004	5.4	140.25	0.34	11.3
					105.81	0.004	4.4	107.59	0.31	9.7
					88.49	0.005	8.0	88.34	0.16	2.7
2458538	822.64	56.54±0.84	0.002±0.001	1.5	60.67	0.004	3.3	59.31	0.15	3.0
		39.84±0.39	0.002±0.001	3.6	58.70	0.004	2.7	54.06	0.15	2.9
					56.84	0.004	2.6			
					39.42	0.004	2.4			
2458539	984.56	101.76±0.59	0.011±0.001	3.8				100.60	0.22	0.6
2458541	1430.09	21.30±0.06	0.003±0.001	5.2				21.33	0.17	5.1
2458542	481.75	163.10±12.23	0.001±0.001	2.1	164.51	0.004	5.9	45.16	0.14	1.5
		45.65±0.89	0.002±0.001	4.7				20.67	0.14	1.5
		19.42±0.10	0.003±0.001	4.3				19.49	0.21	3.1

Mrk 421

Table F.4: Period of the detected IDVs in the optical light curves of Mrk 421.

JD	Duration (min)	Discrete Fourier Transform (P04)			Fast Fourier Transform (Python)			Lomb-Scargle Periodogram		
		Period (min)	Amplitude	S/N	Period (min)	Amplitude	S/N	Period (min)	Amplitude	S/N
2456369	134.19	24.07±0.53	0.005±0.001	32.8				24.11	0.25	2.0
2456638	172.30	48.30±1.24	0.009±0.002	3.1				45.77	0.46	6.8
		24.91±0.93	0.003±0.002	3.5				25.44	0.22	1.5
		19.32±0.28	0.006±0.002	27.8				18.87	0.24	1.9
		17.82±0.21	0.007±0.002	32.5				17.96	0.24	1.8
2457741	197.16	91.73±1.99	0.011±0.001	13.9				91.75	0.48	11.9
		47.52±0.75	0.008±0.001	12.0				45.90	0.40	8.1
		29.21±0.46	0.005±0.001	23.5				28.73	0.20	2.1
		16.78±0.15	0.005±0.001	8.5				16.79	0.24	2.8
2457766	270.92	108.49±1.95	0.009±0.001	6.7				106.44	0.35	6.7
		60.24±0.75	0.007±0.001	20.8				63.79	0.22	2.6
		43.02±0.21	0.013±0.001	27.7				42.77	0.49	13.4
		31.33±0.24	0.006±0.001	17.4				31.13	0.30	5.0
		23.16±0.16	0.005±0.001	16.2				23.50	0.23	2.9
2457799	217.40	75.06±2.18	0.009±0.001	4.9				74.03	0.31	6.9
		42.66±0.36	0.018±0.001	26.8				42.66	0.51	18.5
		34.53±0.41	0.010±0.001	15.6				33.86	0.35	8.4
		25.89±0.28	0.009±0.001	8.6				27.30	0.24	4.1
		19.77±0.22	0.006±0.001	21.1				19.72	0.20	2.8
2458136	204.32	69.42±1.29	0.007±0.001	21.1				72.83	0.32	3.7
		41.76±0.23	0.01±0.001	108.6				41.49	0.65	15.5
		34.67±0.39	0.006±0.001	38.0				33.02	0.35	4.4
		18.59±0.19	0.003±0.001	4.2				19.34	0.17	1.1
								17.74	0.19	1.3
2458137	252.85	36.30±0.79	0.005±0.001	4.6				35.13	0.17	2.8
		25.25±0.41	0.004±0.001	4.0				25.76	0.17	2.7
		23.06±0.26	0.006±0.001	3.5				22.95	0.21	4.1
2458144	303.51	29.23±0.37	0.004±0.001	8.8	38.29	0.007	8.4	37.71	0.21	1.7
		18.25±0.20	0.003±0.001	8.5				29.38	0.28	3.1
								18.23	0.19	1.5
								17.12	0.18	1.3
2458145	526.68	72.18±1.17	0.003±0.001	6.0	249.23	0.003	3.3	245.87	0.40	33.3
		48.55±0.57	0.003±0.001	5.9	72.00	0.003	3.3	71.39	0.19	7.6
					55.54	0.003	4.6	57.16	0.15	4.9
								49.02	0.16	5.4
2458146	258.05	30.77±0.66	0.003±0.001	3.5	75.99	0.004	2.9	74.44	0.24	6.0
					53.11	0.004	4.1	53.47	0.17	2.8
					32.93	0.005	4.1	31.71	0.18	3.1
2458147	345.36	140.43±5.55	0.004±0.001	4.7	143.06	0.003	3.4	137.95	0.24	6.0
		91.87±3.38	0.003±0.001	10.5	92.69	0.004	4.2	91.92	0.21	4.8
		68.94±1.96	0.003±0.001	9.7	68.55	0.004	4.9	68.98	0.18	3.6
		32.10±0.23	0.006±0.001	9.0	40.62	0.004	4.2	42.98	0.16	2.6
		22.63±0.16	0.004±0.001	5.2	38.94	0.004	3.8	37.22	0.19	3.6
		17.35±0.12	0.003±0.001	6.1				32.60	0.24	6.0
								22.64	0.18	3.3
								18.78	0.15	2.5

Table F.4 continued from previous page

2458148	295.04	16.28±0.15	0.003±0.001	8.4				16.23	0.17	2.9
2458149	349.08	122.75±3.77	0.006±0.001	4.6	90.74	0.004	3.5	118.04	0.28	2.6
		87.40±4.46	0.002±0.001	4.1	41.40	0.005	4.7			
		42.86±1.07	0.002±0.001	4.6						
2458150	318.53	76.84±2.02	0.007±0.001	6.9	80.05	0.005	2.0	77.02	0.24	3.1
		45.21±0.66	0.007±0.001	9.2804				45.00	0.26	3.6
2458191	206.15	37.13±1.18	0.005±0.002	9.0	30.63	0.007	2.9	36.16	0.20	4.1
		29.23±1.45	0.003±0.002	4.0						
2458192	338.16	79.60±2.68	0.004±0.001	8.1	40.52	0.005	4.0	79.74	0.18	3.4
		43.64±1.14	0.003±0.001	6.7				22.45	0.19	3.8
		22.47±0.18	0.005±0.001	7.3						

BL Lac

Table F.5: Period of the detected IDVs in the optical light curves of BL Lac.

JD	Duration (min)	Discrete Fourier Transform (P04)			Fast Fourier Transform (Python)			Lomb-Scargle Periodogram		
		Period (min)	Amplitude	S/N	Period (min)	Amplitude	S/N	Period (min)	Amplitude	S/N
2457984	450.53	90.31±3.09	0.008±0.003	5.1	220.11	0.009	5.4	226.46	0.32	11.1
		62.24±1.91	0.007±0.003	6.1	88.05	0.008	4.7	91.17	0.17	3.1
		46.99±0.63	0.011±0.003	27.7	61.63	0.007	3.3	46.68	0.24	6.2
		42.75±0.77	0.008±0.003	13.8				41.36	0.21	5.1
2457999	502.78	135.98±3.77	0.011±0.002	13.3	98.01	0.006	2.4	134.59	0.28	8.5
		17.74±0.15	0.005±0.002	3.0				95.89	0.23	5.6
		15.91±0.10	0.006±0.002	3.1				16.53	0.17	3.3
								15.88	0.16	2.7
2458000	565.23	86.33±2.00	0.005±0.001	3.1	87.38	0.005	2.4	83.72	0.18	115.3
		45.05±0.63	0.004±0.001	5.1				45.10	0.18	116.3
		35.33±0.38	0.004±0.001	6.52				35.20	0.18	121.0
2458291	282.86	103.53±6.10	0.015±0.004	2.1	62.88	0.016	2.8	104.50	0.26	2.2
		60.41±1.98	0.016±0.004	3.7				59.16	0.29	2.7
		41.10±1.11	0.013±0.004	4.9				40.44	0.27	2.4
2458292	272.36									
2458299	340.08	69.48±5.06	0.005±0.003	1.3				66.73	0.17	1.1
		46.30±1.10	0.009±0.003	6.6				46.87	0.26	2.8
2458305	276.49	96.67±2.70	0.014±0.002	3.7				92.15	0.42	5.2
		59.98±1.20	0.012±0.002	12.2				57.36	0.34	3.5
		43.47±0.96	0.008±0.002	9.3				41.61	0.24	1.7
		29.23±0.41	0.008±0.002	10.0				29.00	0.31	2.8
		25.94±0.56	0.005±0.002	4.2				25.46	0.26	2.0
2458306	425.53	118.05±2.52	0.013±0.002	12.7	140.40	0.012	9.2	145.10	0.35	3.6
		37.31±0.45	0.007±0.002	5.0	117.00	0.007	3.2	114.36	0.39	4.0
		22.81±0.19	0.007±0.002	9.1				37.65	0.23	1.9
								22.86	0.21	1.6
2458307	397.44	38.61±0.86	0.009±0.004	13.7				39.31	0.18	3.2
2458308	300.46									
2458310	425.09	67.65±1.17	0.015±0.003	4.2	176.91	0.008	2.2	178.24	0.41	11.4
		48.12±1.12	0.008±0.003	1.3	47.63	0.008	2.2	68.37	0.27	4.9
		39.61±0.74	0.008±0.003	2.0	39.31	0.009	2.7	46.96	0.19	2.4
								38.20	0.24	4.0
2458311	425.64	100.52±3.64	0.006±0.002	6.0	40.70	0.008	4.7	99.42	0.21	7.1
		72.95±2.20	0.005±0.002	6.1				70.57	0.20	6.1
		39.65±0.64	0.005±0.002	30.2				39.75	0.23	8.1
		35.08±0.43	0.006±0.002	11.8				35.05	0.24	9.5
		25.06±0.20	0.006±0.002	6.9				25.40	0.23	8.7
		18.32±0.11	0.007±0.002	6.2				18.33	0.24	9.3
2458312	415.15	116.65±2.81	0.016±0.003	11.3	119.40	0.007	4.8	116.99	0.36	8.8
		67.96±1.84	0.009±0.003	4.1				64.29	0.17	2.0
		43.20±0.84	0.008±0.003	3.5				41.46	0.17	1.9
2458313	459.60	88.26±3.86	0.008±0.003	1.2	191.70	0.010	5.3	187.36	0.31	6.9
		32.35±0.37	0.011±0.003	3.2	85.20	0.008	3.4	32.24	0.19	2.6
2458314	455.54	144.78±3.55	0.010±0.001	11.8	33.75	0.006	3.5	144.73	0.39	5.6

Table F.5 continued from previous page

		88.52±1.64	0.008±0.001	7.5				87.85	0.31	3.6
		43.82±0.67	0.005±0.001	6.4				43.54	0.20	1.5
		25.10±0.22	0.005±0.001	9.4				30.73	0.17	1.1
								25.22	0.19	1.3
2458315	419.40	114.30±13.81	0.004±0.003	0.6	179.10	0.009	6.2	182.75	0.25	3.8
		63.36±1.22	0.013±0.003	2.2	114.62	0.007	4.4	102.52	0.21	2.7
		52.30±0.87	0.013±0.003	2.0	98.81	0.009	7.1	65.25	0.23	3.2
		34.04±0.50	0.009±0.003	4.1	32.20	0.007	4.5	51.03	0.27	4.5
		28.99±0.35	0.010±0.003	3.4	30.49	0.007	4.1	34.06	0.20	2.3
								29.04	0.19	2.3
2458316	419.00	160.02±8.12	0.011±0.003	1.9	41.08	0.010	5.9	163.89	0.28	2.0
		108.31±3.15	0.013±0.003	3.6				110.65	0.33	2.8
		72.64±1.92	0.009±0.003	4.1				71.23	0.22	1.2
		43.56±1.22	0.005±0.003	2.8						
2458317	406.83	177.75±13.92	0.007±0.002	1.2	172.80	0.008	4.7	66.07	0.22	1.7
		64.18±1.53	0.008±0.002	3.6				55.45	0.28	2.7
		55.82±0.86	0.010±0.002	8.9				47.60	0.27	2.4
		49.08±0.84	0.008±0.002	7.0						
2458318	269.04	71.22±3.76	0.005±0.002	3.6				68.22	0.26	6.6
		32.50±0.64	0.007±0.002	5.9				32.65	0.25	6.1
		26.83±0.46	0.006±0.002	8.3				26.49	0.23	5.4
2458771	540.86	197.47±14.47	0.010±0.004	1.2	199.20	0.009	3.1	183.06	0.22	0.2
		140.89±4.69	0.016±0.004	2.9	179.28	0.009	3.2	102.52	0.23	0.2
		91.84±3.57	0.009±0.004	2.2	143.42	0.009	3.0			
		47.28±1.17	0.007±0.004	6.7	105.46	0.010	3.9			
					91.94	0.009	3.0			
					46.57	0.010	3.9			
2458772	590.80	189.01±6.51	0.014±0.003	3.6	187.89	0.012	3.9	20.31	0.22	1.6
		33.52±0.25	0.011±0.003	4.6	34.61	0.009	2.5			
		32.23±0.18	0.015±0.003	14.2	32.61	0.009	2.4			
		30.73±0.27	0.009±0.003	3.0	31.82	0.009	2.1			
		20.35±0.08	0.013±0.003	6.2						
2458775	536.23	73.15±1.46	0.018±0.005	4.7	70.43	0.018	2.7			
		54.00±1.68	0.009±0.005	2.1	56.84	0.016	2.3			
		28.33±0.42	0.010±0.005	8.5	30.28	0.017	2.4			
2458776	403.53	121.15±4.37	0.04±0.01	5.4	85.03	0.031	2.7	122.88	0.36	4.2
		86.21±4.73	0.02±0.01	7.0	66.13	0.029	2.5			
		65.82±2.55	0.02±0.01	7.4	32.47	0.023	1.5			
		31.33±0.41	0.03±0.01	3.2	30.79	0.031	2.8			
2458777	543.24	109.90±2.09	0.016±0.003	4.9	54.72	0.010	2.1	113.80	0.27	3.2
		58.77±0.63	0.016±0.003	9.6	49.40	0.011	2.9	59.17	0.29	3.5
		53.03±0.82	0.010±0.003	23.1						
		48.32±0.47	0.014±0.003	44.5						
2458778	482.41	181.70±7.94	0.016±0.003	2.5	181.27	0.013	3.0	177.81	0.31	11.9
		85.31±2.07	0.013±0.003	3.8	96.30	0.011	2.1	95.50	0.25	8.1
					83.29	0.017	5.1	80.61	0.26	8.3
					56.03	0.011	2.3	59.72	0.24	7.0
2458779	426.53	84.68±1.42	0.029±0.004	13.8	84.22	0.011	1.6	84.97	0.35	0.4
		63.31±2.25	0.010±0.004	4.2	63.16	0.019	5.1			
2458780	572.03	130.21±3.16	0.019±0.003	2.3	172.15	0.013	3.1	173.51	0.27	3.6
		60.58±0.98	0.013±0.003	2.2	130.59	0.015	3.9	129.90	0.29	4.3
		48.92±0.72	0.012±0.003	2.5	60.11	0.011	2.0	60.23	0.22	2.4
					47.94	0.011	2.3	48.85	0.21	2.3

F.2 Tables of short-term timescales of QPOs in optical wavelengths

OJ 287

Table F.6: Period of the detected STVs in the optical light curves of OJ 287.

JD	Duration	Discrete Fourier Transform (P04)			Fast Fourier Transform (Python)			Lomb-Scargle Periodogram		
	(days)	Period (days)	Amplitude	S/N	Period (days)	Amplitude	S/N	Period (days)	Amplitude	S/N
2457267-2457554	287	93.71±0.83	0.40±0.02	17.9	95.57	0.176	17.7	94.05	0.61	7.3
		64.29±0.91	0.17±0.02	7.7	66.90	0.272	42.4			
		39.77±0.24	0.26±0.02	11.3	39.35	0.078	3.5			
		32.73±0.38	0.11±0.02	4.8	33.45	0.102	5.9			
		22.21±0.14	0.13±0.02	5.8	23.07	0.077	3.4			
2457629-2457919	290	62.73±1.45	0.13±0.03	4.8	130.80	0.166	43.7	130.89	0.63	8.0
		49.79±1.27	0.10±0.03	3.5	65.40	0.067	7.0	41.15	0.28	1.6
		43.12±0.68	0.13±0.03	4.8	50.31	0.064	6.5			
		36.59±1.04	0.06±0.03	2.3	43.60	0.073	8.3			
					40.88	0.057	5.0			
					38.47	0.072	8.2			
2457995-2458295	300	139.49±3.50	0.30±0.03	9.2	143.40	0.121	54.2			
		88.20±3.20	0.13±0.03	4.0	89.63	0.079	22.9			
		61.83±2.80	0.07±0.03	2.3	59.75	0.063	14.8			
		41.94±1.64	0.06±0.03	1.8	42.18	0.071	18.5			
		27.14±0.45	0.09±0.03	2.7	26.56	0.046	7.6			
2458358-2458668	310	94.48±1.55	0.15±0.01	9.4	96.00	0.036	5.5	92.39	0.53	2.2
		67.66±1.43	0.08±0.01	5.3	67.20	0.025	2.7			
		30.74±1.12	0.02±0.01	1.4	32.00	0.025	2.7			
2458730-2459033	303	85.04±2.65	0.18±0.04	4.5	60.46	0.117	15.1	83.86	0.30	1.8
		60.41±1.79	0.13±0.04	3.3	35.73	0.144	23.0			
		35.35±1.30	0.06±0.04	1.6	29.11	0.051	2.9			
		29.64±0.95	0.06±0.04	1.5	27.10	0.055	3.4			
		27.48±1.11	0.04±0.04	1.1						
2459087-2459386	299	69.52±1.74	0.15±0.03	4.4	112.50	0.114	18.5	108.92	0.40	1.3
		35.36±1.05	0.06±0.03	1.9	67.50	0.231	76.1			
		22.89±0.42	0.07±0.03	2.0	35.53	0.061	5.2			
					23.28	0.049	3.4			
2459465-2459586	121	37.63±1.14	0.19±0.03	4.7	37.29	0.114	3.3			
		21.56±0.78	0.09±0.03	2.3	21.75	0.138	4.9			

Mrk 421

Table F.7: Period of the detected STVs in the optical light curves of Mrk 421.

JD	Duration	Discrete Fourier Transform (P04)			Fast Fourier Transform (Python)			Lomb-Scargle Periodogram		
	(days)	Period (days)	Amplitude	S/N	Period (days)	Amplitude	S/N	Period (days)	Amplitude	S/N
2456369-2456502	133	60.04 ± 2.75	0.12 ± 0.02	5.405	15.88	0.063	3.4	63.27	0.44	3.9
		28.20 ± 0.82	0.09 ± 0.02	4.010				26.41	0.44	3.8
		14.00 ± 0.23	0.08 ± 0.02	3.487						
2456614-2456838	224	42.25 ± 0.77	0.10 ± 0.02	4.810	45.86	0.107	11.7	42.91	0.44	4.0
		26.03 ± 0.41	0.07 ± 0.02	3.415	26.75	0.058	3.4			
2457168-2457612	444	109.94 ± 1.00	0.21 ± 0.01	13.506	70.50	0.072	25.4	106.87	0.56	6.2
		73.52 ± 0.86	0.11 ± 0.01	7.043	50.36	0.064	20.0			
		53.56 ± 0.35	0.14 ± 0.01	9.203						
2457728-2457962	234	112.09 ± 1.93	0.09 ± 0.01	12.32	32.57	0.075	12.0	110.50	0.74	10.9
		31.01 ± 0.44	0.03 ± 0.01	4.188				30.74	0.33	2.1
2458112-2458340	228	76.92 ± 9.84	0.04 ± 0.03	1.322	78.00	0.162	55.2	34.97	0.41	3.4
		22.87 ± 0.43	0.08 ± 0.03	2.675	34.67	0.060	7.7	22.32	0.30	1.8
					22.29	0.050	5.2			

Mrk 180

Table F.8: Period of the detected STVs in the optical light curves of Mrk 180.

JD	Duration	Discrete Fourier Transform (P04)			Fast Fourier Transform (Python)			Lomb-Scargle Periodogram		
	(days)	Period (days)	Amplitude	S/N	Period (days)	Amplitude	S/N	Period (days)	Amplitude	S/N
2457181-2457643	462	117.74 ± 2.11	0.10 ± 0.01	6.4	147.00	0.034	4.9	147.16	0.45	15.0
		62.23 ± 0.40	0.15 ± 0.01	9.3	61.25	0.033	4.8	120.80	0.43	13.4
		44.32 ± 0.30	0.10 ± 0.01	6.3	45.94	0.044	8.5			
		33.06 ± 0.10	0.17 ± 0.01	10.1	33.41	0.029	3.7			
		27.38 ± 0.15	0.08 ± 0.01	4.8	27.22	0.032	4.4			
		17.00 ± 0.06	0.08 ± 0.01	4.8	17.93	0.026	3.0			

Mrk 501

Table F.9: Period of the detected STVs in the optical light curves of Mrk 501.

JD	Duration	Discrete Fourier Transform (P04)			Fast Fourier Transform (Python)			Lomb-Scargle Periodogram		
	(days)	Period (days)	Amplitude	S/N	Period (days)	Amplitude	S/N	Period (days)	Amplitude	S/N
2457302-2457625	323	142.36 ± 3.45	0.062 ± 0.01	8.85				137.79	0.63	8.1
		36.42 ± 0.70	0.02 ± 0.01	2.859				36.03	0.27	1.5

BL Lac

Table F.10: Period of the detected STVs in the optical light curves of BL Lac.

JD	Duration	Discrete Fourier Transform (P04)			Fast Fourier Transform (Python)			Lomb-Scargle Periodogram		
	(days)	Period (days)	Amplitude	S/N	Period (days)	Amplitude	S/N	Period (days)	Amplitude	S/N
2456826-2456987	161	18.99 ± 0.38	0.13 ± 0.04	3.2	19.8462	0.0718	1.184			
		11.90 ± 0.64	0.03 ± 0.04	0.7	13.5789	0.0715	1.1747			
2457181-2457643	462	62.23 ± 0.40	0.15 ± 0.01	9.3	60.27	0.1	6.48			
		44.32 ± 0.30	0.10 ± 0.01	6.3	44.20	0.1	5.32			
		33.06 ± 0.10	0.17 ± 0.01	10.1	33.15	0.1	5.90			
		27.38 ± 0.15	0.08 ± 0.01	4.8	27.63	0.1	2.59			
		17.00 ± 0.06	0.08 ± 0.01	4.8	17.00	0.1	2.33			
2457826-2458188	362	74.85 ± 1.12	0.12 ± 0.02	6.1	72.00	0.1	2.39	73.4864	0.5975	3.5698
		27.66 ± 0.18	0.10 ± 0.02	5.2	27.00	0.1	2.37	27.5807	0.4888	2.3891
2458267-2458552	285	64.95 ± 1.85	0.11 ± 0.03	3.8	67.80	0.2	8.4			
		33.01 ± 0.46	0.13 ± 0.04	4.0	33.90	0.2	13.30			
2458693-2458889	196	24.55 ± 0.43	0.16 ± 0.04	3.3	25.00	0.2	9.8			
		21.23 ± 0.36	0.14 ± 0.04	2.9	21.43	0.2	7.4			

Appendix G

Tables of detected timescales of QPOs in radio wavelengths

G.1 Tables of short-term timescales of QPOs at 37 GHz

OJ 287

Table G.1: Period of the detected STVs in the radio curves of OJ 287 at 37 GHz.

JD	Duration	Discrete Fourier Transform (P04)			Fast Fourier Transform (Python)			Lomb-Scargle Periodogram		
	(days)	Period (days)	Amplitude	S/N	Period (days)	Amplitude	S/N	Period (days)	Amplitude	S/N
2456294-2459484	3190	313.07 ± 2.48	0.30 ± 0.04	5.4	310.09	0.33	25.2			
		225.62 ± 1.12	0.34 ± 0.04	6.2	227.40	0.34	27.4			
		181.88 ± 0.59	0.43 ± 0.04	7.7	179.53	0.46	49.6			
		128.69 ± 0.74	0.17 ± 0.04	3.1	126.33	0.13	3.8			
		110.62 ± 0.23	0.40 ± 0.04	7.3	110.03	0.32	23.9			
		91.31 ± 0.24	0.26 ± 0.04	4.7	92.19	0.45	47.7			

Mrk 421

Table G.2: Period of the detected STVs in the radio curves of Mrk 421 at 37 GHz.

JD	Duration	Discrete Fourier Transform (P04)			Fast Fourier Transform (Python)			Lomb-Scargle Periodogram		
	(days)	Period (days)	Amplitude	S/N	Period (days)	Amplitude	S/N	Period (days)	Amplitude	S/N
2456297-2457734	1437	124.54 ± 1.23	0.04 ± 0.01	3.8	125.67	0.045	5.3			
		54.35 ± 0.25	0.04 ± 0.01	3.5	56.55	0.034	3.0			

Mrk 501

Table G.3: Period of the detected STVs in the radio curves of Mrk 501 at 37 GHz.

JD	Duration	Discrete Fourier Transform (P04)			Fast Fourier Transform (Python)			Lomb-Scargle Periodogram		
	(days)	Period (days)	Amplitude	S/N	Period (days)	Amplitude	S/N	Period (days)	Amplitude	S/N
2456297-2459381	3084	27.00 ± 0.03	0.03 ± 0.01	3.9	25.30	0.03	3.6			

BL Lac

Table G.4: Period of the detected STVs in the radio curves of BL Lac at 37 GHz.

JD	Duration	Discrete Fourier Transform (P04)			Fast Fourier Transform (Python)			Lomb-Scargle Periodogram		
	(days)	Period (days)	Amplitude	S/N	Period (days)	Amplitude	S/N	Period (days)	Amplitude	S/N
2456294-2459485	3191	351.00 ± 2.08	0.51 ± 0.05	8.7	348.64	0.58	221.5			
		272.94 ± 1.80	0.35 ± 0.05	6.1	271.17	0.20	27.0			
		190.04 ± 0.85	0.36 ± 0.05	6.3	187.73	0.10	6.1			
		163.29 ± 0.65	0.35 ± 0.05	6.1	162.70	0.21	28.5			
		86.85 ± 0.20	0.32 ± 0.05	5.5	87.16	0.10	6.1			

G.2 Tables of short-term timescales of QPOs at 15 GHz

OJ 287

Table G.5: Period of the detected STVs in the radio curves of OJ 287 at 15 GHz.

JD	Duration	Discrete Fourier Transform (P04)			Fast Fourier Transform (Python)			Lomb-Scargle Periodogram		
	(days)	Period (days)	Amplitude	S/N	Period (days)	Amplitude	S/N	Period (days)	Amplitude	S/N
2454473-2459204	4731	645.35 ± 3.56	0.76 ± 0.06	11.3	650.00	0.58	43.4			
		323.37 ± 1.91	0.36 ± 0.06	5.3	325.00	0.94	115.6			
		128.46 ± 0.37	0.29 ± 0.06	4.3	130.00	0.86	95.0			
		108.44 ± 0.27	0.28 ± 0.06	4.2	108.33	0.45	26.0			

Mrk 421

Table G.6: Period of the detected STVs in the radio curves of Mrk 421 at 15 GHz.

JD	Duration	Discrete Fourier Transform (P04)			Fast Fourier Transform (Python)			Lomb-Scargle Periodogram		
	(days)	Period (days)	Amplitude	S/N	Period (days)	Amplitude	S/N	Period (days)	Amplitude	S/N
2454473-2459195	4722	438.37 ± 4.04	0.02 ± 0.01	4.1	363.43	0.042	95.3	443.18	0.27	6.1
		234.67 ± 0.68	0.04 ± 0.01	7.0	231.27	0.030	49.7	362.64	0.27	6.0
		178.72 ± 0.39	0.04 ± 0.01	7.1	159.00	0.012	7.9	177.83	0.27	6.1
		146.78 ± 0.42	0.02 ± 0.01	4.5	149.65	0.011	6.1	161.88	0.21	3.8
		77.26 ± 0.12	0.02 ± 0.01	4.2	77.09	0.010	5.0	148.75	0.23	4.7
		70.83 ± 0.11	0.02 ± 0.01	3.8	72.69	0.025	33.2			

Mrk 180

Table G.7: Period of the detected STVs in the radio curves of Mrk 180 at 15 GHz.

JD	Duration	Discrete Fourier Transform (P04)			Fast Fourier Transform (Python)			Lomb-Scargle Periodogram		
	(days)	Period (days)	Amplitude	S/N	Period (days)	Amplitude	S/N	Period (days)	Amplitude	S/N
2454474-2459199	4725	887.32 ± 7.51	0.014 ± 0.001	9.9	165.27	0.011	73.5	888.19	0.35	29.4
		402.98 ± 2.64	0.008 ± 0.001	5.8	121.20	0.005	18.5	403.95	0.27	17.6
		338.10 ± 2.55	0.006 ± 0.001	4.2	106.94	0.004	11.5	335.24	0.20	9.5
		165.93 ± 0.76	0.005 ± 0.001	3.4				166.03	0.20	9.2
		108.81 ± 0.33	0.005 ± 0.001	3.4				119.70	0.14	5.0
								108.95	0.15	5.7

Mrk 501

Table G.8: Period of the detected STVs in the radio curves of Mrk 501 at 15 GHz.

JD	Duration	Discrete Fourier Transform (P04)			Fast Fourier Transform (Python)			Lomb-Scargle Periodogram		
	(days)	Period (days)	Amplitude	S/N	Period (days)	Amplitude	S/N	Period (days)	Amplitude	S/N
2454853-2459199	4346	370.02 ± 2.12	0.02 ± 0.01	6.5	376.20	0.038	106.7			
		186.57 ± 0.88	0.01 ± 0.01	4.0	188.10	0.009	5.9			
		159.23 ± 0.62	0.01 ± 0.01	4.2	156.75	0.007	3.5			
		143.94 ± 0.54	0.01 ± 0.01	3.9	144.69	0.017	20.5			
		135.21 ± 0.37	0.02 ± 0.01	5.0	134.36	0.015	15.5			
		54.67 ± 0.08	0.01 ± 0.01	3.6	53.74	0.007	3.5			

BL Lac

Table G.9: Period of the detected STVs in the radio curves of BL Lac at 15 GHz.

JD	Duration	Discrete Fourier Transform (P04)			Fast Fourier Transform (Python)			Lomb-Scargle Periodogram		
	(days)	Period (days)	Amplitude	S/N	Period (days)	Amplitude	S/N	Period (days)	Amplitude	S/N
2454908-2459202	4294	245.47 ± 1.65	0.47 ± 0.09	3.8	248.25	0.13	7.6			
		66.339 ± 0.16	0.34 ± 0.09	2.8	66.20	0.33	49.1			
		43.38 ± 0.07	0.36 ± 0.09	2.9	43.17	0.12	6.7			

G.3 Tables of short-term timescales of QPOs at 4.8 GHz

OJ 287

Table G.10: Period of the detected STVs in the radio curves of OJ 287 at 4.8 GHz.

JD	Duration	Discrete Fourier Transform (P04)			Fast Fourier Transform (Python)			Lomb-Scargle Periodogram		
	(days)	Period (days)	Amplitude	S/N	Period (days)	Amplitude	S/N	Period (days)	Amplitude	S/N
2457716-2459242	1526	28.017 ± 0.036	0.402 ± 0.051	6.4	26.63	0.23	3.2	28.02	0.61	15.6
		16.555 ± 0.011	0.459 ± 0.051	7.3				16.55	0.60	15.1

Mrk 421

Table G.11: Period of the detected STVs in the radio curves of Mrk 421 at 4.8 GHz.

JD	Duration	Discrete Fourier Transform (P04)			Fast Fourier Transform (Python)			Lomb-Scargle Periodogram		
	(days)	Period (days)	Amplitude	S/N	Period (days)	Amplitude	S/N	Period (days)	Amplitude	S/N
2457777-2459243	1466	23.527 ± 0.024	0.026 ± 0.003	6.5				23.12	0.69	7.8
		18.696 ± 0.010	0.038 ± 0.003	9.5				18.14	0.58	5.5
		17.639 ± 0.012	0.030 ± 0.003	7.4				17.42	0.57	5.2
		11.734 ± 0.004	0.041 ± 0.003	10.4				11.15	0.66	7.1

Mrk 501

Table G.12: Period of the detected STVs in the radio curves of Mrk 501 at 4.8 GHz.

JD	Duration	Discrete Fourier Transform (P04)			Fast Fourier Transform (Python)			Lomb-Scargle Periodogram		
	(days)	Period (days)	Amplitude	S/N	Period (days)	Amplitude	S/N	Period (days)	Amplitude	S/N
2457777-2459243	1466	29.819 ± 0.071	0.036 ± 0.008	3.8				29.81	0.51	5.1
		10.254 ± 0.007	0.046 ± 0.008	4.9				10.24	0.62	7.7

BL Lac

Table G.13: Period of the detected STVs in the radio curves of BL Lac at 4.8 GHz.

JD	Duration	Discrete Fourier Transform (P04)			Fast Fourier Transform (Python)			Lomb-Scargle Periodogram		
	(days)	Period (days)	Amplitude	S/N	Period (days)	Amplitude	S/N	Period (days)	Amplitude	S/N
2458291 - 2459330	1039	18.52 ± 0.02	0.09 ± 0.01	5.2	18.65	0.04	1.7			
		15.90 ± 0.03	0.07 ± 0.01	3.0	16.43	0.04	1.9			
		11.26 ± 0.01	0.19 ± 0.01	5.3	11.69	0.04	2.2			

Appendix H

Tables of detected timescales of QPOs in X-rays

H.1 Tables of intra-day timescales of QPOs in X-rays

1ES 0236+61

Table H.1: Period of the detected IDVs in the X-ray flux sequence of 1ES 0236+61.

JD	Duration (min)	Discrete Fourier Transform (P04)			Fast Fourier Transform (Python)			Lomb-Scargle Periodogram		
		Period (min)	Amplitude	S/N	Period (min)	Amplitude	S/N	Period (min)	Amplitude	S/N
2454298	1170.66									

1H 0323+342

Table H.2: Period of the detected IDVs in the X-ray flux sequence of 1H 0323+342.

JD	Duration (min)	Discrete Fourier Transform (P04)			Fast Fourier Transform (Python)			Lomb-Scargle Periodogram		
		Period (min)	Amplitude	S/N	Period (min)	Amplitude	S/N	Period (min)	Amplitude	S/N
2453922	1167.02	37.99 ± 0.23	0.06 ± 0.02	3.4	37.29	0.07	2.4	31.47	0.69	12.3
					31.62	0.06	2.1			

PKS 0716+714

Table H.3: Period of the detected IDVs in the X-ray flux sequence of PKS 0716+714.

JD	Duration (min)	Discrete Fourier Transform (P04)			Fast Fourier Transform (Python)			Lomb-Scargle Periodogram		
		Period (min)	Amplitude	S/N	Period (min)	Amplitude	S/N	Period (min)	Amplitude	S/N
2457061	1069.89	33.55 ± 0.21	0.07 ± 0.02	3.7	35.14	0.11	3.5			
2457062	1318.67	260.31 ± 8.36	0.06 ± 0.02	2.2	257.76	0.09	2.5			
		49.73 ± 0.21	0.09 ± 0.02	4.3	51.55	0.10	3.1			

1ES 0836+71

Table H.4: Period of the detected IDVs in the X-ray flux sequence of 1ES 0836+71.

JD	Duration (min)	Discrete Fourier Transform (P04)			Fast Fourier Transform (Python)			Lomb-Scargle Periodogram		
		Period (min)	Amplitude	S/N	Period (min)	Amplitude	S/N	Period (min)	Amplitude	S/N
2454194	1361.8224									
2454849	882.42	73.76 ± 1.33	0.02 ± 0.01	4.5	73.80	0.0	2.4			
		34.59 ± 0.22	0.02 ± 0.01	4.8	32.80	0.0	2.5			

Mrk 421

Table H.5: Period of the detected IDVs in the X-ray flux sequence of Mrk 421.

JD	Duration (min)	Discrete Fourier Transform (P04)			Fast Fourier Transform (Python)			Lomb-Scargle Periodogram		
		Period (min)	Amplitude	S/N	Period (min)	Amplitude	S/N	Period (min)	Amplitude	S/N
2456302	1168.26	45.35 ± 0.13	0.36 ± 0.05	5.6	44.64	0.23	3.8			
		8.08 ± 0.01	0.17 ± 0.05	3.4	8.61	0.24	3.9			
2456307	686.62	19.49 ± 0.13	0.29 ± 0.13	1.5	21.29	0.61	4.2			
		8.89 ± 0.03	0.25 ± 0.13	4.8	7.45	0.57	3.6			
2456312	489.50	71.56 ± 0.76	0.64 ± 0.08	1.2	68.30	0.46	9.3			
		56.33 ± 0.39	0.77 ± 0.08	2.0	59.76	0.64	17.5			
		26.33 ± 0.19	0.36 ± 0.08	3.2	28.12	0.27	3.1			
2456368	499.39	158.17 ± 0.87	5.83 ± 0.18	17.8	155.52	4.42	118.4			
		78.13 ± 0.22	5.56 ± 0.18	23.2	77.76	4.10	101.9			
		33.63 ± 0.09	2.44 ± 0.18	6.8	34.56	2.37	34.1			
		14.69 ± 0.07	0.64 ± 0.18	2.5	14.81	1.05	6.7			
2456385	306.79	30.64 ± 0.77	0.90 ± 0.41	2.1	31.25	0.97	5.7			
		19.84 ± 0.35	0.84 ± 0.41	3.9	20.83	0.72	3.1			
		11.34 ± 0.23	0.42 ± 0.41	2.0	12.02	0.59	2.1			
2456394	507.66	16.66 ± 0.03	3.12 ± 0.97	1.7	16.49	2.41	3.1			
		15.11 ± 0.04	2.38 ± 0.97	3.4	15.07	3.19	5.5			
		10.37 ± 0.02	2.35 ± 0.97	1.3	11.65	2.97	4.8			
2456395	495.63	25.76 ± 0.22	4.64 ± 1.39	1.2	27.84	3.17	4.2			
		16.23 ± 0.08	5.06 ± 1.39	3.4	15.47	3.93	6.4			
		11.34 ± 0.06	3.48 ± 1.39	2.2	11.60	2.69	3.0			
2456396	505.84	108.57 ± 0.18	20.91 ± 0.79	4.2	105.12	5.95	81.7			
		47.52 ± 0.07	10.34 ± 0.79	1.9	47.78	1.89	8.3			
		38.54 ± 0.08	5.90 ± 0.79	1.5	37.54	2.96	20.3			
		9.46 ± 0.02	1.21 ± 0.79	1.4	9.73	1.62	6.1			
2456397	297.75	32.71 ± 0.03	7.72 ± 0.41	4.9	32.12	4.60	11.4			
		21.33 ± 0.04	2.31 ± 0.41	1.5	21.98	2.89	4.5			
		15.40 ± 0.01	3.54 ± 0.41	2.3	14.91	2.81	4.2			
		12.02 ± 0.01	2.68 ± 0.41	1.7	11.60	2.79	4.2			
2456398	900.36	92.19 ± 0.11	14.65 ± 0.46	5.0	92.64	5.46	95.0			
		76.12 ± 0.26	4.18 ± 0.46	1.9	79.41	3.46	38.3			
		17.98 ± 0.03	1.76 ± 0.46	2.2	17.37	1.19	4.5			
2456399	603.91	196.75 ± 0.95	5.89 ± 0.16	33.1	200.88	3.79	60.7			
		54.07 ± 0.11	3.74 ± 0.16	8.8	53.57	2.39	24.2			
		32.79 ± 0.06	2.41 ± 0.16	9.9	32.14	1.72	12.4			

Table H.5 continued from previous page

2456743	587.39	14.61 ± 0.30	0.26 ± 0.39	1.1	15.36	0.62	2.7
2457785	683.24	18.53 ± 0.16	0.54 ± 0.32	1.2	19.10	0.68	4.0
2458136	678.69	23.07 ± 0.03	25.36 ± 1.72	6.2	23.45	3.70	6.5
		17.80 ± 0.07	6.78 ± 1.72	1.2	18.24	5.38	13.7
		12.55 ± 0.02	9.69 ± 1.72	2.0	12.01	2.95	4.1
2458137	675.29	88.05 ± 0.11	14.69 ± 0.25	11.2	92.57	5.94	108.5
		40.63 ± 0.12	2.70 ± 0.25	1.7	38.12	1.01	3.1
		23.80 ± 0.05	2.21 ± 0.25	2.7	24.00	1.85	10.5
		16.58 ± 0.04	1.43 ± 0.25	2.7	16.62	1.21	4.5
		14.77 ± 0.05	0.90 ± 0.25	2.4	14.40	1.31	5.3

3C 273

Table H.6: Period of the detected IDVs in the X-ray flux sequence of 3C 273.

JD	Duration (min)	Discrete Fourier Transform (P04)			Fast Fourier Transform (Python)			Lomb-Scargle Periodogram		
		Period (min)	Amplitude	S/N	Period (min)	Amplitude	S/N	Period (min)	Amplitude	S/N
2453561	399.43	22.72 ± 0.29	0.07 ± 0.03	22.7	20.16	0.13	1.4			
		10.37 ± 0.06	0.07 ± 0.03	11.5	11.20	0.24	5.1			
2454112	889.08	80.04 ± 0.84	0.23 ± 0.05	1.3	81.12	0.37	16.3			
		12.65 ± 0.04	0.11 ± 0.05	1.9	11.06	0.23	6.3			
2454442	206.32	14.05 ± 0.28	0.12 ± 0.06	27.2	15.06	0.28	2.5			
					13.06	0.37	4.3			
2454443	204.48	17.82 ± 0.73	0.07 ± 0.06	6.6	17.57	0.25	1.9			
2455540	1057.36	18.22 ± 0.05	0.12 ± 0.03	5.2	20.97	0.16	2.8			
		11.82 ± 0.03	0.09 ± 0.03	2.6	10.17	0.14	2.1			
2455905	989.25	10.19 ± 0.02	0.09 ± 0.03	5.8	10.80	0.10	2.1			
2456109	399.97	27.51 ± 0.37	0.08 ± 0.03	5.8653	25.40	0.10	1.3			
		13.83 ± 0.07	0.10 ± 0.03	11.5	12.70	0.11	1.5			
2456124	792.22	21.11 ± 0.06	0.21 ± 0.04	5.9	21.72	0.24	4.6			
		11.49 ± 0.03	0.10 ± 0.04	8.4	10.86	0.23	4.4			
2457217	968.11	29.62 ± 0.10	0.12 ± 0.02	5.8	29.09	0.08	1.9			
		12.48 ± 0.03	0.08 ± 0.02	3.8	12.12	0.11	3.3			
2457566	588.99	39.52 ± 0.13	0.40 ± 0.05	4.8	37.03	0.42	7.6			
		32.01 ± 0.21	0.17 ± 0.05	1.6	32.40	0.27	3.2			
		11.50 ± 0.03	0.15 ± 0.05	2.8	11.78	0.25	2.7			
2457931	782.04	34.54 ± 0.20	0.30 ± 0.07	4.5	35.28	0.38	8.5			
		8.16 ± 0.02	0.20 ± 0.07	7.2	8.47	0.20	2.3			
2458304	1352.02	7.78 ± 0.01	0.06 ± 0.03	3.6	6.13	0.14	3.3			
2458667	598.02	14.96 ± 0.05	0.10 ± 0.02	6.13	13.75	0.11	2.3			
		6.15 ± 0.01	0.08 ± 0.02	4.66	6.57	0.16	5.0			
2459036	1058.70	59.69 ± 0.35	0.21 ± 0.04	2.8	62.64	0.58	27.9			
2459375	604.22	158.19 ± 3.05	0.28 ± 0.04	2.2	156.96	0.29	6.7			
		7.47 ± 0.02	0.12 ± 0.04	2.5	6.54	0.21	3.4			

3C 279

Table H.7: Period of the detected IDVs in the X-ray flux sequence of 3C 279.

JD	Duration (min)	Discrete Fourier Transform (P04)			Fast Fourier Transform (Python)			Lomb-Scargle Periodogram		
		Period (min)	Amplitude	S/N	Period (min)	Amplitude	S/N	Period (min)	Amplitude	S/N
2453748	1375.42	8.91 ± 0.01	0.02 ± 0.01	4.6	8.60	0.04	4.7			
2453749	1358.58	12.85 ± 0.02	0.03 ± 0.01	4.3	11.62	0.05	4.0			
2453752	1367.61	24.43 ± 0.09	0.013 ± 0.005	3.7	27.05	0.02	2.4			
		10.67 ± 0.01	0.020 ± 0.005	5.0	12.22	0.02	2.1			
		8.70 ± 0.01	0.018 ± 0.005	4.6	8.42	0.02	2.7			
2453753	1363.68	11.65 ± 0.02	0.02 ± 0.01	2.8	10.02	0.03	2.3			
2454795	794.02	8.14 ± 0.02	0.02 ± 0.01	5.0	9.12	0.04	2.1			
2454796	1167.84	7.42 ± 0.01	0.03 ± 0.01	3.5	8.11	0.05	5.2			
2454799	1256.28	72.31 ± 0.59	0.02 ± 0.01	3.3	70.27	0.04	8.1			
		10.35 ± 0.02	0.01 ± 0.01	4.3	11.33	0.04	5.9			
		8.91 ± 0.01	0.02 ± 0.01	4.7	8.37	0.03	2.8			
2454800	1162.63	101.92 ± 0.65	0.07 ± 0.01	8.7	23.20	0.06	5.3	102.85	0.46	2.1
		23.32 ± 0.09	0.03 ± 0.01	8.0						

PKS 1553+113

Table H.8: Period of the detected IDVs in the X-ray flux sequence of PKS 1553+113.

JD	Duration (min)	Discrete Fourier Transform (P04)			Fast Fourier Transform (Python)			Lomb-Scargle Periodogram		
		Period (min)	Amplitude	S/N	Period (min)	Amplitude	S/N	Period (min)	Amplitude	S/N
2453649	1262.46	41.97 ± 0.17	0.26 ± 0.06	4.3	40.32	0.3	3.28			
		30.18 ± 0.08	0.30 ± 0.06	5.7	32.26	0.3	3.851			
		24.22 ± 0.04	0.42 ± 0.06	5.9	23.04	0.4	4.3674			
2459235	1352.58									
2459244	1352.95	8.81 ± 0.01	0.22 ± 0.05	7.4	8.29	0.4	4.10			

Mrk 501

Table H.9: Period of the detected IDVs in the X-ray flux sequence of Mrk 501.

JD	Duration (min)	Discrete Fourier Transform (P04)			Fast Fourier Transform (Python)			Lomb-Scargle Periodogram		
		Period (min)	Amplitude	S/N	Period (min)	Amplitude	S/N	Period (min)	Amplitude	S/N
2454395	1402.92	54.43 ± 0.30	0.16 ± 0.04	3.0	56.16	0.2	3.51			
		26.43 ± 0.05	0.23 ± 0.04	8.4	24.07	0.2	4.33			
2454979	1350.06	11.17 ± 0.02	0.12 ± 0.04	7.2	12.96	0.2	1.43			
2456395	783.82	27.70 ± 0.17	0.11 ± 0.04	3.3	25.00	0.1	1.20			
		19.60 ± 0.06	0.15 ± 0.04	7.7	19.65	0.1	1.51			
		9.91 ± 0.03	0.09 ± 0.04	3.0	9.48	0.1	1.20			
		7.33 ± 0.02	0.08 ± 0.04	2.9	7.43	0.2	3.66			
2456487	402.54	15.52 ± 0.14	0.23 ± 0.10	5.8	14.40	0.2	1.1999			
		10.78 ± 0.06	0.26 ± 0.10	2.6	10.29	0.4	3.72			
		6.63 ± 0.03	0.21 ± 0.10	3.6	6.75	0.3	1.48			
2456748	579.37	11.49 ± 0.06	0.12 ± 0.05	5.4	11.87	0.4	5.45			
2457871	590.00	77.03 ± 1.67	0.23 ± 0.07	1.1	76.32	0.8	29.95			
		25.75 ± 0.15	0.28 ± 0.07	3.9	25.44	0.4	6.15			

1ES 1959+650

Table H.10: Period of the detected IDVs in the X-ray flux sequence of 1ES 1959+650.

JD	Duration (min)	Discrete Fourier Transform (P04)			Fast Fourier Transform (Python)			Lomb-Scargle Periodogram		
		Period (min)	Amplitude	S/N	Period (min)	Amplitude	S/N	Period (min)	Amplitude	S/N
2453479	776.30									
2453878	306.58									
2453882	690.64	42.69 ± 0.29	0.29 ± 0.10	5.3	40.19	0.21	1.2			
2453883	296.58	55.90 ± 2.23	0.21 ± 0.08	4.3	57.60	0.52	4.5			
		27.45 ± 0.44	0.25 ± 0.08	6.8	28.80	0.50	4.2			
2453884	300.20	79.87 ± 1.35	0.57 ± 0.07	34.6	77.14	0.37	2.4			

BL Lac

Table H.11: Period of the detected IDVs in the X-ray flux sequence of BL Lac.

JD	Duration (min)	Discrete Fourier Transform (P04)			Fast Fourier Transform (Python)			Lomb-Scargle Periodogram		
		Period (min)	Amplitude	S/N	Period (min)	Amplitude	S/N	Period (min)	Amplitude	S/N
2453883	317.92									
2455028	1366.59									

3C 454.3

Table H.12: Period of the detected IDVs in the X-ray flux sequence of 3C 454.3.

JD	Duration (min)	Discrete Fourier Transform (P04)			Fast Fourier Transform (Python)			Lomb-Scargle Periodogram		
		Period (min)	Amplitude	S/N	Period (min)	Amplitude	S/N	Period (min)	Amplitude	S/N
2453485	1366.34	18.46 ± 0.04	0.10 ± 0.03	4.2	18.14	0.14	2.4			

H.2 Tables of short-term timescales of QPOs in X-rays

1ES 0236+61

Table H.13: Period of the detected STVs in the flux sequence of 1ES 0236+61 in X-rays.

JD	Duration	Discrete Fourier Transform (P04)			Fast Fourier Transform (Python)			Lomb-Scargle Periodogram		
	(days)	Period (days)	Amplitude	S/N	Period (days)	Amplitude	S/N	Period (days)	Amplitude	S/N
2457566-2458050	484	25.96 ± 0.13	0.05 ± 0.01	4.9	19.60	0.06	3.8	25.94	0.40	3.2
		18.30 ± 0.10	0.03 ± 0.01	3.1	13.36	0.05	2.7	13.34	0.47	4.4
		13.34 ± 0.03	0.06 ± 0.01	5.6						

1ES 0836+71

Table H.14: Period of the detected STVs in the flux sequence of 1ES 0836+71 in X-rays.

JD	Duration	Discrete Fourier Transform (P04)			Fast Fourier Transform (Python)			Lomb-Scargle Periodogram		
	(days)	Period (days)	Amplitude	S/N	Period (days)	Amplitude	S/N	Period (days)	Amplitude	S/N
2456675-2457664	989	30.65 ± 0.05	0.13 ± 0.02	4.8				31.11	0.6	3.475

OJ 287

Table H.15: Period of the detected STVs in the flux sequence of OJ 287 in X-rays.

JD	Duration	Discrete Fourier Transform (P04)			Fast Fourier Transform (Python)			Lomb-Scargle Periodogram		
	(days)	Period (days)	Amplitude	S/N	Period (days)	Amplitude	S/N	Period (days)	Amplitude	S/N
2457024-2457555	531	27.18 ± 0.12	8.71 ± 1.41	5.0	25.95	11.4	9.71			
		22.08 ± 0.11	6.28 ± 1.41	3.6	21.63	8.8	5.87			
		15.54 ± 0.06	5.74 ± 1.41	3.3	15.26	5.3	2.13			
2458090-2458294	204	58.40 ± 2.16	11.99 ± 2.80	3.4	60.60	13.2	5.40			
		25.17 ± 0.42	11.51 ± 2.80	3.3	23.31	11.2	3.85			
		11.91 ± 0.20	5.35 ± 2.80	1.5	11.22	9.1	2.56			
2459130-2459377	247	87.57 ± 2.30	12.28 ± 1.65	6.1	90.00	16.4	43.10			
		68.19 ± 1.06	16.16 ± 1.65	8.0	72.00	4.7	3.61			
		27.20 ± 0.21	12.69 ± 1.65	6.2	24.00	6.4	6.67			

Mrk 421

Table H.16: Period of the detected STVs in the flux sequence of Mrk 421 in X-rays.

JD	Duration	Discrete Fourier Transform (P04)			Fast Fourier Transform (Python)			Lomb-Scargle Periodogram		
	(days)	Period (days)	Amplitude	S/N	Period (days)	Amplitude	S/N	Period (days)	Amplitude	S/N
2457024-2457555	531	27.18 ± 0.12	8.71 ± 1.41	5.0	25.95	11.4	9.71			
		22.08 ± 0.11	6.28 ± 1.41	3.6	21.63	8.8	5.87			
		15.54 ± 0.06	5.74 ± 1.41	3.3	15.26	5.3	2.13			
2458090-2458294	204	58.40 ± 2.16	11.99 ± 2.80	3.4	60.60	13.2	5.40			
		25.17 ± 0.42	11.51 ± 2.80	3.3	23.31	11.2	3.85			
		11.91 ± 0.20	5.35 ± 2.80	1.5	11.22	9.1	2.56			
2459130-2459377	247	87.57 ± 2.30	12.28 ± 1.65	6.1	90.00	16.4	43.10			
		68.19 ± 1.06	16.16 ± 1.65	8.0	72.00	4.7	3.61			
		27.20 ± 0.21	12.69 ± 1.65	6.2	24.00	6.4	6.67			

3C 273

Table H.17: Period of the detected STVs in the flux sequence of 3C 273 in X-rays.

JD	Duration	Discrete Fourier Transform (P04)			Fast Fourier Transform (Python)			Lomb-Scargle Periodogram		
	(days)	Period (days)	Amplitude	S/N	Period (days)	Amplitude	S/N	Period (days)	Amplitude	S/N
2455170-2457217	2047	78.97 ± 0.27	0.61 ± 0.10	4.9	78.60	0.5	4.36			
		38.97 ± 0.10	0.39 ± 0.10	3.2	39.30	0.3	2.14			

Mrk 501

Table H.18: Period of the detected STVs in the flux sequence of Mrk 501 in X-rays.

JD	Duration	Discrete Fourier Transform (P04)			Fast Fourier Transform (Python)			Lomb-Scargle Periodogram		
	(days)	Period (days)	Amplitude	S/N	Period (days)	Amplitude	S/N	Period (days)	Amplitude	S/N
2455623-2456138	515	83.06 ± 1.80	1.03 ± 0.25	3.3	82.50	1.5	10.08			
		7.21 ± 0.01	2.10 ± 0.25	6.7	7.67	1.0	4.71			
2456717-2456946	229	47.81 ± 0.56	2.82 ± 0.29	7.8	45.00	1.6	4.13			
		37.91 ± 0.48	2.07 ± 0.29	5.7	38.57	2.1	6.92			
		32.53 ± 0.25	2.85 ± 0.29	7.9	33.75	1.4	3.21			

1ES 1959+650

Table H.19: Period of the detected STVs in the flux sequence of 1ES 1959+650 in X-rays.

JD	Duration	Discrete Fourier Transform (P04)			Fast Fourier Transform (Python)			Lomb-Scargle Periodogram		
	(days)	Period (days)	Amplitude	S/N	Period (days)	Amplitude	S/N	Period (days)	Amplitude	S/N
2457045-2457797	752	54.21 ± 0.43	1.82 ± 0.36	4.0	51.60	1.63	2.6			
		22.30 ± 0.07	1.84 ± 0.36	4.1	22.43	2.85	7.8			
2457900-2459317	1417	73.16 ± 0.52	1.97 ± 0.49	3.2	75.00	2.42	4.1			
		50.39 ± 0.25	1.94 ± 0.49	3.2	50.00	2.65	4.9			
		39.12 ± 0.14	2.14 ± 0.49	3.5	39.47	2.26	3.6			
		25.83 ± 0.07	1.83 ± 0.49	3.0	22.73	2.88	5.8			

BL Lac

Table H.20: Period of the detected STVs in the flux sequence of BL Lac in X-rays.

JD	Duration	Discrete Fourier Transform (P04)			Fast Fourier Transform (Python)			Lomb-Scargle Periodogram		
	(days)	Period (days)	Amplitude	S/N	Period (days)	Amplitude	S/N	Period (days)	Amplitude	S/N
2456175-2457423	1248	72.42 ± 0.89	0.07 ± 0.03	2.2	76.71	0.07	16.8			
		51.70 ± 0.45	0.07 ± 0.03	2.3	51.14	0.05	9.6			
		36.39 ± 0.17	0.09 ± 0.03	2.9	35.80	0.06	12.0			
		30.15 ± 0.17	0.06 ± 0.03	2.0	29.03	0.05	9.3			

CTA 102

Table H.21: Period of the detected STVs in the flux sequence of CTA 102 in X-rays.

JD	Duration	Discrete Fourier Transform (P04)			Fast Fourier Transform (Python)			Lomb-Scargle Periodogram		
	(days)	Period (days)	Amplitude	S/N	Period (days)	Amplitude	S/N	Period (days)	Amplitude	S/N
2457560-2457970	410	53.96 ± 1.06	0.13 ± 0.03	3.0	100.50	0.2	16.36	96.0	0.4851	4.7059
		40.41 ± 0.63	0.12 ± 0.03	2.8	50.25	0.1	3.58			
					40.20	0.1	2.11			

3C 454.3

Table H.22: Period of the detected STVs in the flux sequence of 3C 454.3 in X-rays.

JD	Duration	Discrete Fourier Transform (P04)			Fast Fourier Transform (Python)			Lomb-Scargle Periodogram		
	(days)	Period (days)	Amplitude	S/N	Period (days)	Amplitude	S/N	Period (days)	Amplitude	S/N
2454613-2455213	600	74.08 ± 0.48	0.54 ± 0.05	8.6	74.57	0.3	16.30			
		53.10 ± 0.32	0.42 ± 0.05	6.7	52.20	0.5	31.84			
		41.24 ± 0.15	0.55 ± 0.05	8.7	40.15	0.2	7.87			
		37.04 ± 0.14	0.45 ± 0.05	7.2	37.29	0.4	19.86			
		25.00 ± 0.08	0.38 ± 0.05	6.1	24.86	0.2	3.56			
		23.26 ± 0.06	0.43 ± 0.05	6.9	23.73	0.1	2.31			
		19.59 ± 0.09	0.20 ± 0.05	3.2	18.00	0.2	4.95			